Aalto-yliopisto
Kemian tekniikan
korkeakoulu

School of Chemical Technology
Degree Programme of Chemical Technology

Aleksi Eskelinen

Dynamic modelling of a multiple hearth furnace

Master's thesis for the degree of Master of Science in Technology submitted for inspection, Espoo, 18.03.2014

Supervisor **Professor Sirkka-Liisa Jämsä-Jounela**

Instructor **Ph.D. Alexey Zakharov**

Aalto-yliopisto
Kemian tekniikan korkeakoulu

Aalto-yliopisto, PL 11000, 00076 AALTO
www.aalto.fi

Diplomityön tiivistelmä

Tekijä Aleksi Eskelinen

Työn nimi Monipohjaisen uunin dynaaminen mallinnus

Laitos Biotekniikan ja kemian tekniikan laitos

Professuuri Prosessien ohjaus ja automaation **Professuurikoodi** Kem-90

Työn valvoja Professori Sirkka-Liisa Jämsä-Jounela

Työn ohjaaja(t)/Työn tarkastaja(t) FT Alexey Zakharov

Päivämäärä 18.03.2014 **Sivumäärä** 172 + 34 **Kieli** englanti

Tiivistelmä

Tämän diplomityön tavoitteena on kehittää dynaaminen malli monipohjaisesta uunista (MPU), jota käytetään kaoliniitin kalsinoimiseen. Mallia tullaan käyttämään uunissa tapahtuvien monimutkaisten fysikaalis-kemiallisten ilmiöiden tutkimiseen ja sitä voidaan hyödyntää myös prosessin tilan seurannassa. Dynaaminen malli tukee myös uunin lämpötilaprofiilin säätöstrategian kehittämistä. Lisäksi on myös tärkeätä kyetä ajamaan prosessia mahdollisimman pienillä energiahäviöillä ja päästöillä.

Diplomityön kirjallisuusosassa esitellään aluksi yleinen kaoliniitin märkäkäsittely-tuotantoketju, jonka jälkeen kaoliniitin kalsinointiprosessiin paneudutaan yksityiskohtaisemmin. Seuraavaksi perehdytään kaoliniitin kalsinointireaktioihin ja niihin vaikuttaviin muuttujiin, kuten lämmitysnopeuteen, hiukkaskokoon ja raaka-aineen epäpuhtauksiin. Lisäksi kirjallisuusosassa esitellään viisi kaoliniitin kalsinointiuunin kanssa samankaltaisia matemaattista mallia, jotta MPU:n dynaamisen mallin kehittämiseen liittyvät rajoitteet ja vaatimukset ymmärrettäisiin paremmin.

Kokeellinen osa keskittyy erityisesti MPU:n dynaamisen mallin kehittämiseen. Aluksi esitellään reaktioiden kineettiset yhtälöt sekä yhtälöt joilla kuvataan massan ja lämmön siirto- ja säilymisilmiöt sekä lämmönsiirtoparametrit. Seuraavaksi alkuperäisen uunin 1:12 pienoismallilla on suoritettu kokeellisia testejä, joilla on määritetty kiintoainepedin dynamiikkamatriisi. Matriisi kuvaa kiintoainepedin liikkumista ja massan jakautumista uunissa. Matemaattiset algoritmit, joita käytetään mallin yhtälöryhmien ratkaisemiseen, on esitetty seuraavaksi; reaktionopeudet ratkaistaan eksplisiittisesti, kiintopedin massansiirto ratkaistaan käyttämällä diplomityössä kehitettyä sekoitusmallia, kaasufaasin massa- ja energiataseet ratkaistaan intervallijako-menetelmällä, jäähdytysilman, keskiakselin ja sekoituskäsien sekä uunin seinien lämpötilaprofiilit ratkaistaan yhdistämällä Eulerin menetelmä ja intervallijako-menetelmä ja viimeiseksi kiintopedin energiatase ratkaistaan yhdistämällä Eulerin menetelmä ja sekoitusmalli. MPU-malli on toteutettu MATLAB ympäristössä. Lisäksi MPU simulaattoriin on kehitetty graafinen käyttöliittymä.

Mallin dynaamista käyttäytymistä on testattu erillisillä askelkokeilla kolmessa syöttösuuressa: kaoliniitin syöttömäärässä, kaasu- ja ilmasyötöissä pohjalle 4 sekä kaasu- ja ilmasyötöissä pohjalle 6. Lisäksi mallin käyttäytymistä yhtäaikaisille askelmuutoksille jokaisessa syöttösuureessa on testattu ja lopuksi simuloidun mallin dynaaminen käyttäytyminen on testattu ja varmennettu käyttämällä teollisuudessa kerättyä dataa.

Tulokset osoittavat että mallin vaste edellä mainittuihin askelmuutoksiin on järkevä. Kokeissa huomattiin myös kaasufaasin lämpötilan reagoivan lähes välittömästi muutoksiin syöttösuureissa ja että kiintopedin koostumuksen muuttumisen vasteaika voi olla jopa 700 minuuttia eräissä tapauksissa. Verrattaessa dynaamisen mallin käyttäytymistä teollisuusdataan, mallin vaste käyttäytyy tyydyttävästi ja simuloitu lämpötilaprofiili täsmää mitattuihin lämpötiloihin.

Avainsanat Monipohjainen uuni, mallinnus, dynaaminen

Aalto University
School of Chemical
Technology

Aalto University, P.O. BOX 11000, 00076 AALTO
www.aalto.fi

Abstract of master's thesis

Author Aleksi Eskelinen

Title of thesis Dynamic modelling of a multiple hearth furnace

Department Department of Biotechnology and Chemical Technology

Professorship Process control and automation **Code of professorship** Kem-90

Thesis supervisor Professor Sirkka-Liisa Jämsä-Jounela

Thesis advisor(s) / Thesis examiner(s) Ph.D. Alexey Zakharov

Date 18.03.2014 **Number of pages** 172 + 34 **Language** English

Abstract

The aim of this thesis is to develop a dynamic model of a multiple hearth furnace (MHF) used for the kaolin calcination process. The resulting model facilitates in studying the complex physico-chemical phenomena occurring inside the furnace and providing a dynamic simulator for monitoring purposes. The dynamic model also provides means to develop a better control over the temperature profile of the kaolin bed moving inside the furnace. In addition, it is of utmost importance to run the process with minimum energy losses together with minimum possible emissions.

The literature part first introduces a common kaolin wet processing production chain after which the kaolin calcination process is studied in detail. Next, calcination reactions and the effects of factors, such as heating rate, particle size and impurities in the raw material to the calcination reactions are studied. Additionally, five different mathematical models similar to the kaolin calciner (MHF) are reviewed to understand the restrictions and the requirements for the development of a dynamic model of the MHF.

Particularly, the dynamic model of the MHF is developed in the experimental part. First, the modelling equations for the reaction kinetics, mass and heat transfer and conservation, including the heat exchange parameters, are described. Subsequently, experimental test are performed on a 1:12 scaled pilot model of the industrial furnace that determines the solid bed dynamics matrix. This matrix describes the solid bed movement and mass distribution in the furnace. To solve the system of the model equations the mathematical solving algorithms are introduced; the reaction rates are solved explicitly, the solid bed mass transfer is calculated using the developed mixing model, the mass and energy balances of the gas phase are solved with the internal division method, the temperature profiles of the cooling air, the central shaft and the arms and the walls are computed using the Euler method combined with internal division method and the solid bed energy balance is solved combining the Euler method with the mixing model. The MHF model is implemented under the MATLAB environment. In addition, a graphical user interface is developed for the MHF simulator.

The dynamic behaviour of the model is tested using step changes in the three inputs, namely the feed rate, the gas and air flows to the hearth 4 and the gas and air flows to the hearth 6, individually. In addition, the behaviour under simultaneous changes in each input variables is studied and finally the dynamics of the simulated model are tested and validated using the real industrial data.

The results show that the response of the model to the aforesaid changes is reasonable. It is also noticed that the response of the gas phase temperature is almost immediate and the response time of the changes in the solid bed composition is even over 700 minutes in some cases. Comparing the simulated results obtained from the dynamic model to that of the industrial data, the model behaves satisfactorily and the simulated temperature profile matches to the measured temperatures.

Keywords Multiple hearth furnace, modelling, dynamic

Preface

This master's thesis has been written in the Research Group of Process Control and Automation, at Aalto University School of Chemical Technology during the period 1. June 2013 – 20. February 2014. This work is a part of the STOICISM project. STOICISM (The Sustainable Technologies for Calcined Industrial Minerals) is a major innovative research project launched in the beginning of the year 2013 under the Framework Programme 7 for the "New environmentally friendly approaches to mineral processing".

First of all, I would like to express my gratitude to my professor Sirkka-Liisa Jämsä-Jounela for the opportunity to work in this project and for granting me the modelling part of our work group in the project. In addition, I would like to thank her for the interesting discussions we have had and for the guidance she has given for me during the project.

I would also like to thank my instructor, Ph.D. Alexey Zakharov, for his valuable support and expertise during the long hours spent for building and debugging the model. In addition, I would like to thank my co-workers at the lab for the advises they have given for me and for the friendly environment. Thank you, Tushar, Rinat, Jukka, Sasha, Octavio, Miao and Palash.

I very much appreciate the feedback and help received from the personnel of the IMERYS Par Moor research centre involved with the project.

Truly, I would like to thank my family for their support and encouragement through all the years in and outside the pool.

My final and the most tremendous thanks belong to my girlfriend Anna for her unceasing support, help and understanding.

Espoo, 20.2. 2014

Aleksi Eskelinen

Table of contents

Appendices

1. Derivation of the spinel phase peak temperature
2. The gas phase emissivity
3. Photos from the pilot experiments
4. Results of the pilot experiments
5. The model equations and the model parameters and their values

List of symbols:

A	area [m^2]
A_i	frequency factor of reaction i [1/s]
a_{ij}	solid bed movement parameter for volume j in hearth i
Bi	Biot number
C_i	concentration of component i [mol/m^3] (gas) / [kg] (solid)
$c_{p,i}$	heat capacity of component i [kJ/(kgK)]
D_i	solid bed dynamics matrix for hearth i
$E_{A,i}$	activation energy of reaction i [kJ/mol]
F	gas flow [m^3/s]
g	gravimetric constant 9.81 m/s^2
g_d	dust generation [kg/s]
h	height of annular heap [m]
h_{eff}	effective heat transfer coefficient [$W/(m^2K)$]
h_c	convective heat transfer coefficient [$W/(m^2K)$]
h_r	radiative heat transfer coefficient [$W/(m^2K)$]
k	thermal conductivity [W/(m K)]
k_i	reaction rate coefficient of reaction i [1/s]
L	length or characteristic dimension [m]
m_i	mass flow of component i [kg/s]
Nu	Nusselt number

n	number of rabble tooth
n_i	amount of substance i [mol]
P	perimeter [m]
Pr	Prandtl number
p	pressure [Pa]
Q_i	energy flux of component i [kJ/s]
R	ideal gas constant [8.3145 J/K mol]
Ra	Rayleigh number
R_i	reaction rate of reaction i [kg/s]
Re	Reynold number
r	radius [m]
r_0	inner radius of hearth [m]
T_i	absolute temperature of component i [K]
V	volume [m^3]
v_g	velocity of the gas [m/s]
X_i	conversion of component i
x_{H2O}	moisture content

Greek letters:

α	absorptivity
β	angle of repose [°] or volumetric expansion coefficient [1/K]
ε	emissivity
Φ	heating rate [K/min]
λ_i	thermal conductivity of a wall layer i [W/(m K)]
μ	viscosity (Pa s)
ρ	density [kg/m^3]
σ	Stefan-Boltzmann constant [W/(m^{2}K^4)]
φ	installment angle of rabble tooth [°]
Ω	form factor for radiation
ω	rotation speed of the central shaft [rps]
ϑ	overlapping ratio

1. Introduction

Kaolin, often known as china clay, consists primarily of the mineral kaolinite, which has the formula $Al_2Si_2O_5(OH)_4$. Calcination, a process of heating a substance to a point below its melting or fusing point, causing a loss of water from the structure, is one of the most important ways of enhancing the properties, and value, of kaolin. As a result of calcination, the kaolin becomes whiter and more chemically inert, allowing it to be used in a wide variety of products, such as paper, rubber, paint and refractory items.

During calcination, kaolin undergoes several physico-chemical reactions (Ptacek et al., 2010). The first reaction involves driving off the free moisture. Next, the kaolin undergoes a dehydroxylation reaction, in which the chemically bound water is removed and amorphous metakaolin is formed. The third reaction at around 980 °C leads to the transformation of metakaolin to the 'spinel phase' by exothermic re-crystallisation. Heating kaolin above 1000 °C, it begins to form mullite, which is hard and abrasive, and can cause damage to process equipment (Thomas, 2010).

In the process, under this study, the kaolin is calcined in a multiple hearth furnace (MHF) that has eight hearths. The heat for the calcination is provided through the burners located on the hearths 4 and 6. To maintain steady, good product quality, which has a low mullite and soluble aluminium content, the peak temperature the kaolin reaches in the furnace must be controlled carefully. For process simulation and control it is often necessary to develop a dynamic model of the process. The dynamic model provides means to study the physico-chemical reactions of the calcination process and to develop better control over the temperature profile of the kaolin bed moving inside the furnace. In addition, process monitoring can be enhanced with the help of the dynamic model of the process. Nowadays, it is also important to be able to run processes with minimum energy losses and with minimum possible emissions. The dynamic model to be developed can be used to

tune the process control so that minimum energy is used and as well for studying the energy consumption and the emissions of the MHF.

This thesis is a part of the STOICISM project. STOICISM (The Sustainable Technologies for Calcined Industrial Minerals) is a major innovative research project launched in the beginning of the year 2013 under the Framework Programme 7 for the "New environmentally friendly approaches to mineral processing". The STOICISM Consortium is led by IMERYS and consists of 17 partners from 8 different European countries. The area of responsibility of Aalto University is to design the concept for online monitoring and control of the calcined mineral processes. The special emphasis in the concept will be put on product quality, energy efficiency, environmental performance and economic aspects.

The aim of this thesis is to develop a concept of a dynamic model of a MHF. The dynamic model can be used to study the physico-chemical phenomena occurring inside the furnace and to provide a dynamic simulator for monitoring purposes.

The thesis is divided into two separate parts: the literature part and the experimental part. Chapter 2 reviews the whole kaolin processing chain from the pit to the ready calcined product and Chapter 3 explains the kaolin calcination process: the occurring reactions and phenomena affecting them. Chapter 4 reviews five state-of-art mathematical models related to calcination in multiple hearth furnaces (MHF) found from the literature. The aim of the experimental part is stated in Chapter 5. Next, Chapter 6 gives the process description of the kaolin calcination plant in Lee Moor UK. Chapter 7 presents the mathematical model of the MHF; it includes the calcination reactions, the mass transfer, the heat conservation equations and the calculation of heat transfer parameters, the emissivities of the solid bed and the gas phase and the heat capacity of the gas components. Chapter 8 explains the pilot experiments executed to determine the solid bed movement and Chapters 9 and 10 describe the solving of the systems of equations of the MHF and the graphical user interface developed for the simulator, respectively. The testing results for both the steady-state temperature profile and the dynamic tests are

presented in Chapter 11. Finally, the conclusions and further research topics are discussed in Chapters 12.

LITERATURE PART

2. Kaolin processing

The majority of kaolin clays are mined in open pits, since in most cases the cost of production and poor roof conditions prohibit underground mining of clay deposits. Since practically no deposits are naturally pure, the kaolin used by paper, ceramic and many more industries is processed further after mining. The calcined kaolin usually requires high quality grade kaolin as feed. According to Thurlow (2005), the kaolin to be calcined is obtained from the pits in by a method called wet processing, which results in better product compared to dry processing: higher uniformity, relatively free from impurities and better colour. The working of clay results in large quantities of side products. The ratio of kaolin to by-products is generally around 1:9. The common by-products are rock, sand and mica. Next, a common wet processing chain used to refine kaolin is described using the process flow description of the production chain located in Devon and Cornwall (Thurlow, 2005) as an example.

2.1. Process route from the pit to the calciner

Kaolin route from the pit to the calciner can be divided into three primary sections: pit operations, refining processes and drying processes. After these operations the processed kaolin is ready to be calcined. The next three sub paragraphs describe these three sections. The process flow diagram from the pit to the product is presented in Figure 1.

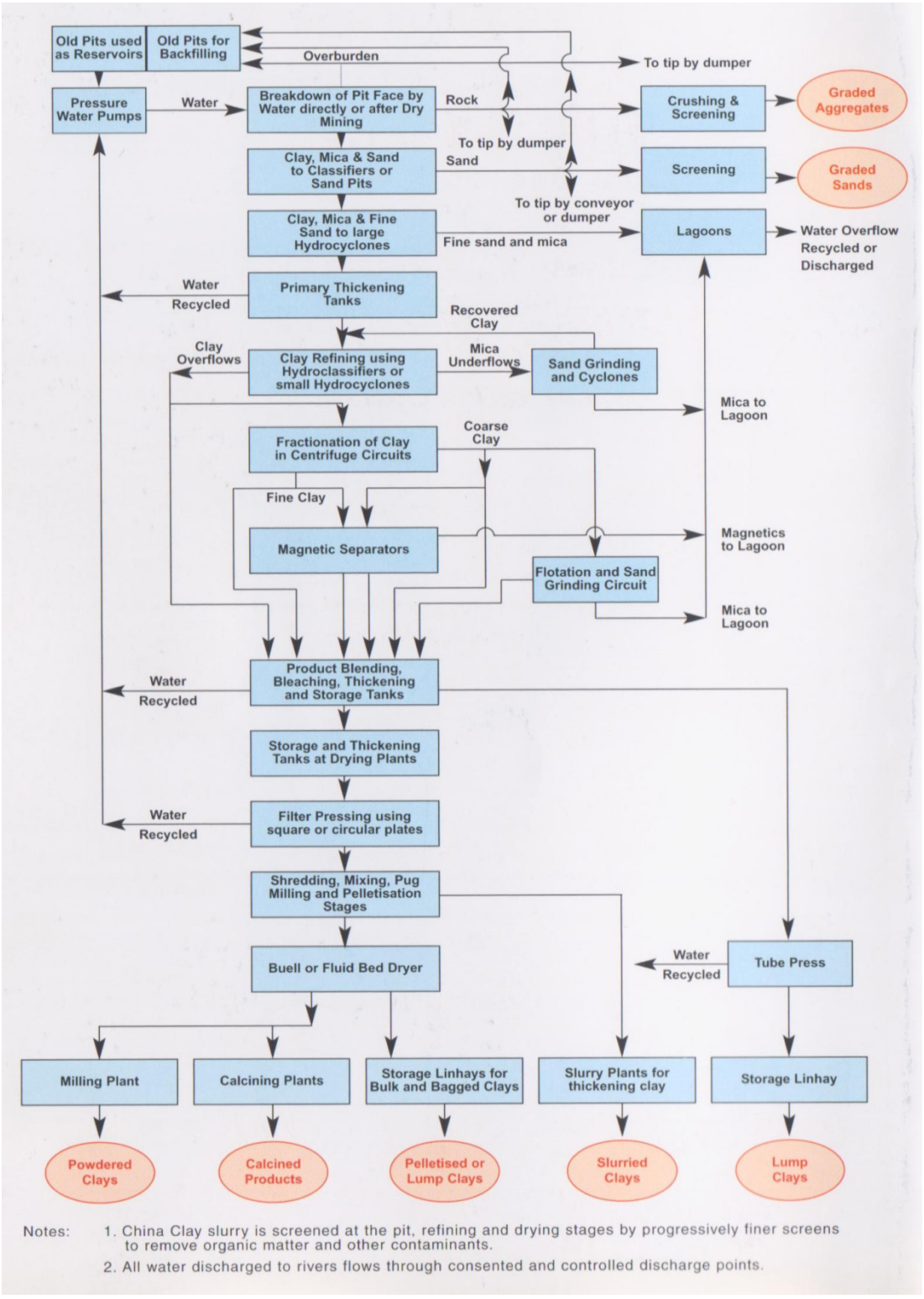

Figure 1. Simplified flow diagram of kaolin production (Thurlow, 2005).

2.1.1. Pit operations

Pit operations in an open-pit can be split into five different unit operations: removal of the over burden, breaking the hard ground, processing the clay face, removal of sand and separation of fine sand and coarse mica.

First, before the kaolin clay can be extracted from the soil, the overburden composed of topsoil, workable quality decomposed granite and brown stained layer of the same granite material has to be removed. This is executed by large shovel loaders and dumpers. The overburden can be used for landscaping work on sites where clay extraction has been completed.

Secondly, after removal of overburden, the hard ground is usually broken down by drilling holes of 150 mm in diameter and up to 15 m deep. The holes are filled with explosive emulsion and the ground is blasted. The drilling product can be used to analyse the quality of the clay. Next, the kaolinised granite can be either processed with dry mining or in a traditional way in the clay face processing phase.

Thirdly, in the dry mining process the kaolinised granite is taken to a 'make down' site where the material is washed, and stones and sand are removed. In the 'traditional method' clay face processing phase the blasted hard ground is directly washed at site, using a jet of water having a pressure up to 20 bars. Consequently, the stone material is separated as stones accumulate at the foot of the washing face. The side product, rocks, can be crushed and screened to various grades to be used in other industries.

The fourth stage of pit operations is the sand removal. The washed china clay, sand and mica form a suspension which flows to the lowest point of the pit. From there, it is pumped using centrifugal gravel pumps to a higher level and to a sand removal plant. Nowadays, the sand is separated either with bucket wheel classifiers or in large settling pits. The bucket wheel classifiers operate continuously and work in conjunction with conveyor belts. In the settling pits the sand is removed using

shovel loaders and dumpers. The extracted and classified sand can be sold for example to building industry.

The last step, before the actual refining stages, is the separation of fine sand and coarse mica from the clay. Before the separation, the clay, mica and sand suspension is pumped through long pipelines from a pit to refineries and drying plants with centrifugal pumps, for example in Devon and Cornwall over 200 miles of pipeline is used. The separation is performed after the moving of clay from a pit to refinery. The separation is done by hydrocyclones which divide the feed roughly into two grades; a particle size over 50 microns and particles having a diameter less than 50 microns. The smaller size grade is almost completely clay.

2.1.2. Refining processes

At the refineries, sand, mica and other impurities contained in the clay suspension are extracted to get a pure clay product. The refineries commonly have the following unit operations: thickening, mica separation, grinding, magnetic separation and bleaching.

Before any further refining processes can be performed, the clay has to be thickened. For the thickening, large circular tanks with diameters up to 43 meters are used. The clay suspension is pumped continuously to the middle of the tanks. In the tank, the clay settles down and is shifted towards the underflow pipe with slow moving raking arms. The settling of particles can be encouraged by introducing flocculent to the tank. The overflow water from the tanks is used at the washing process downstream. The thickened clay is tested for different properties, such as colour and particle size, and is then pumped from the tanks to the next stages of refining.

The second stage is the removal of fine mica. The fine mica particles are separated from the clay slurry using tanks (hydroclassifiers) or hydrocyclones. In the

hydroclassifiers process of de-flocculation is used and the particles are couraged to repel each other, by the addition of deflocculant. The fine mica particles are coarser than the kaolin and so mica settles down to the bottom of the tanks and it is removed from there by pumps. This step is repeated for the underflow to ensure better yield. Using hydrocyclones is an alternative for large tanks. To achieve reasonable tonnage, the clay feed is divided to a number of hydrocyclones. There are two sets of hydrocyclones utilized. The first set is 125 mm in an internal diameter and the second 50 mm. The overflow from the first set of hydrocyclones is re-treated with the set of smaller hydrocyclones. The underflows from both sets are retreated in a sand grinding process or are led directly to mica lagoons.

Some of the fine kaolin clay particles can form curled stacks of the same size as the rest of the underflow product from the hydrocyclones. Therefore, the underflow is led to the sand grinding stage to be grinded for a short period of time to break these clay stacks, but not to break the mica particles. The ground material is then classified by hydrocyclones and the finer clay overflow is added to the main kaolin flow. Next, the 'so far' refined clays will be ground, if it is desired that the final product has a particular fineness or 'aspect ratio'. The aspect ratio is the relationship between the length and thickness of clay particles, which relates to the amount of clay needed to coat paper.

The next separation step takes place after grinding the kaolin residue. Impurities in the refined kaolin, such as mica, iron oxides and tourmaline contain some iron. These minerals can cause specks in ceramics when fired and decrease the brightness of clay used for paper making. Therefore, they have to be removed. This can be performed with a powerful electromagnet.

There are two types of machines employed – one for coarse clays and one for fine clays. Both machine types use super-conducting electromagnet to give a high magnetic field with low electric current. This is achieved when working in a very low temperature of -267 °C. The machine used for coarser clays is a large electromagnet with a circular chamber in the centre filled with stainless steel wool, to which the

iron-particles attach. The machine operates in cycles of flushing and separation stages. The machine used for finer clays has a pair of reciprocating canisters. The canisters are packed with wire wool. The canisters are moved in and out of the magnetic field in turn so that the process can be considered almost to be continuous.

The last stage in the refining process is bleaching. The clay is frequently stained by iron oxides, hence a bleaching process is used to convert the insoluble iron oxides to iron sulphates using sodium hydrosulphite. Iron sulphite is less strongly coloured and much more soluble than iron oxides. Therefore, the iron is lost later on in the process when the clay is dewatered. In bleaching, the clay first passes through a tall column to remove trapped air and then flowing through a pipeline where the sodium hydrosulphite is added.

2.1.3. Drying process

The refined clay slurry is piped to a drying plant, where it is first thickened and then filter pressed to form a cake. The cakes are cut and fed into a mechanical dryer. The common mechanical dryers used in the process include square and circular filter presses and tube presses.

First, the clay from the refinery is thickened by sedimentation. Next, the clay is flocculated by using small amounts of acid to settle the clay quicker. Then clear water from the top of the tank can be removed.

After thickening the dewatered is continued by filter presses. In this process step the clay is pumped to under pressure into series of chambers lined with a tightly woven nylon cloth, which allows the water pass through it but not the clay particles. The chambers can be of a square or circular shape. A filter press has a line of plates placed together for a framework.

The filter presses with square plates have been used for long time and first the plates where manufactured from cast iron but nowadays they are polypropylene. The press with a circular plate is of newer design and its plates are made of steel. Both of the press types have around 120 plates per press. The clay cakes coming out from the presses have a water content of 25 - 30 percent. The circular press produces cakes with lower water content than the square presses since they can be operated with a higher pressure, respectively 68 bars and 15 bars. After pressing for one to two hours, the formed cakes are released. Another pressing method for coarser clay is the tube press. It allows usage of even higher pressures up to 100 bars and the water content can be reduced down to 18 %. The dewatered clay can be sold in this form or it can be moved further in the process to the dryers.

Before the pressed clay is introduced to dryers it can be milled with a pug mill to round the clay particles and to improve their flow properties. The milling operation is usually required for products used in paper industry as coating clay.

The final stage before drying is pelleting. First the clay is mixed in an enclosed trough with paddles which break down any lumps. Then clay is conveyed to a drum with a rotating vertical shaft carrying pegs known as a pelletizer. These form the clay into pellets about the length of half inch. This form is considered good for drying.

After pelleting the clay is dried. There are two existing dryer types, a Buell tray dryer and a fluidized bed dryer. The Buell tray dryer has been used for drying from the 1950s. It consists of thirty trays in a circular tower, rotated in a current of hot air, drawn into the dryer by fans. Each tray consists of several radial plates with gaps between them. Clay is fed to the top of the dryer and as the trays complete a full rotation the clay is pushed off by fixed arms onto the next level of plates. The retention time of the dryer is about 45 minutes after which the moisture content of the clay is around 10 %.

A more recent dryer application is a fluidized bed dryer where hot air is introduced slightly pressurized through a perforated floor in a cylindrical chamber. The pellets

of clay are fed onto the floor at the one end of the cylinder and they are moved by vibrating the floor to the other end while gradually drying. The fluidized bed dryer has two different operating configurations; separate cooling and combined cooling. When using the separate cooling, the clay is moved to another cylinder where it is cooled in atmospheric air. This process can handle about 6000 tons weekly. Operating with the combined cooling, the single fluidized bed is used for drying and cooling. This method is better suited for lower tonnages around 3000 tons per week. The fluidized bed combined with cooling provides lower dust levels outside by minimizing steam emissions from the dried product.

After drying, the kaolin can be milled to obtain the desired particle size. Now, the kaolin has been processed to a ready-product for a part of the applications and it can be sold. However, if the high quality grade products are required, the clay can be calcined to obtain higher brightness and lower soluble aluminium content.

2.2. Calcination

Calcination is a process used to produce value-added products, that was introduced in the early 1950s (Murray, 2007). Calcination is used to change the physical and chemical properties of various solid materials, such as minerals, metals, and ores, while removing gaseous decomposition products. The operation is usually accomplished in either rotary or large hearth furnaces, where the material is heated to temperatures up to 1500 °C. Besides using for kaolin processing, the most common calcination process is turning limestone, also known as calcium carbonate, into lime, or calcium oxide. In addition, recycling facilities use calcination to recycle metal waste products, like grindings, polishing mud, and slurries. Calcination can also be used to turn petroleum coke, a by-product from oil-distillation that contains a large amount of carbon, into a much purer form of carbon.

There are three different industrial calcination methods for kaolin: soak, batch and flash calcination. In soak calcination the kaolin is exposed to a high temperature for a prolonged time (over 30 minutes) to guarantee the level of calcination. During soak calcination the kaolin goes through total dehydroxylation under relatively slow heating (Slade et al., 1991). In the soak calcination the material is fed into a continuously working furnace, causing a large temperature difference between the kaolin and the inside of the furnace. On the contrary, in the batch calcination process the material is fed to a cold furnace and then the furnace is gradually heated to a desired temperature. Soak and batch calcinations lead to very much similar products. Their largest difference is in the operation capacity; batch calcination is for smaller amounts, offering better control over the heating rate and the temperature profile of the calcined material compared to the soak calcination method.

The flash calcination involves a rapid temperature increase usually from ambient temperature to 900 – 1000 °C. The heating happens within a fraction of a second, achieving a heating rate even as high as 100000 to 500000 °C per second (Thomas, 2010). Flash calcines are only partially dehydroxylated, which leads to totally different materials with differing physical characteristics. The steam evolved from the kaolin cannot escape from the particles, causing the formation of sealed blisters, which can be used to increase opacity of paints where the kaolin is used as a filler component. Also, metakaolin can be produced using flash calcination. This involves stopping the reaction at 800 °C when the material is highly reactive. The flash calcined product has much lower density than soak calcined.

3. Kaolin calcination

As natural product kaolin deposits vary in quality and quantity. Therefore, in order to produce uniform and specific engineered kaolin products, the physical, chemical, and mineralogical properties of the raw kaolin ore are evaluated. Brightness, particle size and shape, and viscosity are the most important physical properties to be measured. It is common in the kaolin industry to blend kaolins from different mines to achieve the desired properties. The physical and optical properties of kaolin such as particle size and shape, the particle size distribution and shape, brightness, colour, opacity, viscosity, surface area, dispersability, and hardness relate to their suitability for use as a pigment for coating paper. These properties can be altered by selective processing. (Murray & Kogel, 2005)

The brightness, opacity and abrasiveness of crude kaolin can be increased by thermal treatment. These products are utilized as coating pigments and functional fillers by the paper industry. The heat treated kaolin can be divided roughly into two grades. The first grade has increased brightness and improved opacity. At the temperature range of 450 °C to 700 °C kaolinite dehydroxylates, which breaks down the crystal structure of kaolinite leaving an amorphous mixture of alumina and silica which is called metakaolin (Murray & Kogel, 2005). This is a bulky product that is used as a paper coating additive to enhance resiliency and opacity in low basis weight sheets (Murray, 2005).

Heating kaolin further up to around 980 °C the amorphous mixture of alumina and silica reorganizes to form the so-called ‘spinel phase’. Heating the material even more, the spinel phase’s crystal structure changes again, forming small crystals of mullite and high temperature quartz (cristobalite). The spinel phase and the mullite form the second grade, in which the relict plates aggregate to form particles with an open structure that have relatively high light scattering coefficient. This standard calcined kaolin product has a brightness ranging between 92 and 94 % (Murray & Kogel, 2005). This grade’s surface chemistry and physical properties are completely

changed and it is whiter and more abrasive than the original kaolin. The abrasiveness of the calcined product is caused by the mullite and it can be reduced to acceptable levels by selecting the feed kaolin properly and carefully controlling the calcination and the final processing after calcination. This product can be used as an extender for titanium dioxide in paper coating and filling and in paint and plastic formulations (Murray, 2005). The two grades and their properties are compared in Table 1.

Table 1. Kaolin grades and changes in properties.

Kaolin	Calcination (grade 1)	Calcination (grade 2)
Brightness	Increased	Increased
Particle size	Changed	Changed
Particle shape	Changed	Changed
Opacity	Improved	-
Colour	-	Whiter
Viscosity	-	-
Specific surface area	-	Increased
Abrasion	-	Increased
Temperature range	500-700 °C	1000-1100 °C
Porosity	Increased with higher temperatures	

During kaolin calcination several chemical reactions and morphology changes occur in the raw material bed while it is moving through the calciner. The main five stages in kaolin calcination are (Ptacek et al., 2010):

1) Dehydration of absorbed water (T≤100 °C)

$$H_2O(l) \rightarrow H_2O(g) \qquad (1)$$

2) Dehydroxylation of kaolin and formation of metakaolin in the temperature range of 450-700 °C

$$Al_2O_3 \cdot 2SiO_2 \cdot 2H_2O \rightarrow Al_2O_3 \cdot 2SiO_2 + 2H_2O(g) \quad (2)$$

3) Formation of spinel phase at around 980 °C (925-1050 °C)

$$2(Al_2O_3 \cdot 2SiO_2) \rightarrow 2Al_2O_3 \cdot 3SiO_2 + SiO_2(amorphous) \quad (3)$$

4) Nucleation of the spinel phase and transformation to mullite (>1050 °C)

$$3(2Al_2O_3 \cdot 3SiO_2) \rightarrow 2(3Al_2O_3 \cdot 2SiO_2) + 5SiO_2 \quad (4)$$

5) Formation of cristobalite (≥1200 °C)

$$SiO_2(amorphous) \rightarrow SiO_2(cristobalite) \quad (5)$$

The stages 1 and 2 both give loss of weight on thermogravimetric (TG) curve shown in Figure 2 and the reactions are endothermic as shown on differential scanning calorimetry (DCS) curve in Figure 2. The total mass lost in calcination for kaolin is around 14 mass-percent. The steps 3 and 4 are exothermic reactions where the crystal structure of the metakaolin changes to a more stable state. The step five occurs only when heating to over 1200 °C, which in this particular process is not performed.

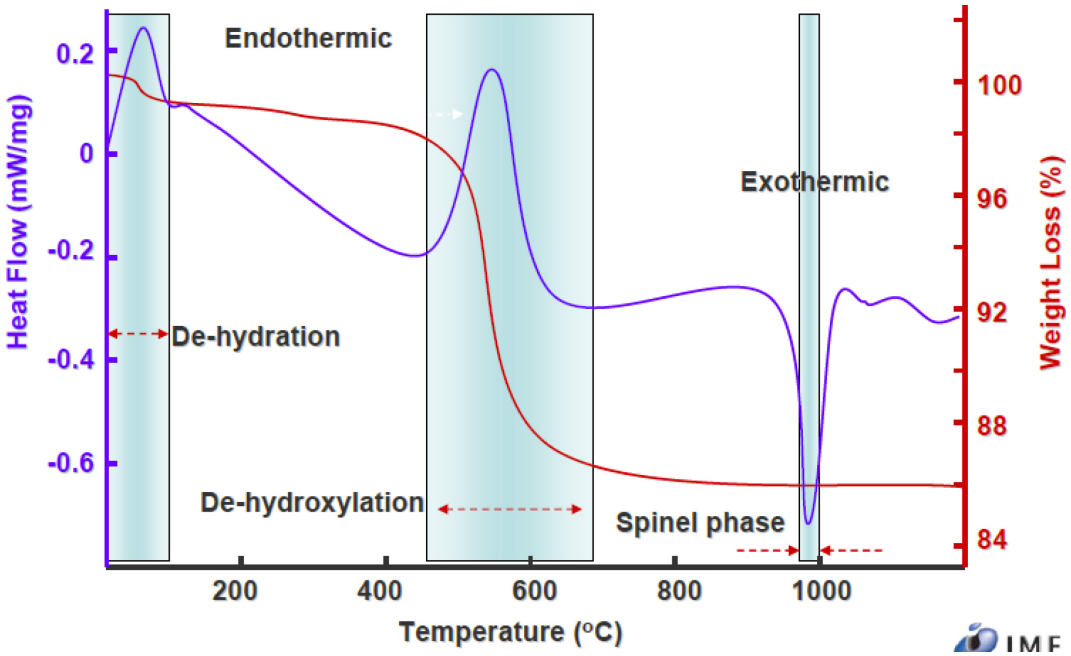

Figure 2. Thermal history of calcined clay (provided by IMERYS).

3.1. Heating rate effects

Castelein et al. (2001) studied the influence of the heating rate on the thermal changes of commercial kaolin. They concluded that kaolinite dehydroxylation, metakaolinite structure change, exothermic structural organization and mullite formation are very sensitive to the heating rate. The mullite growth below 1100 °C is the most effected phenomena, which is improved by increasing the heating rate from 3 to 20 °C/min. Therefore, it is very important to know what is the correct heating rate and then to be able to control the heating process as well as possible.

Langer (1967) stated that different heating rates have produced a marked effect on the area and temperature of the dehydroxylation peak of kaolinite. At the lower heating rates (10 to 20 °C/min), the incremental difference between successively determined peak temperatures is the greatest and the difference between the peak temperatures of the dehydroxylation curve tends to decrease with higher (40 to 50 °C/min) heating rates. The dehydroxylation reaction is said to be particularly

sensitive to a change in the heating rate because of the relationship between the build-up of vapour pressure and the reaction rate.

The kinetics of the spinel phase crystallization from medium ordered calcined kaolin were studied by Ptacek et al. (2010). They used differential thermal analysis to investigate the dependence of the exothermic peak of crystallization on heating rate. They varied the heating rate from 1 to 40 °C/min and found that the maximum temperature of the exothermic peak of spinel phase crystallization increases from the initial value of 947.4 °C to about 1001.6 °C. From the results presented in the article a simple correlation between the crystallization peak temperature and the heating rate (Φ) could be derived as (see Appendix 1)

$$T_{peak}(K) = 14.812 \ln(\Phi) + 1219.7 \qquad (6)$$

3.2. Particle size effect

The size and shape of the kaolin feed is a very important factor in calcination reaction. Kaolin having a fine particle size has a larger surface area meaning it will be much more reactive than coarse kaolin (Grim, 1962). Increased reactivity often leads to an increased rate of mullite formation.

As the particle size decreases, the size of the exothermic reaction (formation of spinel phase) and the intensity of the corresponding peak decrease. This is considered to be due to the decrease in crystal phase formation due the fragmented state of the particle (Thomas, 2010).

If the particle size increases, the dehydroxylation and other reactions take place much slower (Thomas, 2010). This phenomenon is met with particles larger than 20 μm and it is thought to occur because of the too small surface area for the dehydroxylation reaction to happen as rapidly as in finer particles.

The initial particle size of the kaolin also affects the particle size after the calcination. Two kaolins of a different particle size, medium and fine, were soak calcined and studied using electron microscopy. The variation in the products was noticeable. The fine kaolin produced a much smaller aggregate average size of 0.7 µm compared to medium kaolin's product of 1.2 to 2.2 µm in an average size. Also, the finer product had a higher void volume than the medium product, which affects the oil absorption capability of the product. This is because of the increased porosity. (Thomas, 2010)

The opacity, the ability to block light, improves as the particle size decreases. This is very important when the calcined kaolin product is used in paint formulation. Also, at the same time, gloss increases. (Thomas, 2010)

3.3. The effect of impurities to the colour of the calcined product

The impurities present in kaolin can be roughly divided into two categories; iron and organic components. The iron components make a huge difference when calcining kaolin compared to the organic components. Heating the clay matter to high temperatures causes the iron oxides to be oxidised from the green/blue Fe^{2+} to the red Fe^{3+} giving the product a shade of pink. Good correlations have been found between the measured iron content and properties of product, like brightness, yellowness and light absorption coefficients, to enable prediction of the colour of the product (Thomas, 2010).

Chandrasehar and Ramaswamy (2002) found out that kaolin having high iron content before beneficiation, but low after refining, is favourably comparable, in terms of brightness, with kaolin that had naturally low iron content once both samples had been calcined. The iron can be removed from clay by several methods, including magnetic separation and reductive chemical bleaching. Removal of iron

gives the kaolin a significant added value, but in many cases the separation is not cost effective.

The second category, organic material, can contaminate kaolin by natural and artificial means. Natural contaminants are mainly particles of wood, leaf matter and spores. Artificial contaminants refer to contamination by processing, for example, during the process route from a pit to refineries dispersants such as polyacrylate are added to prevent settling.

All organic components present in low temperature calcination (~700 °C) have a charring effect giving kaolin grey colour. However, when heating to a higher temperature such as 1000 °C, it has been generally determined that all organics are removed from the kaolin so that they do not have any effect on the final product (Thomas, 2010).

3.4. Morphology and structure studies in varying temperatures

Wang et al. (2011) studied the morphologies of the kaolin materials by scanning electron microscope (SEM). They compared four kaolin samples which where heated to four different temperatures: room temperature, 400 °C, 700 °C and 1050 °C. The SEM pictures revealed that kaolin has a layered structure and that layer stripping occurred at increased calcination temperatures. This was noted to indicate that a higher calcination temperature promotes lamellar layer formation and an increase in specific surface area. However, the clay structure collapsed at 1050 °C. Further in their research, Wang et al. examined the BET (Brunauer-Emmet-Teller model) surface area and porosity of kaolin. The BET surface area of the samples decreased with an increased calcination temperature, whereas the pore volume and the pore size increased on the contrary. It was concluded that well-ordered kaolin transformed to a less-reactive metakaolin with thermal treatment. Also, a loose structure brings a larger pore volume and a pore size. When compared with

other samples the sample calcined at 1050 °C showed significantly different properties. This suggests the formation of the crystalline phase and confirms the first four reactions described above.

Saito et al. (1996) studied the effects of calcination conditions on the properties of porous materials obtained from the selective leaching of calcined kaolinite. The following conclusions were drawn: first, by calcining kaolinite for 24 hours at various temperatures, mesoporous γ-Al_20_3 (spinel phase) was obtained in the temperature range from 900 to 1050°C and mesoporous mullite was obtained at 1100°C. Mesoporous γ-Al_20_3 obtained at 1000°C showed the sharpest pore size distribution, the highest specific surface area of 247 m^2g^{-1} and the highest pore volume of 0.84 mlg^{-1}. Secondly, by varying the calcination time at 1100°C, the crystalline phases in the porous materials changed from γ-Al_20_3 to mullite. A corresponding pore size increase, from 3 nm to about 6-10 nm, and a decrease in the specific surface area was observed. Clearly, then it can be said that the time kaolin spends in the exact calcination temperature must be determined correctly to obtain the desired kaolin structure and hence the correct product quality.

3.5. Residence time distribution

Residence time distribution is one of the key attributes to success regarding steady and unified level of calcination when producing calcined kaolin products. If the kaolin spends too long time in the furnace it will become over-calcined and forms abrasive mullite structure which can damage the process equipment. Thus the calcination reaction should be discontinued before significant mullite transformation. In the opposite case, when the calcination time is too short, the clay will stay at the metakaolin form which is not desired either. The rotational speed and the orientation of the rabble blades moved by the rabble arms can be modified to affect the residence time of the kaolin in the kiln.

Thomas et al. (2009) investigated the residence time of the Lee Moor multiple hearth furnace using mineral tracers. The researchers chose titanium dioxide (TiO_2) and talc ($Mg_3Si_4O_{10}(OH)_2$) as tracers, since those are not usually present in the kaolin fed to the furnace. The tracer material was added to the kaolin feed in a manner such that it was distributed as evenly as possible in the feed flow and was then dosed into the kiln in one portion.

First, the residence time distribution was examined using titanium dioxide. Samples were collected from both of the exit holes. The researchers noted from the results that there was only very little difference between the samples collected from the different exit holes meaning that there exists a good level of mixing in the furnace. Figure 3 shows the titanium dioxide content of the samples during the first test. Since the sampling results do not form a steady peak, the titanium dioxide tracer experiment indicated that plug flow does not occur in the furnace and there is a lot of small circulation and recirculation. This conclusion was also supported by the fact that during the sampling period only 33.6 % of the total added titanium dioxide had exited the kiln and it remained unknown how long it took for the rest of the titanium dioxide to exit the furnace. The difference in the specific gravity of titanium dioxide and kaolin was thought to be the reason for the results.

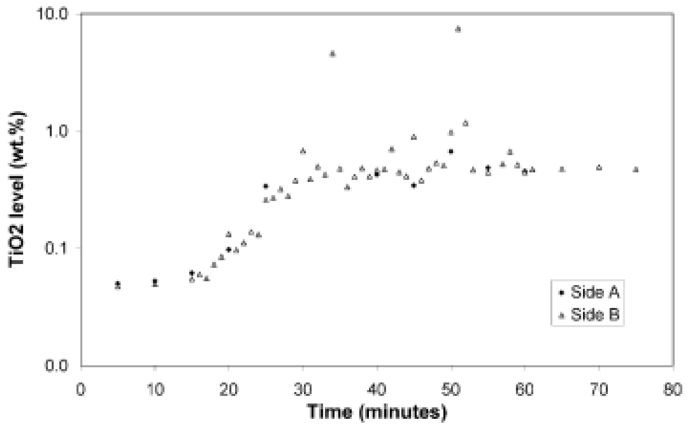

Figure 3. Variation of the titanium dioxide content of the calcined product sample after titanium dioxide was added to the feed.

Because of the poor results obtained by titanium dioxide, the residence time was next studied using talc, since it has almost an identical flow rate index value and a similar specific gravity value compared to kaolin. The results for the talc experiment are shown in Figure 4. The talc starts to appear at the drop hole after 20 minutes and all of the talc had passed through the furnace in 90 minutes. The peak amount of talc was detected at 43 min and the steady distribution peak suggests a plug-flow pattern flow in the furnace. However, Thomas et al.(2009) concluded, that as the width of the residence time distribution curve is over 60 minutes, the powder flow is not entirely uniform and the feed goes through the kiln in a more complex random path.

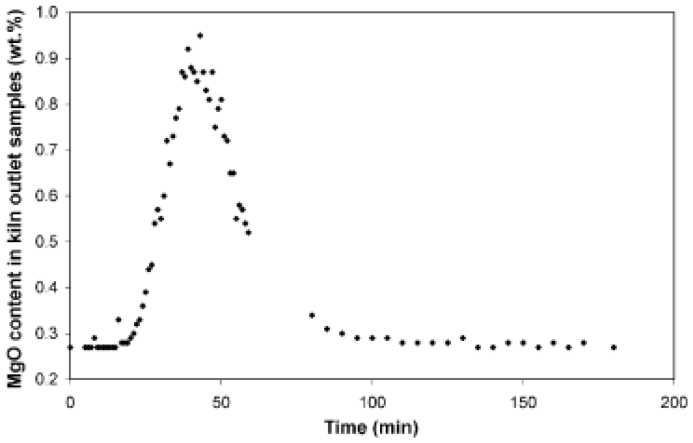

Figure 4. Graph showing change in the talc content (inferred by MgO content) of the calcined product during the talc tracer dosing experiment.

4. Mathematical models similar to the kaolin calcination

This chapter introduces five state-of-art mathematical models related to kaolin calcination found from the literature. No articles were found directly written on dynamic modelling of kaolin calcination in a multiple hearth furnace (MHF). However, five closely relevant articles are introduced. The first article presents a dynamic model of a roasting process to recover vanadium. The second article explains a rotary hearth coke calciner with one hearth. The third article presents a continuous plate dryer, which has a similar solids flow pattern as the Lee Moor MHF. The last two articles describe rotary kilns and dynamic modelling of the calcination process. These five cases introduce the concepts of calcination and the modelling aspect to be considered when developing a model of the MHF and kaolin calcination. Since the physical characteristics of the furnaces modelled in the reviewed articles are not exactly as in the MHF model more emphasis is given to the phenomena to be modelled and the mass and heat transfer equations that are required to build a model of the multiple hearth furnace.

Case 1 – Dynamic model of a roast process for simulation and control

Voglauer and Jörgl (2004) presented a dynamic model of a multiple hearth furnace used for the roast process to recover vanadium. The furnace configuration is very much similar as the Lee Moor Herreschoff furnace both having 8 hearths and counter current gas-solid flows. In addition, the model is used to simulate the temperature profile of the furnace, which is also an objective of the current work.

In the model each floor is divided into two layers – a gas and solid phase. Balance equations of mass, heat and components are described in both layers. For clarity, the model is divided into three interacting sections: a transportation model, a thermodynamic model and a chemical model (comprising the molar balances). This division is presented in Figure 5. The modelling work considered a few assumptions:

1) different floors contain homogeneous gas/solid layers in temperature and components. 2) Specific heat capacities, heat conductivities, etc. are considered constant.

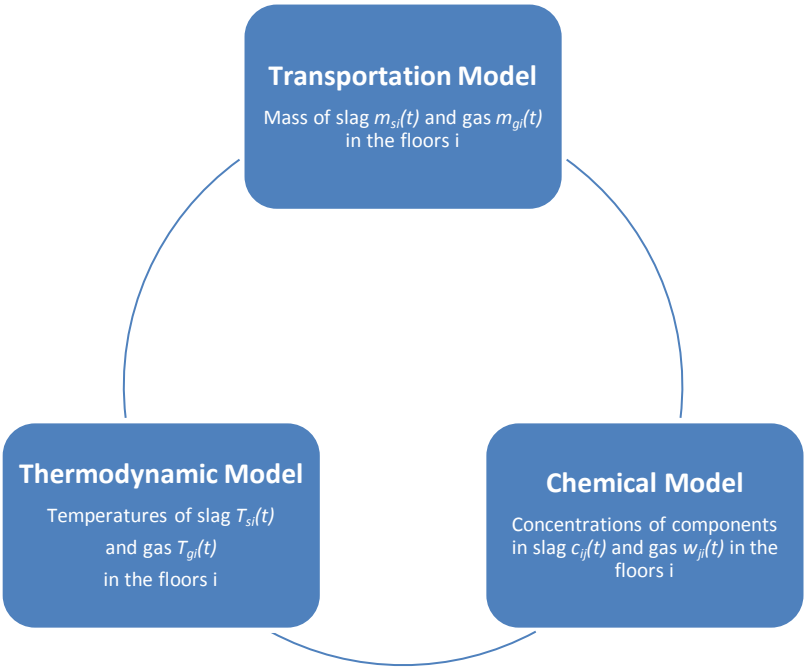

Figure 5. Overview of the model structure (Voglauer & Jörgl, 2004).

The transportation model is very simple; the global mass balance of the solid phase is only the total mass going in equalling the total mass coming out. The output is considered to be proportional to the central shaft rotating speed and to the mass of the solid layer. In addition, a transportation factor constant is used to calculate the output. The mass balance for the gas phase for individual hearth is the same as it was for the global mass balance. Additionally, the amount of the evaporated water was considered minimal compared to the overall gas flow.

The component molar balances are calculated for each main component; water, sodium, insoluble vanadium, and soluble vanadium. An assumption of approximate

stationarity was made for components in the gas phase, because the transient changes in concentration are rapid.

The components considered for the solid phase heat transfer are convective heat transfer due to mass exchange between hearths, heat of reactions, and heat of evaporation, heat transfer between the gas and the solid phase, heat transfer to the environment, heat transfer to the subsequent floor through the floor plate, and heat transfer to the central shaft. The temperature of the inner layer of the wall is assumed to be equal to the temperature of the slag on a particular floor. The heat transfer components considered for the gas phase are convection due to mass transfer of the gas from floor to floor, heat transfer from the gas to the solid phase, heat transfer to the environment, heat transfer from the gas to the previous floor through the upper floor plate and heat transfer to the central shaft. The temperature of the inner layer of the wall is assumed to be equal to the temperature of the gas on a particular floor.

The model included equations of drying and chemical reactions of vanadium. The drying kinetics consisted of the two phase drying rate derived from practical experiments. The first phase is a constant drying-rate-period, where surface water is available and evaporation depends only on environmental factors. The second phase was considered when the water content dropped under a critical limit. Then the drying rate was assumed to be proportional to the water content of the solid phase and to the mass transport from inside the porous media to the surface. The chemical reaction kinetic parameters were obtained by practical experiments. The model uses the Arrhenius law to describe the reaction rates. Also, adaptation parameters were used to compensate the difference between the laboratory scale results and the industrial plant data.

The dynamic solid bed mass balance considers inflow, outflow and evaporation. In the final model the slag layer in each hearth was considered homogenous whereas initially it was divided to several compartments. The initial assumption was neglected because of the enormous growth in computational effort and

considerably less increased accuracy of the model. Voglauer and Jörgl stated that many of the process phenomena can be described well if leaving only a few parameters for model adaptation to the special case (e.g. heat transfer). This is essential since only a few measurements are available. A model based on physical relations is flexible towards process modification.

The overall simulation model consists of seven essential state variables on each hearth. Since the range of variables differs strongly between different hearths, the differential equation system was scaled referring the states x_i to a typical set point values x_{i0}:

$$\bar{x_i} = \frac{x_i}{x_{i0}} \qquad (7)$$

The model was implemented in Simulink where the numerical integration of the state equations was carried out using the fixed step size Euler algorithm.

The model validation was carried out executing various experiments at an industrial scale plant. The validation was done for temperature on each hearth for gas and solid phase, residence time distribution, dynamic behaviour of temperatures of gas and solid phases, and for the component balance in terms of expected reduction in the recovery gain. The last validation proved to be a difficult task and it was stated that the results were not reliable for this section. The overall performance of the model was evaluated to be satisfactory and it was noted that to build this kind of a model, practical experiments are usually necessary. Interestingly, radiation was not considered in the heat transfer model. This was maybe due to the fact that the temperature should not rise over 850 °C in the furnace. Another questionable part of the model is the composition of the gas phase. It was not described, which components the gas phase included.

Case 2 – Mathematical modelling of a rotary hearth coke calciner

Meisingset and Balchen (1995) developed a mathematical model for a single hearth rotary coke calciner. Despite the fact that the model is only for one hearth this application is closely related to this Master's thesis work and has considerably well described equations and principles. The model was divided into three main sections, the coke bed, the gas phase and the lining including the floor, the roof and the walls above the bed. Mass exchange occurs between the solid and the gas phase whereas the heat exchange occurs between the bed, the gas phase and the lining.

The model considers three kinds of chemical reactions; the evaporation of the water, the release of volatile matter from the coke and the combustion of the volatiles and the fuel gases in the gas phase, coke bed combustion and dust generation. Each phenomenon, except the dust generation and the combustion of the coke bed, is described by the Arrhenius equation. As reviewing the article from the kaolin calcination point of view, the coke bed combustion is not an area of interest, but the dust generation is, since the Lee Moor plant has a bag filter collecting the kaolin particles from the exhaust gases. The simplified Equation 8 describes the dust generation considered in the model using the following variables; central shaft rotational speed (ω), gas density (ρ), velocity (v), gas temperature (T_g), coke moisture content (x_{H2O}) and a parameter k_d. The parameters k_d and m_i are estimated according the dust generation data.

$$g_d = k_d * T_g^{m_1} * v_g^{m_2} * \rho_c^{m_3} * x_{H_2O}^{m_4} * \omega^{m_5} \qquad (8)$$

The coke bed is considered as a packed bed of porous particles of different shapes and sizes, and only bulk phenomena are taken into account. The rabble arms are assumed to cause an axial coke bed mixing and no back-mix flow is considered to occur. Figure 6 presents the movement of the solid bed. After one full rotation of

the central shaft, the coke particles are moved to the next concentric path. The area of each path is considered to be equal and so the width of the paths increases inwards.

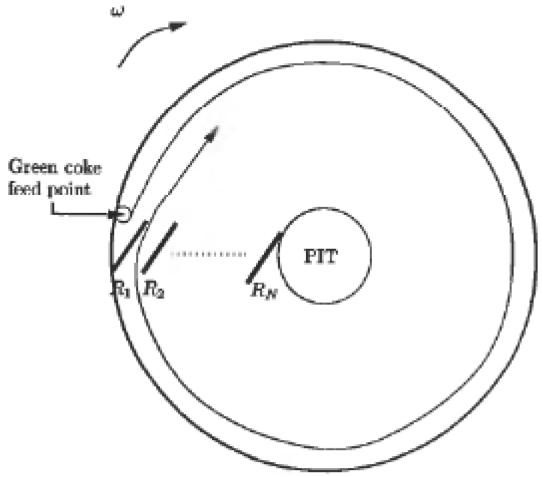

Figure 6. Overview of the rotating coke bed. The coke is moved in concentric paths. R_i denote the rabbles.

The mass balance of the model is written as a function of polar coordinates and the height of the bed. The bed density is assumed to be constant for simplification and some boundary conditions are considered. The mass loss due to the coke combustion and the dust generation are taken into account, since it reduces the height of the bed. Also, individual component balances for coke components; H_2O, H_2, CH_4 and $C_{18}H_{12}$ are calculated. The coke bed energy balance is modelled considering the plug-flow assumption and the coke heat capacity is assumed to be temperature dependent.

The gas phase is considered as a combustion chamber, which serves as a heat exchanger. The model does not describe the gas flow pattern since it is not the main aim of the model. The gas phase consists of air, volatiles, water from evaporation, fuel gas and the combustion products. A steady-state model was used for the gas phase since the changes in the gas phase are much faster compared to

changes in the solid bed. The gas flow is considered to occur only in the radial direction. Perfect mixing is considered in the axial and in the angular direction due to the turbulence in the gas flow. Radial flow with radial mixing was modelled as a series of mixed vessels of different volumes with internal back-mix flow. The authors mentioned that a plug flow model with a dispersion term could also be used. The mass balance for the total gas system and for the individual components is implemented in the model. The energy balances are modelled for each vessel separately considering the case of no phase change and neglecting the variations in the total pressure and the work term.

The heat transfer model involves all three forms of heat transfer; conduction, convection and radiation. The Figure 7 presents the heat transfer scheme in the model. Also, heat conduction in the bed, in the lining, and heat transfer to the water cooled rabble arms are considered.

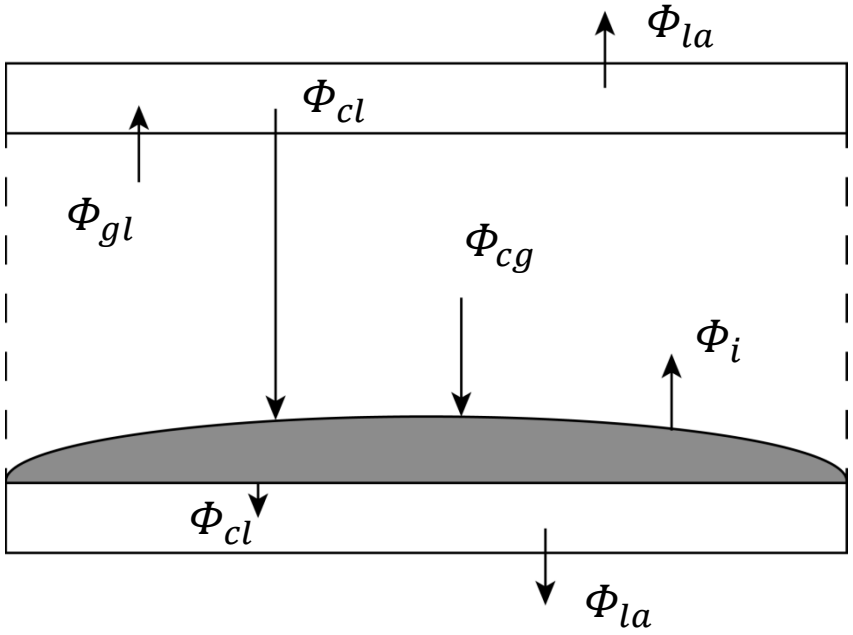

Figure 7. Heat transfer between the coke bed, the gas phase and the lining (Meisingset & Balchen, 1995). Φ_{cg} is the radiant and convective heat flux between the gas and the coke bed. Φ_{gl} is the radiant and convective heat flux between the gas and the lining. Φ_{cl} is the radiant and conductive heat flux between the coke bed and the lining. Φ_{la} is the radiant and convective heat flux between the lining and the ambient air. Φ_{cg} is the heat flux due to evolution of component I from the coke bed to the gas.

Heat conduction is included between the solid bed and the lining, but it is neglected in the gas phase. The conduction is assumed to be one dimensional for both the solid bed and the lining. The coke bed was assumed to be thermally thick medium using the dimensionless Biot-number.

$$Bi = \frac{hV}{kA} \tag{9}$$

Where h is the heat transfer coefficient for the heat flux from the gas phase or from the lining to the coke bed, V is volume, A is area and k is the thermal conductivity of the bed. If the Biot-number is over one, the assumption of the thermally thick medium is justified. The effective heat transfer coefficient of the coke bed is due to both radiation and convection. However, due to the high temperature in the furnace, radiation dominates as the heat exchange mechanism and the heat transfer coefficient is approximated by

$$h_{eff} = \epsilon_g \frac{(\epsilon_c + 1)}{2} \sigma \frac{T_g^4 - T_c^4}{T_g - T_c} \tag{10}$$

Where ϵ is emissivity, σ Stefan-Boltzmann constant and T is temperature. The coke bed effective heat conductivity accounts for solid conduction and inner particle radiation and neglects the gas conductance

$$k_{eff} = (1 - \sqrt{1 - \varepsilon_b} k_R + \frac{\sqrt{1 - \varepsilon_b}}{\frac{1}{k_R} + \frac{1}{k_P}} \tag{11}$$

Where ε_b is the bed voidage and k_R is due to radiation (Meisingset and Balchen, 1995, page 202). The k_P is the thermal conductivity for a particle with porosity.

The lining is considered as two parallel plates, first one representing the roof and the wall above the coke bed, and the second one represents the floor. The following assumptions where used in the model; the lining is geometrically approximated by an infinite plate, since the lining is not very thick, the temperature gradient of the steel shell is neglected, and the thermal properties of the brick material are constant.

Convective heat transfer occurs in the model between the gas phase and the lining, the gas phase and the bed surface, and the lining and the ambient air. The convective heat transfer coefficients are calculated from the Nusselt, Reynolds and Prandtl numbers.

The radiative heat transfer has the following assumptions: the coke bed and the lining are grey and opaque, and the gas is grey, transmitting and non-reflecting. The model assumes that the furnace length in the direction of gas flow is large compared to its height so that the net radiative flux in the gas-flow direction can be ignored and only the flux in the direction of normal to the flow is considered. The radiation is simplified assuming that the surfaces are dark grey.

The simulation model uses finite difference methods to solve the dynamic partial differential equations. In the article there was no validation of the model. However, the simulation results obtained seemed to be rational and correctly behaving.

Case 3 – Mass and heat transfer in a continuous plate dryer

Liu and Jiang (2007) presented a mathematical model for a continuous plate dryer considering mass and heat transfer in the dryer. The material flow path is similar to the one in the multiple hearth furnace but the heating mechanism is different. The

heat transfer is accomplished only by conduction between the heated plate surface and the solid bed. Therefore, the mass transfer model described in the article is reviewed whereas the heat transfer model is not.

The mass transfer model considers the following assumptions. Whenever a heap of particles is being formed, the angle of inclination of the free surface to the horizontal dimension can take any value up to a maximum, which is called the angle of repose. In the model, the angle of repose is supposed to be constant during the drying procedure, and the angle can be measured by an experiment. On the plate, there is several annular granular heaps with a isosceles-triangle section. For each heap, there are a corresponding feed-in plow and a take-away plow. For example, in Figure 8 illustrating the particle movement model on a large heating, the inferior plow is a feed-in plow of the second heap near the external rim, and the left plow is a take-out plow. Circle mid-line of each heap is supposed to coincide with one edge of the corresponding feed-in plow, which can be considered as the projection of the top point of the annular granular heap. The annular heap is composed of two segments with different cross-sections. The first segment type B-B, shown in Figures 8 and 9, locates from the position of the take-away plow to the feed-in plow in the rotation direction of central shaft. The bottom angle of the B-B section is equal to the angle of repose. The second segment type A-A, also shown in Figures 8 and 9, has a smaller surface area. The transient section at the sweeping moment is presented in Figure 9.

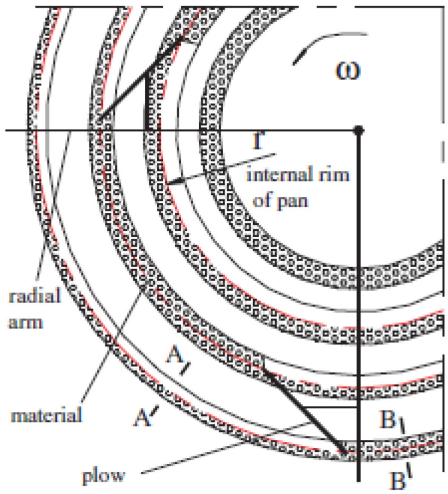

Figure 8. Sketch diagram the of model the of particle transfer on the heating plate (Liu & Jiang, 2007).

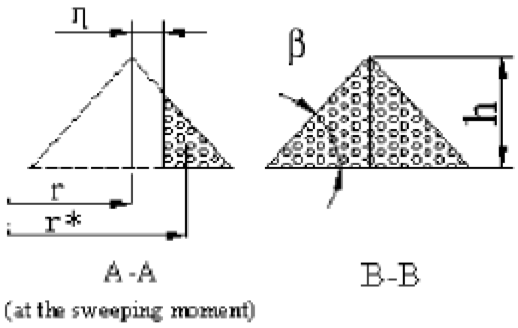

Figure 9. Cross section of annular granular heaps (Liu & Jiang, 2007).

Next, the mass transfer model is introduced in detail. When the sum of plow sweeping areas equals the surface area of the heating plate, one edge of the take-away plow coincides with the circle mid-line (η=0 in Figure 10). Figure 9 (the left part) presents a case where the total sweeping area is larger than the plate surface area, and the swept area of feed-in plows overlaps with the sweeping area of take-away plows. An overlapping ratio ϑ, describing the difference between the combined width of plows in a radial direction and the radial width of the heating plate, is introduced and it is defined as

$$\vartheta = \frac{nLcos(\varphi) - R + r_0}{R - r_0} * 100\% \qquad (12)$$

where n is the number of the plows on one plate (number of the plows in one rabble arm), L is the width of the plow, φ is the installment angle of the plow, R is the external radius of the heating plate and r_0 is the inner radius of the heating plate. For example, if the summed width of the plows in the radial direction and the radial width of the heating plate equal, then the overlapping ratio is 0.

For simplification, a parameter η presenting the difference between one edge of the take-away plow and the circle mid-line of an annular heap is defined:

$$\eta = \frac{\vartheta(R - r_0)}{n}\left[= \frac{nLcos(\varphi) - R + r_0}{R - r_0} * \frac{(R - r_0)}{n} = \frac{nLcos(\varphi) - R + r_0}{n} = Lcos(\varphi) + \frac{r_0 - R}{n}\right] \qquad (13)$$

For each annular heap, the feed in mass should equal to the amount of material swept away resulting in mass balance equation (14). The first left hand side term of equation (14) presents the half of the volume of annular heap as the B-B section, and the second term is the volume of the smaller annular heap of the A-A section.

$$2\pi\omega r h^2 c \ \tan\beta - \pi\omega r^*(hc\tan\beta - \eta)^2 \tan\beta = \frac{m}{\rho} = V, \qquad (14)$$

where ω is the rotation speed of the central shaft, r is the radius of the mid-line circle of the heap, h is the height of the heap, c is $\frac{1}{(\tan\beta)^2}$ and r* is the radius of the gravity center position of the A-A section

$$r^* = r + \eta + \frac{1}{3}(hc\tan\beta - \eta) = r + \frac{1}{3}hc\tan\beta + \frac{2}{3}\eta \qquad (15)$$

In the above equations 14 and 15 the $(hctan\beta - \eta)$ presents the width of the A-A section. The width (=2hctanβ) of an annular heap is usually much smaller than the radius of the circle mid-line of the annular heaps. Therefore following simplification is made

$$r^* = r \qquad (16)$$

Rearranging the mass balance formula (14) gives the height of each heap in the case of η ϵ (0,hctanβ):

$$h = \sqrt{\frac{m\tan\beta}{\pi\omega r\rho} + 2\eta^2\tan^2\beta} - \eta\tan\beta, \qquad (17)$$

where m is the feed in rate. The mass balance equation 14 is based on η ϵ (0,hctan β). When η_c = hctan β, thus the plow sweeps the whole heap, the critical overlapping ratio ϑ_c then becomes

$$\vartheta_c = \frac{n}{R - r_0}\eta_c = \frac{n}{R - r_0}\sqrt{\frac{mc\tan\beta}{2\pi\omega r\rho}} \qquad (18)$$

when $\eta < -hc\tan\beta$, the heaps cannot be swept away by its take-away plow, and no mass transfer occurs. If $0 > \eta > -hc\tan\beta$, $\vartheta \in (-\vartheta_c, 0)$, the plow sweeps less than half of the heap and the mass balance equation takes the form of

$$\pi\omega r(hc\tan\beta + \eta)^2\tan\beta = \frac{m}{\rho} = V \qquad (19)$$

While $\frac{R-r_0}{n} > \eta > hc\tan\beta$, $\vartheta \in (\vartheta_c, 1)$, the plow sweep width is greater than the heap width and the mass balance can be written as

$$2\pi\omega r h^2 c\tan\beta = \frac{m}{\rho} = V \qquad (20)$$

Expression for height of the large section segment of the annular heap can be obtained by solving Equations 18, 19 and 20 and combining them as

$$h = \begin{cases} \sqrt{\dfrac{m\tan\beta}{\pi\omega r\rho}} - \eta\tan\beta & \vartheta \in (-\vartheta_c, 0) \\ \sqrt{\dfrac{m\tan\beta}{\pi\omega r\rho} + 2\eta^2\tan^2\beta} - \eta\tan\beta & \vartheta \in (0, \vartheta_c) \\ \sqrt{\dfrac{m\tan\beta}{2\pi\omega r\rho}} & \vartheta \in (\vartheta_c, 1) \end{cases} \qquad (21)$$

Likewise, for the expression of the height of a the small section segment (A-A section)

$$h' = \begin{cases} \sqrt{\frac{1}{2}(h^2 - 2h\eta\tan\beta - \eta^2\tan^2\beta)} & \vartheta \in (-\vartheta_c, 0) \\ \frac{\sqrt{2}}{2}(h - \eta\tan\beta) & \vartheta \in (0, \vartheta_c) \\ 0 & \vartheta \in (\vartheta_c, 1) \end{cases} \quad (22)$$

The total amount of product bulks on a plate can be calculated in terms of the corresponding parameter h. On steady operation, the product volume in one annular heap is of form

$$v_i = \begin{cases} \pi rc\tan\beta\,[2h^2 - \theta(h + \eta\tan\beta)^2] & \vartheta \in (-\vartheta_c, 0) \\ \pi rc\tan\beta\,[\theta(h - \eta\tan\beta)^2 + 2(1-\theta)h^2] & \vartheta \in (0, \vartheta_c) \\ 2(1-\theta)\pi rc\tan\beta\,h^2 & \vartheta \in (\vartheta_c, 1) \end{cases}, \quad (23)$$

where θ is the plow-setting coefficient, which is defined as $\frac{1}{2}\pi$ times the angle from the feed-in plow to the take-away plow in the central shaft rotation direction. It is a function of the number of arms and setting order of plows.

On the assumption the volumes of various heaps are equal, the total bulk on a plate can be written as

$$V = \sum_{i=1}^{n} v_i \approx nv_i \quad (24)$$

The retention time of the material on a plate is defined as

$$t = \frac{V\rho}{m} = \frac{n\rho v_i}{m} \tag{25}$$

Eliminating v_i from Equations 21, 22, and 23 results in an expression for the retention time in terms of h

$$t = \begin{cases} \dfrac{2\pi r n \rho c \tan\beta}{m} h^2 - \dfrac{\theta n}{\omega} & \vartheta \in (-\vartheta_c, \vartheta_c) \\ \dfrac{n}{2\omega} & \vartheta \in (\vartheta_c, 1) \end{cases} \tag{26}$$

Consequently, the retention time for the whole dryer is

$$T_{tot} = \sum_{j=i}^{K} t_j \tag{27}$$

In general, because of the clearance between the annular heaps, the product-covering area is less than the plate surface area, and so the product covering area is the effective heat transfer area. Consequently, the ratio of these two areas partially represents the performance of a plate dryer. The effective covering ratio μ may be expressed as

$$\mu = \sum_{j=1}^{k} \sum_{i=1}^{n} \frac{4\pi r_i [\theta h_i + (1-\theta) h_i']}{\pi\left(R_j^2 - r_{0,j}^2\right)} \tag{28}$$

The effective covering ratio is expected always to be less than unity. A good design should provide the maximum of μ in a given feed rate.

The above equations assume that no overlapping between the adjacent heaps occurs. However, according to Equation 23, the width of a heap increases as the feed-in rate increases resulting in the overlapping of adjacent heaps, if the feed rate is high enough. Setting $r_{i+1} - r_i = (h_i + h_{i+1})ctg\beta$ gives the formula for the critical feed-in rate m_c

$$m_c = \begin{cases} \pi\omega\rho \tan\beta\, r_i r_{i+1}(r_{i+1} - r_i + 2\eta)^2 & \vartheta \in (-\vartheta_c, 0) \\ \frac{1}{8}\pi\omega\rho \tan\beta\, (r_i + r_{i+1})[(r_{i+1} - r_i + 2\eta)^2 - 8\eta^2] & \vartheta \in (0, \vartheta_c) \\ \dfrac{2\pi\omega\rho \tan\beta\, r_i r_{i+1}(r_{i+1} - r_i)^2}{r_i + r_{i+1} + 2\sqrt{r_i r_{i+1}}} & \vartheta \in (\vartheta_c, 1) \end{cases} \quad (29)$$

when $m > m_c$, the equations will become complicated. However, in general processing conditions the feed-in rate is much lower than the critical feed-in rate. Therefore, all equations of the current article are based on the assumption of $m < m_c$.

Case 4 – Dynamic modelling of a rotary kiln for calcination of titanium dioxide white pigment

In a recent work by Ginsberg and Modigell (2011), a dynamic model of a rotary kiln used for calcination of titanium dioxide is developed. The rotary kiln itself is different to the multiple hearth furnace, but the overall heat transfer phenomenon and the reactions occurring are very much similar and therefore the article is reviewed.

The heat transfer model comprises of six heat transfer paths, which are shown in Figure 10. Direct heat transfer from the gas phase to the wall is considered to occur by radiation and convection. Same mechanisms are expected to occur between the gas phase and the solid phase, and between the outer kiln shell and the environment. Heat is also transferred by radiation from the kiln inner wall to the solid bed and from the inner surface of the wall to the outer surface of the kiln by conduction. In addition, heat is regenerated from the gas side wall surface to the solid side wall surface, meaning that as the kiln rotates the wall contacted with the gas is 'charged' with heat which is then released again in contact with the solid.

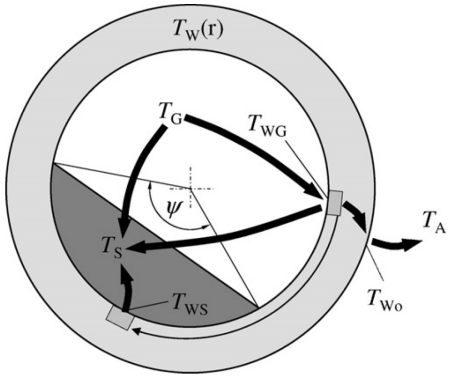

Figure 10. Heat transfer paths in rotary kiln cross section (Ginsberg & Modigell, 2011).

The convection heat transfer coefficient between the gas phase and the solid bed is adapted to measurement results as a fixed value. The heat transfer between the wall and the solid bed is considered to be formed from two parts: contact resistance between the wall and the solid bed, and the bulk penetration resistance. The heat transfer coefficient between the kiln outer shell and the environment is calculated with a method that accounts for the both forced and free convection. The kiln is regarded as a grey body regarding the radiative heat transfer to the environment. The temperatures for the gas phase, the solid bed, the gas side wall, the solid side wall and the kiln outer shell are solved from energy balance equations for each axial

position z. The axial components of the radiative and conductive heat transfer are neglected due to the former research for simplification of the modelling.

Five different reactions occur in the TiO2 calcination process, first the evaporation of the moisture, second and third the removal of adsorbed water, fourth the removal of sulphate groups, and fifth the phase transformation from anatase to rutile. The evaporation of the free water is considered to be entirely heat transfer controlled. The evaporation is assumed to start once the solid temperature reaches 100 °C and the solid temperature does not rise before all of the free water has been evaporated. The influence of pore-diffusion controlled drying is neglected entirely. The four latter reactions are kinetically limited. Their reaction kinetics is described by Equation 30:

$$\frac{d\vartheta_i}{dt} = A_i \left(-\frac{E_{A,i}}{RT_S}\right)(1-\vartheta_i)^{n_i} \qquad (30)$$

where A_i is the frequency factor for reaction i, E_i is the activation energy for reaction i, R is the gas constant, T_S is the solid bed absolute temperature, n_i is the order of reaction, and ϑ_i is the degree of conversion for reaction i. The kinetic parameters were studied by Ginsberg and Modigell in another article (Ginsberg et al., 2011) by DTA-TG-MS-measurements. The reaction enthalpies and kinetic parameters for reactions 2 to 5 were obtained from those experiments.

The mass transfer model of the rotary kiln is not deeply discussed here, since it differs from the MHF. The gas phase and the solid bed are assumed to be uniform in each kiln cross sections due to the turbulent gas flow and kiln rotation. Hence, the temperature and the composition gradients can be considered only in the z-direction, which is the direction of the kiln length. The model contains the molar balances for each of the components. The z-directional velocity of the bed is calculated using angle of repose and the porosity of the material. For the porosity, a

mean value is considered over the whole length of the kiln. Also, an axial dispersion coefficient is used to formulate the dispersive flux. The gas phase is assumed to have a very high velocity compared to the solid phase. Therefore, the gas phase is modelled with a steady-state model and no transient terms are used for the gas mass balances.

The kiln is operated slightly under pressured, as is the Lee Moor MHF, causing false air to enter the kiln through leakages, mostly from the discharge hopper. The amount of false air depends directly on the inner kiln depression Δp:

$$\dot{V}_{FIA} = K_{FIA}\sqrt{\Delta p} \qquad (31)$$

The constant K_{FIA} describes the flow conditions within the discharge hopper. It is determined from the volumetric balance over all gaseous input and output streams.

The numerical solution for the model is obtained by using finite difference methods. The kiln is divided to 100 and 5 equidistant elements in z and radial directions, respectively. Backward Differentiation Formulae (BDF) is used to execute the integration of the model in time.

A steady-state sensitivity analysis revealed that the temperature of the exiting gas flow is not very sensitive to variations whereas the clinker temperature is, as a result of the strong temperature increase towards the kiln end. The model is also tested for dynamic responses showing good performance.

Case 5 – Modeling and simulation of petroleum coke calcination in rotary kilns

Martins et al. (2001) developed a one-dimensional mathematical model for the simulation of petroleum coke calcination in rotary kilns. As with the former example the kiln is different to the MHF but the phenomena are very much similar with the process in hand. The calciner model is used to predict the temperature profiles and the composition profiles for the solid bed, the gas phase and the kiln inner wall in the axial direction. The axial flow modelling also considers some rheological properties of the particle bed. The model is discussed here on the relevant parts considering the Master's thesis.

The model regards the mass transportation between the solid phase and the gas phase including the combustion of methane, the release of the volatile matter, the coke combustion and the release of the coke particles into the gas phase. The main factors influencing the solid motion in the axial direction are identified to be the bed height variation, the particle fluidization caused by the flow of the volatile components released from the bed and the dependency of the properties on the temperature.

The convective heat fluxes between the gas phase and the solid bed, and the gas phase and the kiln inner wall are modelled applying Equation 32:

$$Q = hA(T_g - T_k) \qquad (32)$$

where h is the convective heat transfer coefficient. The heat transfer coefficients are evaluated from experimentally determined equations comprising the dimensionless Reynolds number.

The radiative heat flux between the solid bed and the kiln internal wall was evaluated by Equation 33:

$$Q = \sigma A \varepsilon_w \varepsilon_s (1 - \varepsilon_g) \Omega (T_w^4 - T_s^4) \quad (33)$$

where Ω is the form factor for the surface between the kiln internal wall and the solid bed. The conductive heat transfer coefficient between the coke bed and the kiln internal wall was evaluated by an empirical correlation.

The radiative heat transfer between the gas phase and the solid bed, and between the gas phase and the kiln internal wall are evaluated by Equation 34, which is applicable for ε ≥ 0.8.

$$Q = \sigma A \frac{(\varepsilon_k + 1)}{2} (\varepsilon_g T_g^4 - \alpha_g T_k^4) \quad (34)$$

where σ is the Stefan-Boltzmann constant, A is the heat transfer area, ε is the emissivity, T is the absolute temperature, α is the absorptivity. The subscript g stands for gas and k for solid or wall.

The energy balances are written assuming negligible viscous dissipation and insignificant variation in the kinetic and the potential energy. The heat losses to the environment from the external kiln wall occur by radiation and convection. The model considers both, forced and natural convection, depending on the environmental conditions.

The kinetics of the water release from the coke bed are described by a first-order equation

$$R_e = k_0 \left(\frac{X_c G_c}{u_b} \right) X_e e^{-\frac{E}{RT_s}} \quad (35)$$

where k_0 is the characteristic constant, E is the release energy, X_c is the coke mass fraction in the bed, G_c is the coke mass flow rate, u_b is the velocity of the bed and X_e is the external water mass fraction. Also, the reaction rates of the combustion of the volatiles are described by empirical Arrhenius-like equations.

Part of the coke particles are released from the bed to the gas phase due to high turbulence in the gas flow inside the kiln. This phenomenon clearly has similarities to the work on hand, where some of the kaolin powder is lost to the gas phase as a result of fast flowing gas phase. The kinetics of the release of the coke particles to the gas phase are evaluated by Equation 36:

$$R_p = 2K(2\omega G_c R_i)^{½} T_g^{\frac{3}{4}} * [u_g \rho_g R_i^2 (1-\eta)]^{½} \qquad (36)$$

where K is a characteristic constant, ω is the kiln rotational speed, ρ_g the density of the gas phase and η is the fraction of solids fill. The equation is based on the two distinct mechanisms of the release of the bed particles into the gas phase; particle drag due to fall and particle drag due to vortex in the gas phase.

Case 5.1 – Solution methodology of the coke calciner dynamic model

Martins et al. also discussed the different solution methodology for counter current models. Two main approaches exist; the first approach solves the ordinary differential equations simultaneously in the axial direction for the both solid and gas phases. The second approach solves the equations in an iterative manner, first for one phase in the direction of the solids flow and secondly for the other phase in the opposite direction. Martins et al. refer to Franks (1972) where these two solution methods are discussed comparatively.

Franks (1972) noticed that the simultaneous solution of the model equations for both directions of the flow requires a good estimation of the initial values for the dependent variables in the equations describing the flow in the opposite direction to the axial direction. Such solution method also presents convergence problems if there are steep gradients in the source terms.

The iterative method first solves the equations for the solid flow in its movement direction and then for the gas phase in its movement direction. Because the equations for both phases are coupled, the initial values for the gas phase have to be guessed. After solving the equations for the first time for the solid phase, the equations for gas phase are solved using the newly calculated values of the solid phase. After the equations for the gas phase are solved, the solution methodology is re-started. The iteration procedure is repeated until convergence limits are satisfied for both of the phases. Solving the model equations iteratively can take a while, but the iterative method can solve the equations without a good estimate of the initial values. In addition, the calculation time can be decreased with good initial value guesses.

Figure 11 presents the modelling scheme of the coke calciner model. As there is much interaction between the sub-models Martins et al. implemented the iterative solution procedure. They tested several numerical methods to solve the ordinary differential equations, including the fourth-order Runge-Kutta, the fourth order Adams-Bashforth/Adams-Moulton prediction-correction method and the Hamming prediction-correction method. All of the methods were reported to give similar performance. Eventually the fourth-order Runge-Kutta was chosen for its simplicity compared to others.

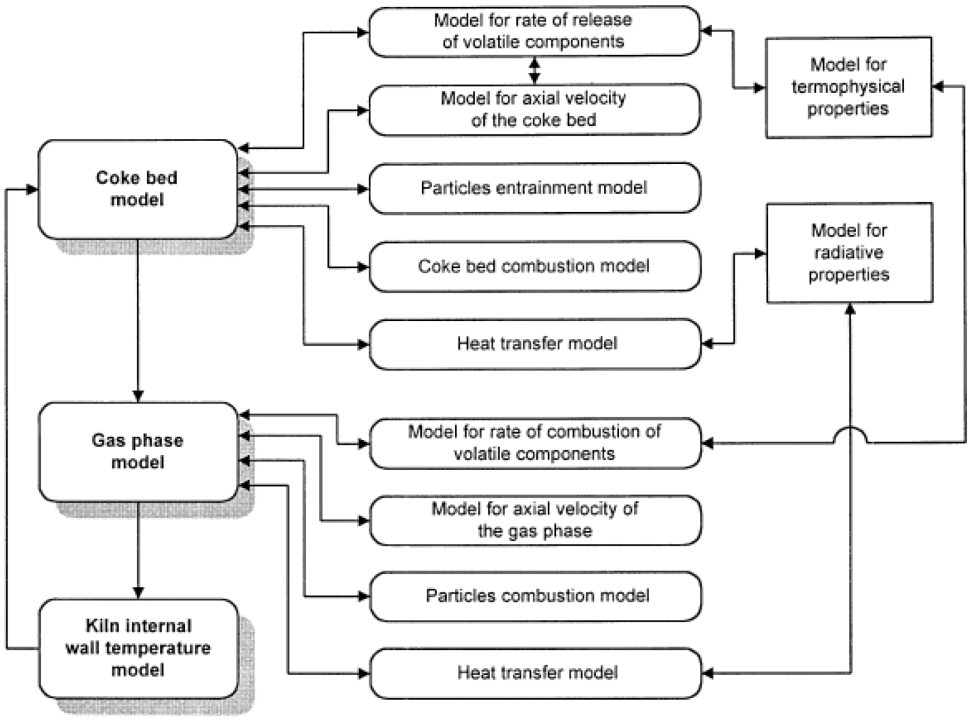

Figure 11. Information flow diagram of the coke calcination model (Martins et al., 2001).

A sensitivity analysis was also performed for the model to determine the optimal value for the increments in the axial direction (dx). The temperature profiles converged at a dx smaller than 0.75 m. The kiln is 60 m in length, hence the kiln has to be divided at least to 80 sections.

The system of non-linear equations for the temperature calculations is solved by the Picard iteration scheme coupled with a relaxation formula where the internal wall (w) and external wall (e) radiation are approximated by Equations 37 and 38, respectively,

$$T_w^4 = T_{w,n}(T_{w,n-1}^3) \qquad (37)$$

$$T_e^4 = T_{e,n}(T_{e,n-1}^3) \qquad (38)$$

resulting in a linearization procedure, since the values of the previous iterations (n-1) are known. In addition, convergence was improved by implementing relaxation Equations 39

$$T_n = \lambda T_n + (1 - \lambda) T_{n-1} \quad (39)$$

The relaxation parameters λ are reported to be different for the internal and the external wall temperatures.

4.1. Summary of the methods and assumptions implemented in the reviewed models

This chapter summarizes the main methods and assumptions used in the reviewed articles. The summary is divided to four sections; the first section includes the models for reaction kinetics. The second section comprises the mass transfer dynamics. The third section covers the heat exchange phenomenon considered in the models. The final and fourth section summarizes the assumptions about the physical properties.

4.1.1. Reaction kinetics

The reaction kinetics in the five introduced articles was mainly divided to two categories; drying of the free moisture and the chemical reactions. This division and the kinetic models used are shown in Table 2. Three different types of drying mechanisms are used in the models; a two-phase drying model is implemented in the case number 1, Arrhenius equation is used for drying in the cases 2 and 5, and the case 4 has a heat transfer dependent drying model. As for the chemical

reactions, all of the introduced cases use the Arrhenius equation. Additionally, in the case 4 the researchers themselves determined experimentally the parameters for the reaction kinetics.

Table 2. Reaction models implemented in the cases 1 to 5.

	Drying model	Reaction model
Case 1	Two-phase drying model	Arrhenius
Case 2	Arrhenius	Arrhenius
Case 3	N/A	N/A
Case 4	Heat transfer dependent	Arrhenius, self-measured
Case 5	Arrhenius	Arrhenius

4.1.2. Mass transfer

The mass transfer dynamics are commonly divided between the solid bed and the gas phase. Tables 3 and 4 list the main assumptions and models for the mass transfer applied in the presented cases. Each of the cases 1, 2, and 3 has different kinds of solid bed dynamics. However, in all of the five cases the gas phase is modelled with a steady-state model since the changes in the gas phase are fast. The water evaporated from the solids is only added into the gas phase in the case number 2. In other cases, the amount of evaporated water is assumed to be small compared to the amount of air. Molar component balances are calculated in each of the cases. The cases 2 and 3 include mixing models for the solid phase, but these models differ completely from each other. The only similarity between them is that they both assume no backward flow exists.

Table 3. Assumptions considering the mass transfer in cases 1 to 5 (1/2).

	Dynamics of the solid phase	Volumes in the solid phase	Dynamics of the gas phase	Volumes in the gas phase
Case 1	In = out, evaporation	1/hearth	Steady-state	1/hearth
Case 2	Polar coordinates and height of the bed	N/hearth	Steady-state	Not specified
Case 3	Inclination angle based	Several	N/A	N/A
Case 4	N/A	N/A	Steady-state	N/A
Case 5	N/A	N/A	Steady-state	N/A

Table 4. Assumptions considering the mass transfer in cases 1 to 5 (2/2).

	Evaporation to the gas phase	Component balances	Mixing path	Backward flow
Case 1	No	Yes	-	-
Case 2	Yes	Yes	Equal areas	No
Case 3	N/A	-	Isosceles-triangular cross-section	No
Case 4	N/A	Yes	N/A	N/A
Case 5	N/A	Yes	N/A	N/A

4.1.3. Heat transfer

The assumptions regarding the heat transfer and the heat transfer paths in the introduced cases are listed in Tables 5 and 6. The case 3 was not evaluated considering the heat exchange since differs from the case of MFH.

Each case includes the main heat transfer paths. The most noticeable difference, when comparing the different cases, is ignoring of the heat transfer by radiation in the case 1. Also the heat transfer between the gas phase and the walls and between the walls and the solid phase is neglected in case 1. However, only the case 1 considers the heat transfer with the central shaft and rabble arms.

Table 5. Assumptions considering the heat transfer in cases 1 to 5 (1/2).

	Heat transfer in the solid phase	**Gas-solid heat exchange**	**Walls – gas**	**Walls – solid**	**Solid – shaft**	**Gas – shaft**
Case 1	Convection	Convection	Equal T	Equal T	Yes	Yes
Case 2	Conduction	Convection, radiation	Convection, radiation	Conduction, radiation	No	No
Case 3	N/A	N/A	N/A	N/A	N/A	N/A
Case 4	Convection in axial direction	Convection, radiation, measured fixed value	Convection, radiation	Radiation	N/A	N/A
Case 5	Convection in axial direction	Convection, radiation	Convection, radiation	Radiation	N/A	N/A

The case 1 considers heat transfer through the floors and the others do not, as shown in Table 6. On the contrary, the case 1 does not have heat transfer in the walls whereas the others have. In each of the cases, the heat exchange with the environment is included in the model and the heat of reactions is considered in the energy balances.

Table 6. Assumptions considering the heat transfer in cases 1 to 5 (2/2).

	Heat exchange through floors	Heat transfer in the walls	Heat exchange to environment	Heat exchange to shaft and arms	Heat of reactions / evaporation
Case 1	Yes	No	Yes	Yes	Yes
Case 2	-	Yes	Convection, radiation	No	Yes
Case 3	N/A	N/A	N/A	N/A	N/A
Case 4	N/A	Conduction	Convection, radiation	N/A	Yes
Case 5	N/A	Conduction	Convection, radiation	N/A	Yes

4.1.4. Physical properties

The physical properties of materials, such as the gas components, the solid bed components and the furnace bricks, are divided to two categories; radiation properties and other physical properties. The assumptions applied in cases 1 to 5 are presented in Table 7.

The case number 1 is assuming physical properties, such as the heat capacities and the thermal conductivities to be constant. The case number 2 considers the materials dealing with radiation to be grey and transmitting. In addition, the bed

density and the thermal properties of bricks are assumed constant, whereas the heat capacity of the coke is considered to be temperature dependent. In the case 3 the angle of repose of the bed material is assumed to be constant. Finally, in the case 4 the radiative surfaces are assumed grey and the bed porosity is considered to be constant.

Table 7. Assumptions considering the radiation and physical properties in cases 1 to 5.

	Radiation properties		**Physical properties**	
	Gas	**Surfaces**	**Constant parameters**	**T dependent**
Case 1	-	-	c_p, k	-
Case 2	Grey, transmitting, non-reflecting	Grey	Bed density, brick thermal properties	$c_{p,coke}$
Case 3	N/A	N/A	Angle of repose	-
Case 4	-	Grey	Porosity	-
Case 5	-	-	-	-

EXPERIMENTAL PART

5. Aim of the experimental part

The main aim of the experimental part is to develop a dynamic model of the multiple hearth furnace at Lee Moor. The model is built to study the temperature profile of the solid bed and the gas phase and the chemical reactions occurring inside the furnace. In addition, changes in the feed and different process conditions can be simulated and their effect on the process operation evaluated. The model consists of a dynamic solid bed model and of a steady-state gas phase model.

To support the model development, the solid bed dynamics are studied using a pilot scale MHF, which is a 1:12 ratio model of the Lee Moor MHF. The pilot is used to provide information of the mass distribution between the hearths and the residence time distribution of the furnace. Based on these experiments a model describing the solid flow movements is developed.

Finally, the mathematical model of the MHF is implemented in the MATLAB environment and a graphical user interface (GUI) is built for the simulator. Simulation studies are performed and the results are presented and analysed.

6. Process description of the Lee Moor calcination plant

The multiple hearth furnace modelled in this Master's Thesis is located at the Lee Moor calcination plant. There are four main units in the Lee Moor calcination process: the Altenburger mill, the feeding system of the calciner, the Herreschoff multiple hearth furnace and the Bauer mills. The process flow sheet can be divided to a solid flow line and a gas flow line, which are described next (Hearle, 2012).

6.1. The solid flow line

At first, kaolin clay is delivered by trucks to the plant and the material tipped into the in-feed hopper. Next, the kaolin is conveyed to a 350 ton Redlar bin using a bucket elevator. From the Redlar bin the kaolin feed is conveyed by another bucket elevator to the Altenburger mill feed bin. From the mill feed bin the kaolin containing 10 weight-percent of moisture is fed into the Altenburger mill-dryer. The Altenburger mill removes the water and provides powder as a feed to the calciner. The material leaving the Altenburger is collected in a bag filter and is afterwards transferred to the powder feed silo by a lean phase air conveyor (LPC) through a rotary blow seal. The powder held in the silo is transferred by another LPC to the calciner upper weigh feeder bin at the top of the kiln.

The powder is transferred from the upper bin to the weighed hopper via a rotary valve. The rotary valve can deliver weights from 0 to 145 kilograms per minute. When the desired weight of the feed in the weigh hopper has been achieved, the powder is transferred to the lower bin via two slide valves. This action cycles once per minute hence the feed rate is expressed in kg/minute of a zero moisture feed. A screw conveyor is used to transfer the material from the lower bin to the furnace. The amount of material in the lower bin is controlled by a level probe that controls the screw speed preventing a complete discharge of the powder to stop the escape

of exhaust gases from the calciner through the feeder system. The multiple hearth furnace is described in its own chapter below.

The calcined kaolin leaves the calciner through two discharge holes located at the bottom hearth and then via water cooled screws into a high flow stream of ambient air. After the screws the product is at a temperature of around 750°C and is further cooled by the air blast coolers such that the temperature of air and product is around 100°C by the time it reaches the air blast cooler bag filters. The material is collected at the bottom of the bag filter hopper from where it is conveyed by LPC via a blowing seal to the Bauer mills feed bin.

The calciner feed has a very fine particle size with a mean size of around 3 µm. However, during calcination some of these particles are stuck together to form aggregates with a mean size around 15 microns. Aggregates that enter the calciner are fused together and other smaller particles tend to aggregate at high temperatures.

The Bauer mill-classifiers are high speed air swept mills used to reduce the particle size of the aggregates and to remove material greater than 50 microns as rejects and producing a mean particle size around 5 microns. As the air flow passes through the classifiers, the large particles are concentrated at the outside edge and leave the classifier through a flap valve. The flap opens when the weight of rejects exceeds the suction pressure on the flap and the rejects fall out. From the Bauer mills the air and the classified product continue their way to the bag filter where the product is separated from the air. The product is collected in the bag filter hopper from where it passes into another LPC for transportation either to the small bag packer or IBC packer.

6.2. The multiple hearth furnace

The multiple hearth furnace at Lee Moor has eight hearths. The furnace is constructed of bricks and enclosed by a cylindrical steel shell with refractory lining. The material flow through the furnace is stirred and moved spirally across the hearths by a centrally oriented vertical rotating shaft carrying arms with rabble blades. Material is fed to the top hearth through a single inlet from the weigh feed hopper to the periphery of the hearth. The material on the odd numbered hearths is stirred by the rabble blades towards the centre of the hearth and the material drops down to the next hearth from the centre through a single annulus around the shaft supporting the rabble arms. Material on the even numbered hearths is moved outwards to be dropped through drop holes at the periphery of the hearth. The stirring pattern is repeated until the lowest heart is reached from which the calcined product is extracted through the two exit holes. The product falls from the exit holes to screw conveyors. Figure 12 presents a cross-sectional picture of the Herreschoff furnace.

Heat required by the calcination is supplied to the furnace through burners on the hearths 4 and 6. Each hearth has four tangentially aligned burners. In the hearths 1, 2 and 3 the temperature of kaolin rises progressively to about 700 °C. The temperature of the material continues to rise in the hearths 4, 5 and 6. The temperature control of the hearth 6 is the most critical objective of the process to prevent overheating the product. In the hearths 7 and 8 the product starts to cool and as it leaves the furnace from the hearth 8 its temperature is around 750 °C.

The burners can be operated by using either natural gas or fuel oil. The temperature in the 'fired hearths' is controlled by varying the gas flow. The amount of combustion air is a function of the gas flow. The gas and air flows are measured using orifice plate flow meters. The gas flow on the hearth 4 is a function of the feed rate to prevent the excessive use of the gas. The oil flow is measured using geared flow meters. The oil requires a fixed volume of air to produce an atomized spray to improve combustion. This air is supplied from the high pressure fans. The

air flow for the oil burners can be operated at two levels; low flow, to prevent the overheating of the oil lines to the burners when operating on gas, and high flow, while using oil as fuel. At the moment only natural gas is used in the daily operation.

The pressure in the furnace is measured by two sensors in the main calciner exhaust duct. The calciner is operated slightly under pressure by the main exhaust fan, which is at the end of the exhaust gas process discharging the exhaust gases through the main stack. The pressure in the furnace is a function of the fan speed. The pressure sensors are fitted with an air purge cleaning system.

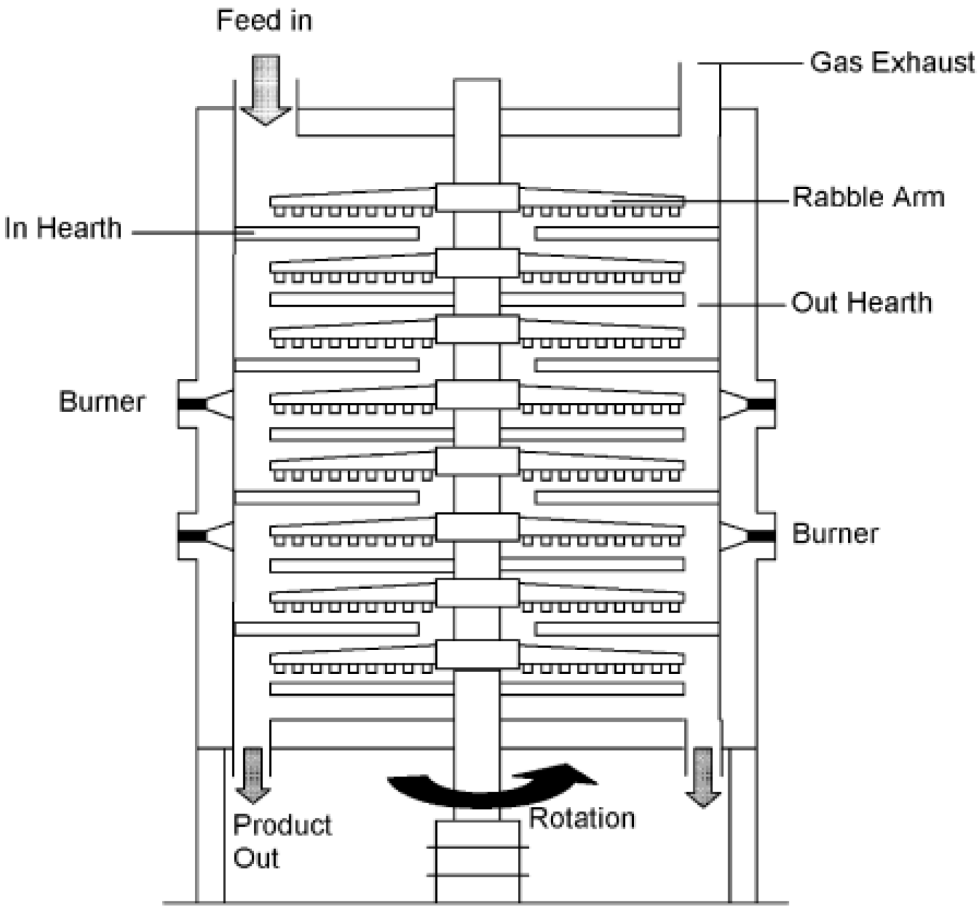

Figure 12. Cross-sectional picture of a Herreschoff furnace with direct fire burners.

6.3. The gas flow line

The exhaust gases leaving the furnace are lead through an American Air Filter (AAF) heat exchange system in a normal operation, but in a case of emergency there exists a possibility to vent the exhaust gases to atmosphere by operation of the stack vent valve. The AAF plant consists of a heat exchanger and a bag filter.

The heat exchanger is used to recover heat to supply the calciner feed drying process and for cooling the exhaust gases to prevent damage to the bag filters, which remove previously entrained product. Operation of the heat exchanger is automatic and faults or process extremes activate alarms. The hot process air coming from the heat exchanger passes into the inlet of the Altenburger mill where it passes through the mill and the hot air is used to dry the feed clay. Ambient air is used on the 'cold' side of the heat exchanger. The temperature of the exhaust gases entering the heat exchanger must be under 650 °C to prevent any damage for the heat exchanger material. If the exhaust gas temperature is too high, it can be cooled by combining ambient air from outside the building with the exhaust gases.

The heat exchanger control is associated with three algorithms. The primary algorithm controls the temperature of the air passing into the bag filter, by varying the speed of the process air fan which introduces ambient air the process. The second algorithm controls the temperature of the process air leaving the heat exchanger by varying the amount of hot air allowed to be recycled. The third algorithm controls the pressure in the process air duct to the Altenburger mill by regulating the position of the process air vent damper.

The cooled exhaust gases pass into the bag filter to remove the entrained product. The product is collected in the hopper below the bag filters and is screwed into an LPC via a rotary blowing seal which discharges into the Altenburger milled product silo.

After the bag filter, the de-dusted exhaust gases continue into a Peabody water scrubber which removes fluorine from the gas. The effluent from the Peabody

scrubber is treated with sodium carbonate to neutralize the fluorine as hydrofluoric acid before discharging through the environmental authority discharge consent point. The temperature of the exhaust gas before the Peabody scrubber must stay above $150^{O}C$ to prevent the condensation of fluorine as hydrofluoric acid (HF) and its subsequent detrimental effects on ducting. After exiting the Peabody water scrubber, the gases flow to the exhaust stack via the exhaust fan.

7. Mathematical modelling of the MHF

In this modelling work, the MHF is divided to five sections; a solid bed, a gas phase, walls, a central shaft and rabble arms. The mathematical model of the furnace includes reaction kinetics, mass transfer and heat transfer mechanisms for each four section. In addition, equations for calculating temperature dependent parameters, such as gas heat capacities, gas emissivities and the solid bed emissivities, are implemented. Figure 13 illustrates the structure of the MHF model.

This chapter describes all the models and mechanisms implemented in the MFH simulator. However, first the assumptions required to build such a model are presented in section 7.1.

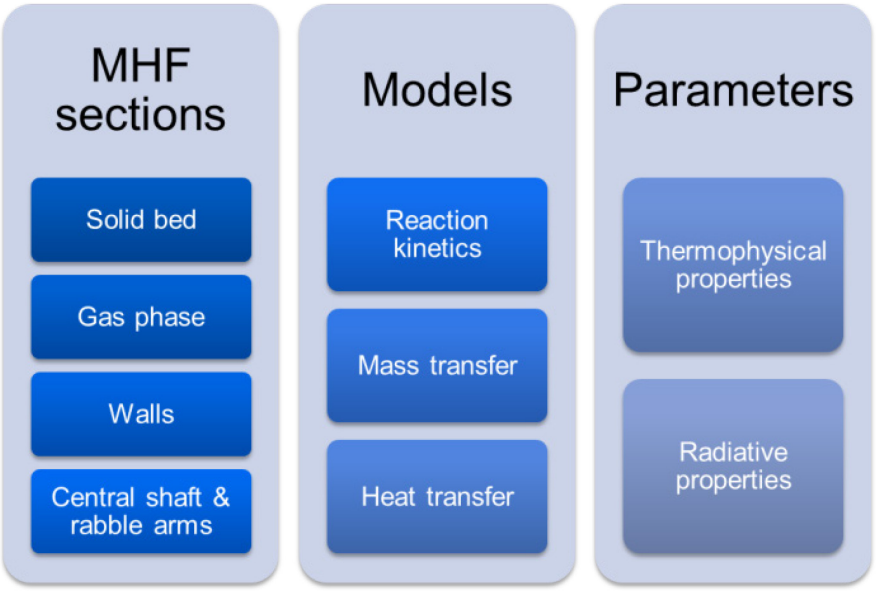

Figure 13. Concept of the structure of the mathematical model of the MHF.

7.1. The main assumptions

To construct a dynamic process model a few specific assumptions have to be considered for simplification. The assumptions for the MHF model are listed below.

1. The solid bed on each hearth is split into 4 or 5 homogenous annular sections according to the furnace characteristics. The sections equal in volume and in width in a radial direction. There is a proportion of each volume that is moved to the previous volume or to the next volume or stays in the same volume after one full central shaft rotation.
2. No heat conduction occurs inside the bed. The bed sections are assumed homogenous in temperature and composition.
3. Four reactions occur in the bed:
   3.1. Water evaporation
   3.2. Dehydroxylation and formation of metakaolin
   3.3. Spinel phase formation
   3.4. Nucleation of spinel phase and transformation to mullite

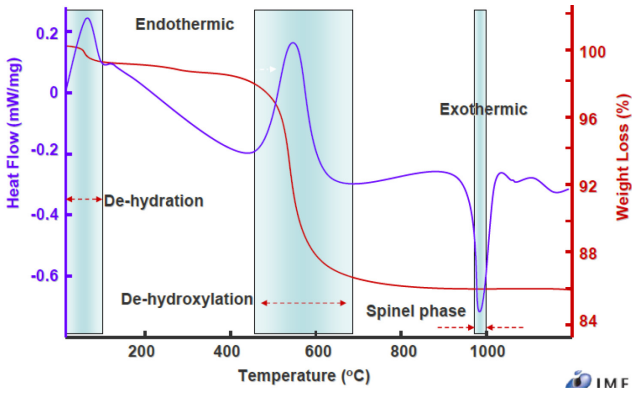

4. The gas phase is ideal.
5. The gas phase has five components: methane, oxygen, nitrogen, water and carbon dioxide
6. The gas phase on a specific hearth is divided into 4 of 5 homogenous annular volumes according to the corresponding number of solid volumes in the hearth.
7. The burning of methane is not perfect at the burner volume and a portion of the methane is burnt at the following volumes.
8. Heat exchange occurs between solid and gas, solid and wall, gas and wall, wall and environment, and gas and arms. Also, heat exchange exists between cooling air and central shaft and rabble arms.

9. The furnace wall is divided to 8 sections according to hearths, so that each section has a fixed temperature and there is no vertical heat exchange in the wall.
10. The central shaft is divided to 8 eight sections according to hearths, so that each section has a fixed temperature and there is no vertical heat exchange in the shaft.
11. Emissivity of the gas phase is a function of water and carbon dioxide content and heat capacities of the gas phase components are a function of temperature.
12. Emissivity of the solid bed is a function of temperature.
13. Density of the kaolin is assumed constant.

7.2. Reaction kinetics

The main reactions considered in the bed are drying of free moisture, dehydroxylation, spinel phase formation and mullite formation (Equations 1-4, Assumption 3). For each reaction, the reaction rate coefficient k is modelled using the Arrhenius equation, Equation 40,

$$k = Ae^{-\frac{E_A}{RT}} \qquad (40)$$

where A is the frequency factor of the reaction, E_A is the corresponding activation energy, T denotes the current absolute temperature and R is the gas constant. The reaction rate (R) equation for each reacting component follows Equation 41

$$R_i = k_i C_i \qquad (41)$$

where C is the concentration of the reacting component.

7.2.1. Drying

Evaporation of the free water from kaolin follows Equation 42. Table 8 summarizes the parameters for evaporation found in the literature.

$$H_2O(l) \rightarrow H_2O(g) \qquad (42)$$

Table 8. The Arrhenius parameters for water evaporation found in literature.

Ea (kJ/mol)	**A (s^{-1})**	**Reference**
71.942	2.549*10^7	(Martins et al., 2001)
41.942	19667	(Meisingset & Balchen, 1995)

In the model, the reaction rate coefficient for drying is calculated with Equation 43

$$k_{drying} = 5 * 10^7 \frac{1}{s} e^{-\frac{61000\frac{J}{mol}}{RT}} \qquad (43)$$

and the reaction rate is implemented as in Equation 44

$$R_{drying} = k_{drying} C_{water} \qquad (44)$$

Due to the deviation in the literature values, the reaction parameters were fitted to match the TG and DSC curves of kaolin (Figure 14). The fitted reaction curve is shown in Figure 15. The values of 61 kJ/mol and $5*10^7$ s^{-1} in Equation 43 are obtained as the results of fitting. The heat of vaporization for water is 2258.22 kJ/kg (CRC Handbook, 2005).

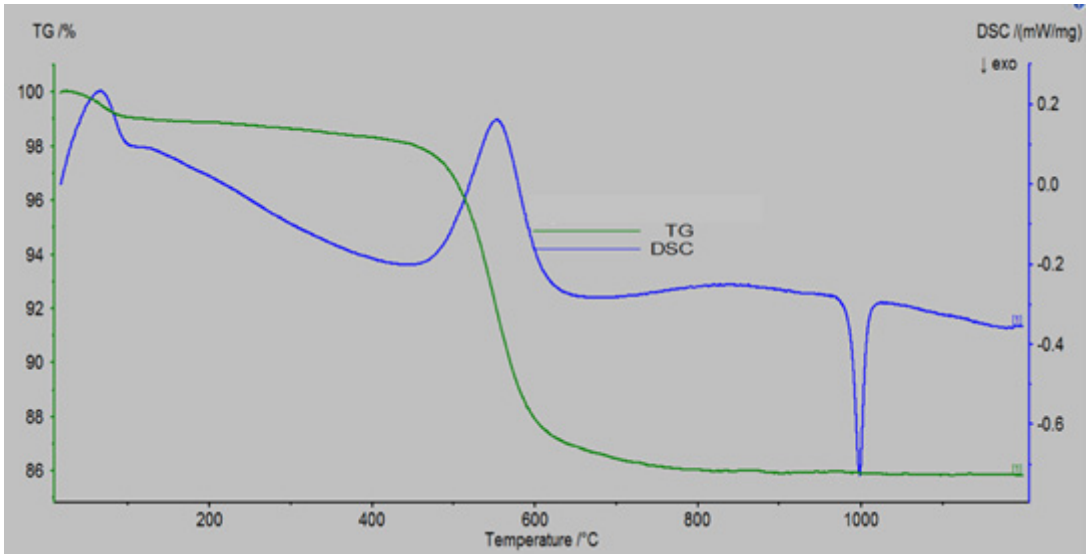

Figure 14. TG and DSC curves of kaolin calcination (Imerys).

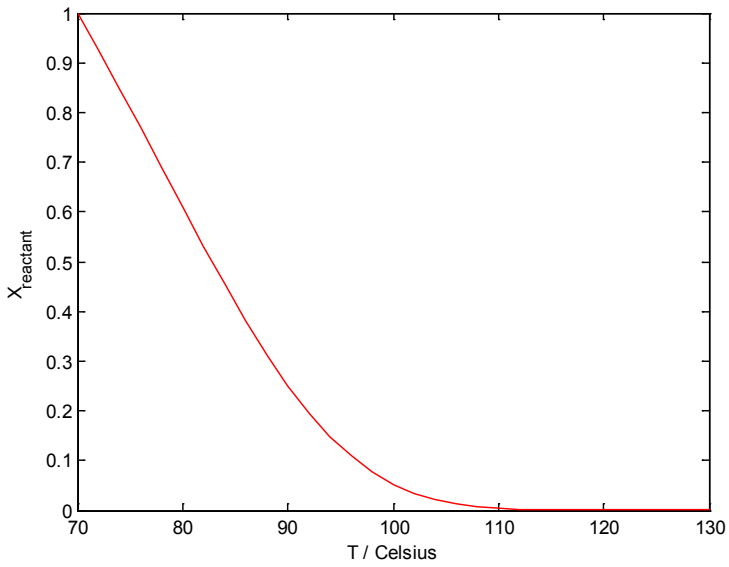

Figure 15. Reaction curve shows the evaporation of free moisture. The heating rate used to calculate the reaction curve was 40 °C/min.

7.2.2. Dehydroxylation

Dehydroxylation of kaolin and formation to metakaolin is assumed to occur in the temperature range of 450-700 °C according to Equation 45

$$Al_2O_3 \cdot 2SiO_2 \cdot 2H_2O \rightarrow Al_2O_3 \cdot 2SiO_2 + 2H_2O(g) \qquad (45)$$

Table 9 summarizes the parameters for the dehydroxylation reaction found in literature. From the table it can be seen that the activation energy E_a varies between 76.6 and 257 kJ/mol and the frequency factor A varies between 0.12 and 1.9*10^19. The large variations in parameters are partly explained by how well the kaolin is ordered. Whether it is relatively disordered, medium ordered or well ordered. According to several sources (Ptacek et al., 2010), (Ptacek et al., 2010), and

(Ptacek et al., 2010)), the dehydroxylation reaction is a third order reaction. Figure 16 illustrates the difference between the frequency factors of dehydroxylation reported in literature.

Table 9. Activation energies, frequency factors, reaction enthalpies, valid temperature ranges and notes for kaolin dehydroxylation reactions found from literature.

E_a (kJ/mol)	A (s^{-1})	ΔH (kJ/mol)	T_{range} (C)	Reference	Notes
76.6 - 216.17	0.12 – 9.26 *10^4	-	-	(Ptacek et al., 2013)	Relatively disordered – ordered kaolin
257	1.9*10^{19}	-	370-410	(Ptacek et al., 2010)	Isothermal experiments, medium ordered, second order kinetics
202	2.9*10^{15}	-	415-500	(Ptacek et al., 2010)	Isothermal experiments, medium ordered, third order kinetics
242	2.21*10^8	-	370-540	(Ptacek et al., 2010)	Medium ordered, non-isothermal conditions, third order reaction
167.5 / 108.9	6.33*10^6 /8.33*10^3	-	-	(Bellotto et al., 1995)	Ordered/disordered, First order kinetics
157.4 – 154.5	1.7*10^{10} – 1.0*10^9	-	369	(Criado et al., 1984)	Conversion dependence, isothermal experiments
195	8.58*10^{14}	-	-	(Ptacek et al., 2011)	Medium oriented, non-isothermal, list of literature values
226	9.4*10^9	-	-	(Ptacek et al., 2010)	Medium oriented, non-isothermal, third-order reaction
239	8.55*10^7	-	-	(Ptacek et al., 2010)	
-	-	230	-	(Petzold et al., 1985)	

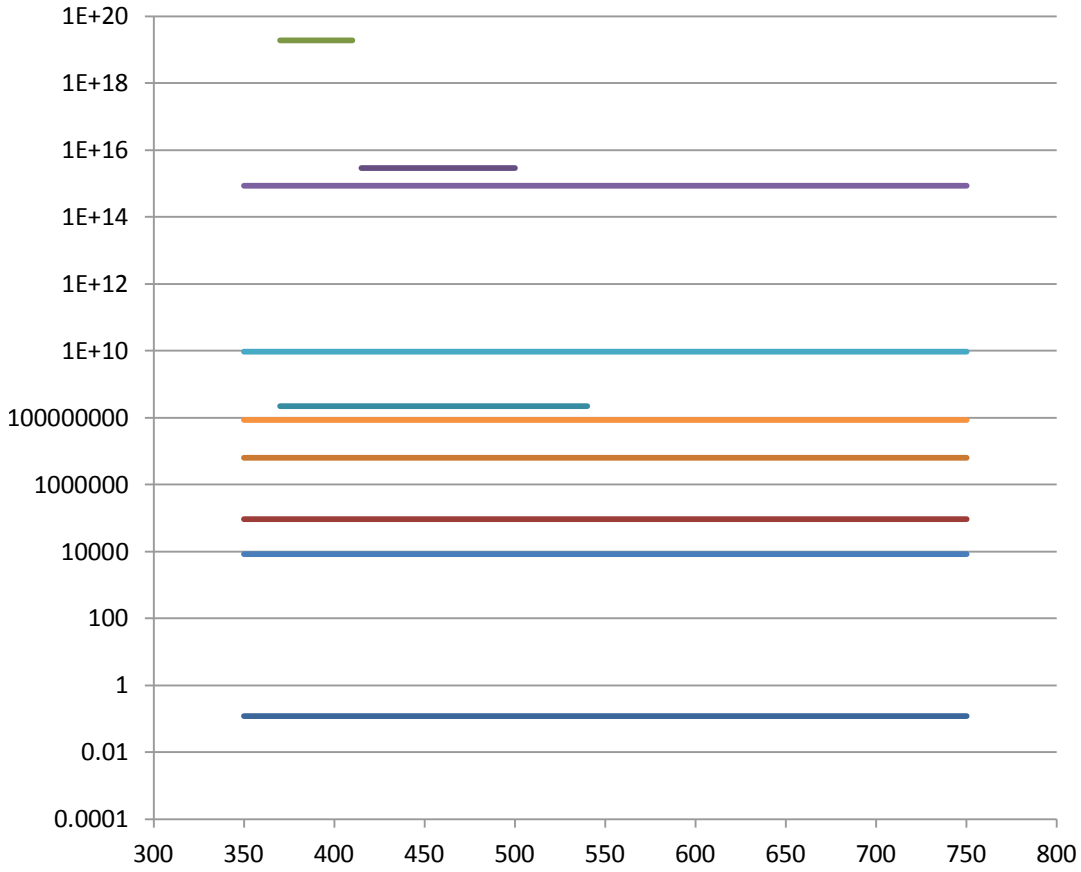

Figure 16. The deviation of the frequency factors of hydroxylation of kaolin found from literature.

In the model, the reaction rate coefficient is calculated with Equation 46

$$k_{dehydroxylation} = 1 * 10^7 * e^{-\frac{145000\frac{J}{mol}}{RT}}, \quad (46)$$

and the reaction rate is implemented as in Equation 47

$$R_{dehydroxylation} = k_{dehydroxylation} C_{kaolin} \quad (47)$$

The values of 145 kJ/mol and $1*10^7$ s^{-1} in Equation 46 are obtained by fitting the reaction rate curve to match the TG and DSC curves of kaolin. The reaction curve is shown in Figure 17. The fitted values are in line with the values found from the literature. The reaction enthalpy for dehydroxylation in the model is 230 kJ/mol.

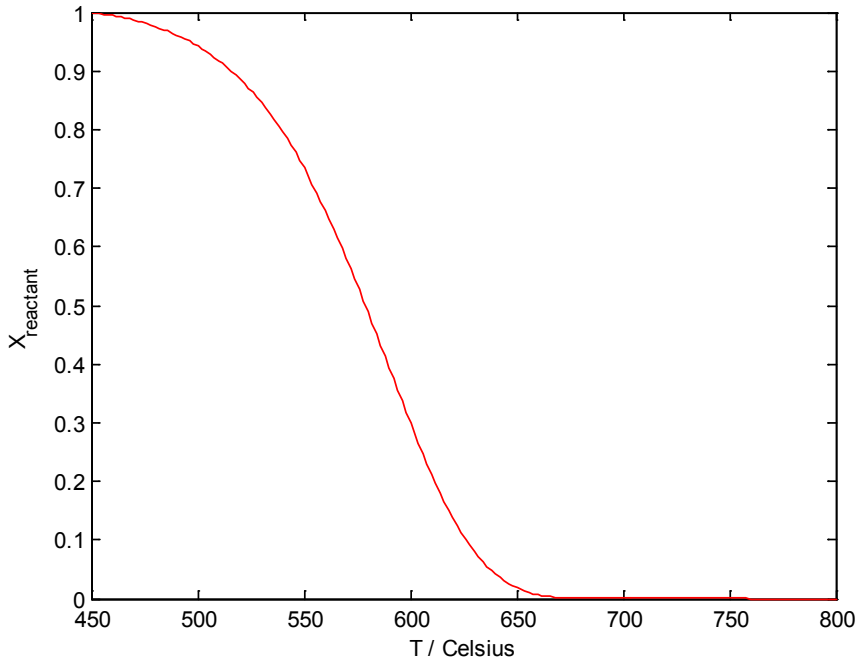

Figure 17. Reaction curve presenting the consumption of kaolin during dehydroxylation. The heating rate used to calculate the reaction curve was 40 °C/min.

7.2.3. Spinel formation

The formation of the spinel phase, Equation 48, is assumed to occur at around 980 °C in the temperature range from 925 up to 1050 °C.

$$2(Al_2O_3 \cdot 2SiO_2) \rightarrow 2Al_2O_3 \cdot 3SiO_2 + SiO_2(amorphous), \qquad (48)$$

Table 10 lists the parameters for the spinel formation found in the literature.

Table 10. Kinetic data of the spinel formation reaction.

Ea (kJ/mol)	A (s^{-1})	ΔH (kJ/mol)	Reference	Notes
856	-	-	(Ptacek et al., 2010)	Medium ordered kaolin
		-40.18	(Mazumdar & Mukherjee, 1983)	Experimentally obtained
		-54.39	(Mazumdar & Mukherjee, 1983)	Theoretical value

In the model, the reaction rate coefficient is calculated with Equation 49

$$k_{spinel} = 5 * 10^{33} * e^{-\frac{856000\frac{J}{mol}}{RT}}, \quad (49)$$

and the reaction rate is implemented as in Equation 50

$$R_{spinel} = k_{spinel} C_{metakaolin} \quad (50)$$

The value of $5*10^{33}$ s^{-1} for the frequency factor is obtained by fitting the reaction rate curve to match the TG and DSC curves of kaolin. The reaction curve is shown in Figure 18. An average value of -47.29 kJ/mol is used for the reaction enthalpy.

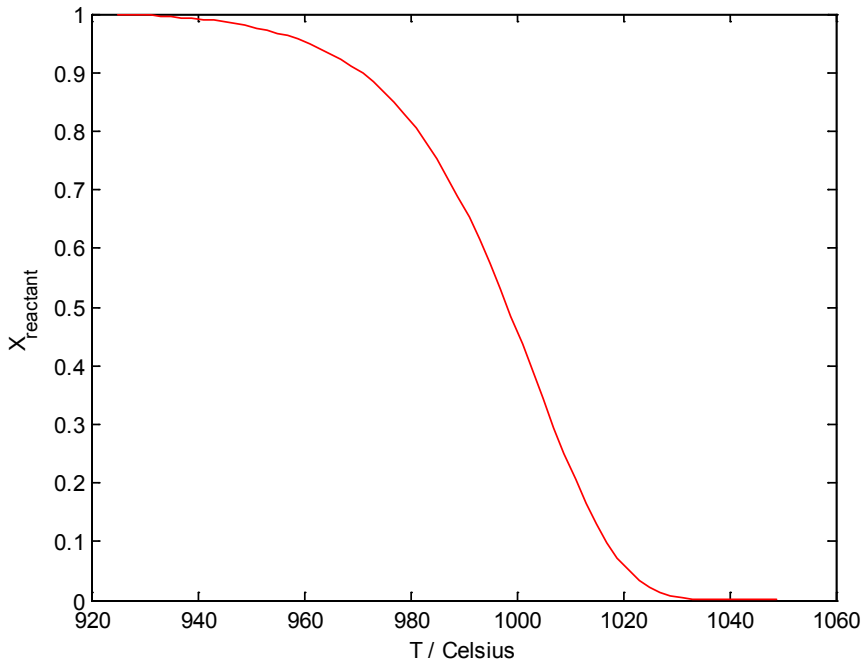

Figure 18. Reaction curve shows the consumption of metakaolin in the spinel formation reaction. The heating rate used to calculate the reaction curve was 40 °C/min.

7.2.4. Mullite Formation

The nucleation of the spinel phase and transformation to mullite (Equation 51) is assumed to occur at temperature higher than 1050 °C. The kinetic parameters and the heat of reaction found in the literature for the crystal structure change are given in Table 11.

$$3(2Al_2O_3 \cdot 3SiO_2) \rightarrow 2(3Al_2O_3 \cdot 2SiO_2) + 5SiO_2, \qquad (51)$$

Table 11. Kinetic data of the mullite formation reaction.

Ea (kJ/mol)	A (s^{-1})	ΔH (kJ/mol)	Reference	Notes
512.5	$1.71*10^{19}$	500.1	(Ptacek et al., 2012)	At heating rate 10 C /min
360.0	$1.833*10^{13}$		(Gualtieri et al., 1995)	Ordered
523.4	$2.833*10^{8}$		(Gualtieri et al., 1995)	Disordered

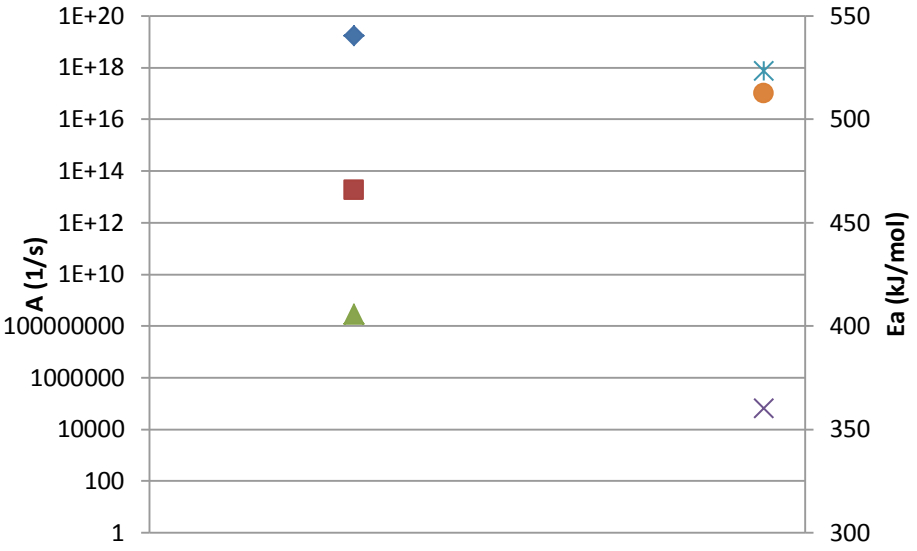

Figure 19. Frequency factors and activation energies of the mullite formation found in the literature. Frequency factors on the left hand side and activation energies on the right hand side.

As it can be seen from Table 11 and Figure 19, the reaction parameters in the literature differ. Therefore, the reaction parameters have to be adjusted to obtain the reaction parameters for the model. In the model, the reaction rate coefficient is calculated with Equation 52

$$k_{mullite} = 1 * 10^{17} * e^{-\frac{522000\frac{J}{mol}}{RT}} \quad (52)$$

and the reaction rate is implemented as in Equation 53

$$R_{mullite} = k_{mullite} C_{spinel} \quad (53)$$

The values of 522 kJ/mol and $1*10^{17}$ s^{-1} in Equation 52 are obtained by fitting the reaction rate curve to match the TG and DSC curves of kaolin. The reaction curve is shown in Figure 20. The fitted values are in line with the values found from the literature. The used value for the reaction enthalpy is 500.1 kJ/mol.

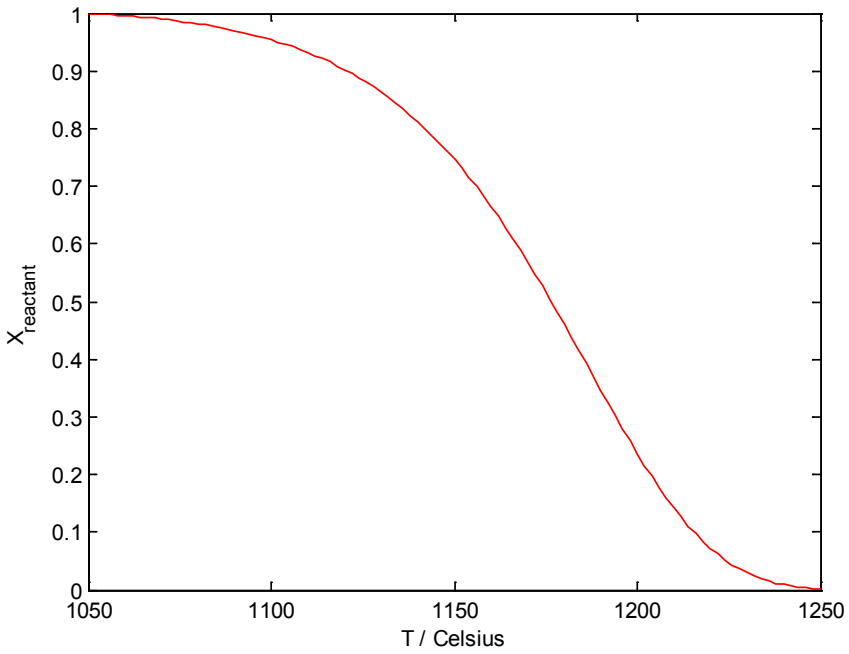

Figure 20. The reaction curve of the mullite formation presenting the consumption of spinel phase. The heating rate used to calculate the reaction curve was 40 °C/min.

7.2.5. Combustion of methane

The burners on the hearths 4 and 6 provide energy for the calcination process by combusting methane. The combustion reaction of methane is following

$$CH_4(g) + 2O_2(g) \rightarrow CO_2(g) + 2H_2O(g) \quad (54)$$

The amount of combustion energy from the reaction is the lower burning value of 802 kJ/mol (CRC Handbook, 2005). According to Assumption 7 the burning of methane is not perfect at the gas volume where the burners are located and thus a portion of the methane is burnt at the following volumes. The portions are described using the combustion parameters *a* and *b*, which are model parameters used in simulation. Table 12 shows how the combustion parameters are implemented in each volume through the hearths 4 and 6 where all of the methane is assumed to be combusted. Since each gas volume is assumed uniform in composition and temperature (discussed in the subchapter 7.3.2), the burning of methane is not modelled using reaction kinetics.

Table 12. Methane combustion ratios.

		Volume number			
		1	**2**	**3**	**4**
Hearth number	**4**	$(1 - b)^3$	$b*(1-b)^2$	b*(1-b)	b
	5	$a*(1 - a)^4$	$(1-a)^5$	0	0
	6	$a*(1 - a)^3$	$a*(1-a)^2$	a*(1-a)	a

7.3. Mass transfer in the MHF

Mass transfer is divided into two sections; the solid bed dynamics and the gas phase dynamics. Mass transfer occurs in the solid bed as the solid bed is mixed and moved by the rabble blades, the solids fall to the next hearth and when water is evaporated to the gas phase. For the gas phase, mass transfer occurs when the gas moves to the upper hearths and when water is evaporated from the solids. The mass transfer dynamics for the both sections are described in this subchapter.

7.3.1. Solid bed dynamics

The general mass continuity equation for the solid phase is

$$\frac{\partial m}{\partial t} = m_{in} - m_{out} - R_r \qquad (55)$$

where m_{in} presents the total incoming mass flow into the furnace, m_{out} is the total outgoing mass flow from the furnace and R_r presents the mass transferred to the gas phase through the drying and dehydroxylation reaction as presented before. There is known to be a mass loss of the material from 300 to 400 kg per hour to the flue gases due to high flow rate of the gas and turbulence. However, it is not considered in this model.

The mass continuity equation for an individual hearth is the same as Equation 55, with the exception that the m_{in} presents the incoming mass flow from the previous upper volume and m_{out} is the outgoing mass flow dropped to the next volume on the lower hearth. Equation 56 presents the exchange of matter from the upper hearth to the lower hearth

$$N_{solid,in}^{i} = N_{solid,out}^{i-1}, \quad (56)$$

where N denotes mass, amount of substance or temperature of a given hearth i, moved to the next hearth.

Furthermore, as Assumption 1 states, the solid bed on each hearth is divided to four or five annular uniform compartments according to the furnace characteristics as shown in Figure 21. The hearths 1 and 2 are divided to five compartments and the hearts 3 to 8 are divided to four compartments. The mass balance of these compartments follow the general mass balance equation (55), where m_{in} is the incoming mass from the neighbour compartments and m_{out} presents the mass transferred to the neighbour compartments.

In addition, Equations 57 and 58 present the exchange of matter on 'out-hearth' where material is moved from the centre towards the edges and on 'in-hearth' where material is moved from the periphery towards the centre, respectively:

$$N_{solid}^{i,out} = N_{solid}^{i+1,in}, \quad (57)$$

$$N_{solid}^{i,out} = N_{solid}^{i-1,in}, \quad (58)$$

where N denotes mass, amount of substance or temperature of a given compartment i, moved to the following compartment.

The density of kaolin is assumed constant (Assumption 13) and the compartments are assumed to have equal volume, which causes the height of the annular heaps to grow towards the centre as shown in the cross sectional Figure 21. The annular rings have a triangular cross-section where the angle between the horizontal

bottom and one side of the heap equals the angle of repose that is a characteristic property of material.

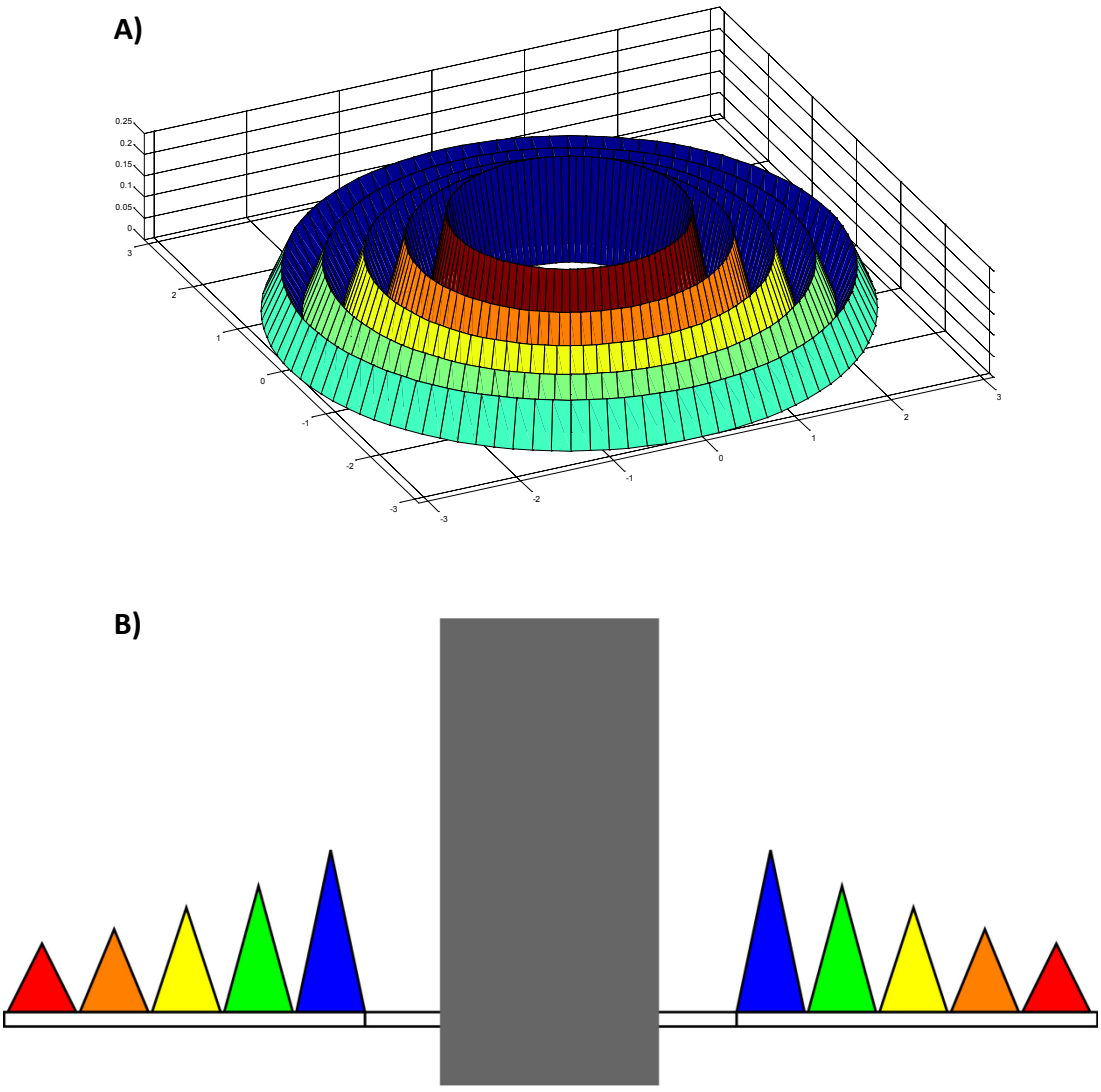

Figure 21. A) View of a solid bed with 5 annular compartments. B) Cross sectional view of the solid bed.

The mass transportation between compartments on the same hearth can take place via three possible paths:

1) Proportion of the kaolin stays in the current compartment
2) Proportion of the kaolin is moved to the next compartment
3) Proportion of the kaolin is moved backwards to the previous compartment

The black arrows in Figure 22 present these three paths. The proportions of kaolin moved along each possible path is determined by the experimental tests which are described in Chapter 8.

Figure 22. Movement paths of kaolin from one compartment to other compartments during one full rotation of the central shaft (inward rabble).

7.3.2. Gas phase dynamics

The gas phase is assumed ideal (Assumption 4) and it consists of five components; oxygen, nitrogen, methane, water and carbon dioxide (Assumption 5). The gas phase on a specific hearth is divided into 4 of 5 homogenous annular volumes according to the corresponding number of solid volumes in the hearth (Assumption 6). Due to the turbulence in the gas flow and a relatively fast flow rate of the gas phase (see chapter 7.4.5) the individual gas phase volumes are assumed to be

uniform regarding composition and temperature and they are modelled with a steady-state model. The scene of furnace's gas volumes is presented in Figure 23.

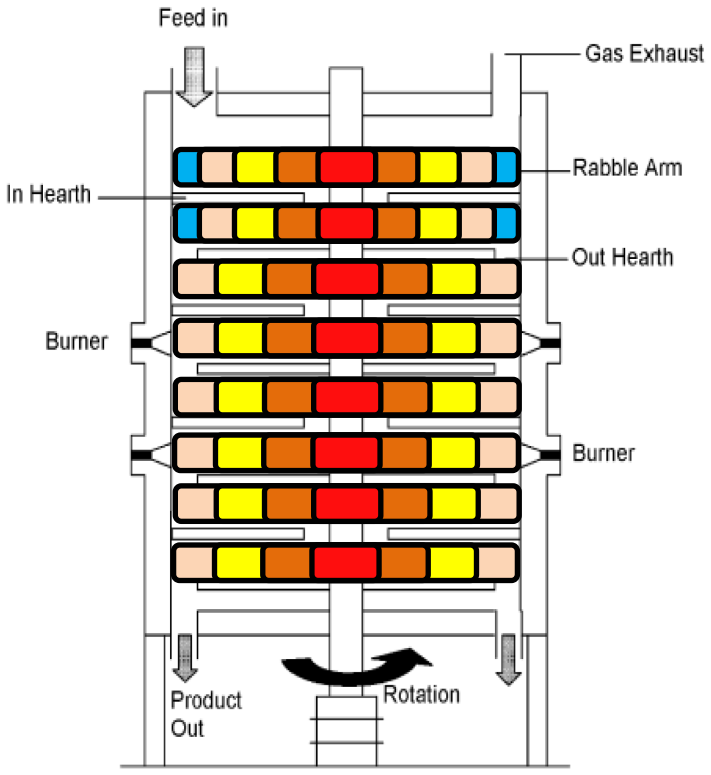

Figure 23. The gas division on each hearth.

The gas phase mass balance equation is derived for each primary gas component; oxygen, nitrogen, methane, water and carbon dioxide

$$n_{i,in} - n_{i,out} - R_i = 0 \qquad (59)$$

where subscript i denotes the component, $n_{i,in}$ is the molar amount of the component i entering the volume, $n_{i,out}$ is the molar amount of the component i leaving the volume and R_i is the reaction rate of the gas component i.

$n_{i,in}$ is obtained from Equation 60

$$n_{i,in} = c_i^{j+1} F, \tag{60}$$

where c_i^{j+1} is the concentration of the component i in the lower hearth (j+1) and F denotes the total gas flow (m^3). The total gas flow can be calculated from the ideal gas law (Assumption 4). The furnace is operated close to the atmospheric pressure slightly under pressured. For modelling purposes, atmospheric pressure is assumed throughout the furnace. The total gas flow on the hearths 7 and 8 equals to the draft through the drop holes at the bottom hearth due to the under pressure in the furnace, however the amount of the draft is assumed to be negligible in the terms of heat exchange and the gas phase on the hearths 7 and 8 is assumed stationary when considering the heat exchange. The total gas flow on the hearths 5 and 6 equals to the sum of methane and combustion air fed to the hearth 6, the gases from different reactions and the air flow from the lower hearths. At the hearths 1 to 4 the total gas flow consists of the gas flow from the hearth 5, the methane and combustion air fed to the hearth 4 and the gases from the different reactions. Now, the real gas flow, F_{real}, on each hearth having different temperature can be calculated as

$$F_{real} = F_{NTP} \frac{T_{real}}{T_{NTP}} \tag{61}$$

7.4. Energy conservation equations in the MHF

The heat transfer paths in the multiple hearth furnace are shown in Figure 24. In total, there are seven different heat transfer paths as listed in Assumption 8;

1. Heat transfer between the solid bed and the gas phase by radiation and convection
2. Heat transfer between the wall and the solid bed by radiation
3. Heat transfer between the wall and the gas phase by radiation and convection
4. Heat transfer inside the wall by conduction
5. Heat transfer between the outer wall and the ambitious air by convection
6. Heat transfer between the gas phase and the central shaft and the rabble arms
7. Heat transfer between the cooling air and the central shaft and the rabble arms

In addition, it was assumed that there exists no conduction inside the solid bed (Assumption 2).

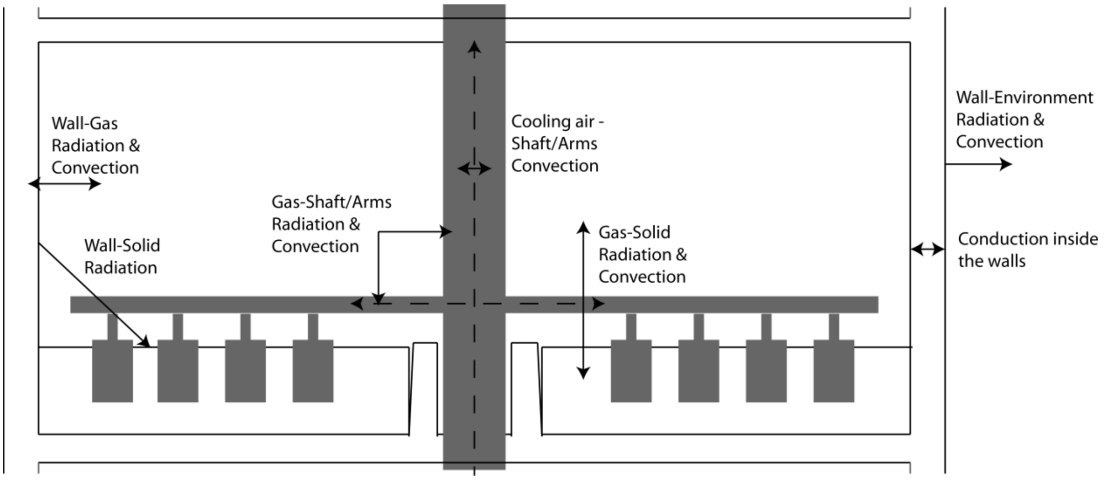

Figure 24. The heat transfer paths considered in the MHF model.

7.4.1. Solid phase energy balance

The general solid phase energy continuity equation is

$$\frac{\partial Q}{\partial t} = \dot{Q}_{mass,in} - \dot{Q}_{mass,out} - \dot{Q}_{reactions} - \dot{Q}_{evaporation} + Q_{sw} + Q_{sg} \quad (62)$$

where the $Q_{reactions}$ and $Q_{evaporation}$ present the heat of reactions and evaporation, respectively, as described in Chapter 7.2. Q_{sw} is the heat transfer term between the solid bed and the walls, Q_{sg} stands for the heat transfer between the gas phase and the solid bed. In addition, the incoming and exiting kaolin flow enthalpies are calculated using Equation 63

$$\dot{Q}_{kaolin} = c_{p,kaolin} m_{kaolin} T_{kaolin} \quad (63)$$

The heat transfer terms Q_{sg} and Q_{sw} are described later in Chapters 7.4.5.1 and 7.4.5.2, respectively. The general solid phase heat continuity equation is applied for the whole furnace and for each hearth separately.

It is assumed that the surfaces of hearths have equal temperature to the kaolin in contact with them. Therefore, no heat transfer between the hearth surfaces and the solid bed exists. For each component in the solid phase, the heat capacity is assumed constant. The heat capacities are listed in Table 13.

Table 13. The heat capacities of the solid components.

Component	Heat capacity (kJ/kg K)	Reference
Water	4.18	(Perry & Green, 1997)
Kaolin	1.16	(Schieltz & Soliman, 1966)
Metakaolin	1.19	(Schieltz & Soliman, 1966)
Spinel phase	0.93	[Imerys]
Mullite	1.11	(Schieltz & Soliman, 1966)

7.4.2. Gas phase energy balance

For the gas phase the general energy equation is

$$\dot{Q}_{gas,in} - \dot{Q}_{gas,out} + Q_{combustion} + Q_{gw} + Q_{gs} + Q_{gshaft} + Q_{garms} = 0 \quad (64)$$

where the enthalpies of the incoming and the exiting gas flows are calculated using Equation 65

$$\dot{Q}_{gas} = \sum_{i=1}^{5} n_i \int_{300K}^{T_{gas}} c_{p,i} \quad (65)$$

where i denotes the gas component and 300 kelvins is used as a reference temperature. Since the gas component enthalpies vary as a function of temperature, they have to be calculated for a specific temperature. This is discussed in Chapter 7.4.5.10. $Q_{combustion}$ presents the energy provided by the burners on the hearths 4 and 6, Q_{gw} is the heat exchange term between the gas phase and the

walls, Q_{gs} presents the heat exchange term between the gas phase and the solid bed, and Q_{gsa} denotes the heat exchange between the gas phase and the central shaft and the rabble arms. Further, the heat transfer terms Q_{gw}, Q_{gs}, Q_{gsa}, are discussed below.

7.4.3. Energy balance for the walls

The energy balance equation for the wall, which is solved for each hearth separately (Assumption 9), is

$$\frac{\partial Q_w}{\partial t} = Q_{wg} - Q_{ws} - Q_{wa} \qquad (66)$$

where the heat flow terms Q_{wg}, Q_{ws} and Q_{wa} present the heat transfer between the wall and the gas phase, the wall and the solid bed, and the wall and the ambient air, respectively. They are further discussed in next subchapters. The conduction inside the furnace wall is presented in chapter 7.4.5.4.

7.4.4. Energy balance for the central shaft and the rabble arms

The energy balance of the central shaft and rabble arms is calculated for each hearth separately (Assumption 10). The energy balance equation for the central shaft and rabble arm sections is

$$\frac{\partial Q_w}{\partial t} = Q_{gsa} - Q_{sa,cool} \qquad (67)$$

where the heat flow terms Q_{gsa} and $Q_{sa,cool}$ present the heat transfer between the gas phase and the central shaft and rabble arms, and between the cooling air and the central shaft and rabble arms, respectively. They are further discussed in next chapters 7.4.5.6 and 7.4.5.7, respectively.

7.4.5. Heat transfer parameters

In this model, heat transfer occurs via convection and radiation through the seven heat exchange paths described in Assumption 8. For convective heat transfer, the convection coefficients and, for radiative heat transfer, the emissivities of the material surfaces must be calculated. The heat transfer paths and the calculation of the heat transfer variables are presented in this chapter. Additionally, the conduction mechanism inside the walls and the calculation of the gas component heat capacities are represented.

7.4.5.1. Heat transfer between the solid bed and the gas phase

Direct heat transfer between the solid bed and the gas phase (Q_{gs}) occurs by radiation and convection. Thus, the heat flux can be written as

$$Q_{gs} = Q_{rgs} + Q_{cgs} \tag{68}$$

where the radiation term Q_{rgs} is

$$Q_{rgs} = \sigma A_{gs} \varepsilon_s \varepsilon_g (T_g^4 - T_s^4) \tag{69}$$

where σ is the Stefan-Boltzmann constant, A_{gs} denotes the heat exchange area between the solid bed and the gas phase, ε_s is the emissivity of the solid bed and ε_g is the emissivity of the gas phase. The emissivity of the solid bed is temperature dependent and the gas phase emissivity is water and carbon dioxide content and temperature dependent. The emissivities of the solid bed and the gas phase are further discussed in Chapters 7.4.5.8 and 7.4.5.9, respectively. The variables T_g and T_s present the absolute temperatures of the gas phase and the solid bed, respectively.

The convective heat term Q_{cgs} in Equation 68 can be written as

$$Q_{cgs} = h_{cgs} A_{gs} (T_g - T_s) \tag{70}$$

where h_{cgs} is the heat transfer coefficient between the bed and the gas phase. The heat transfer coefficient h is calculated using the Nusselt's number presented in Equation 71.

$$Nu = \frac{hL}{k_g} \tag{71}$$

where L is the characteristic dimension and k_g is the thermal conductivity of the gas phase. In this case the characteristic dimension is the length of the heat transfer surface shown in Figure 25.

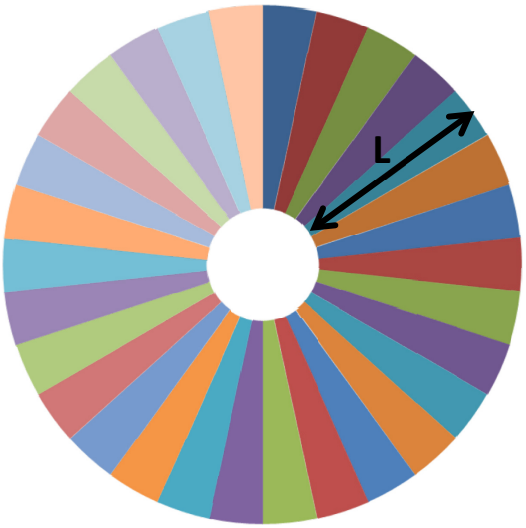

Figure 25. The solid bed surface from up showing the characteristic length L.

Since the gas flow direction in the furnace is from the bottom to the top and methane and air are not fed to the furnace until the hearth 6, the flow conditions differ between the two sections; the hearths 1 to 6 and the hearths 7 and 8. In the upper section (the hearths 1 to 6) the gas phase is moving due to the air and gas fed at the hearths 4 and 6. Though there is a small draft of air through the drop holes in the bottom hearth, the gas phase is assumed stagnant in the lower section (the hearths 7 and 8) because there is no considerable forced feed and the amount of draft can be assumed negligible while calculating the heat exchange.

For the hearths 1 to 6 the conditions for the Nusselt number calculation are assumed to be forced convection, turbulent (Re > $1*10^5$) and internal flow. For this case the Nusselt number is given by Equation (72) (Incropera et al., 2007)

$$Nu = 0.23 * Re^{\frac{4}{5}} * Pr^{0.35} \qquad (72)$$

The Reynold number in Equation 72 is calculated as

$$Re = \frac{\rho v D_h}{\mu} \tag{73}$$

where D_h is the characteristic diameter of the flow path, ρ is the density of the flowing fluid, v is the average velocity of the fluid and μ is the fluid viscosity (Pa s).

The Prandtl number describing the ratio between the momentum diffusivity and thermal diffusivity of the fluid is calculated as

$$Pr = \frac{c_p \mu}{k} \tag{74}$$

where c_p is the specific heat capacity, μ is the dynamic viscosity , and k is the thermal conductivity of the gas.

The conditions on the hearths 7 and 8 are assumed to be natural convection on the top of a hot surface. Now, the solid bed is assumed to be in a higher temperature than the gas phase, otherwise there would not be a cooling effect. According to (Incropera et al., 2007) the Nusselt number for this particular case can be evaluated as

$$Nu = 0.54 Ra^{1/4} \tag{75}$$

The Rayleigh number is written as

$$Ra = \frac{g\beta\left(T_s - T_g\right)L^3}{\nu\alpha} \tag{76}$$

where g presents the gravimetric constant 9.81 m/s^2, β is the volumetric expansion coefficient (1/T(K)), and T_s and T_g are the temperatures of solid and gas, respectively. ν is the thermal diffusivity of the gas and α stands for the kinetic viscosity of the gas. The characteristic length L is defined as

$$L = \frac{A}{P} \tag{77}$$

where A and P are the plate surface area and perimeter, respectively. The gas-solid heat exchange is calculated separately for each four or five solid volumes depending on the hearth.

7.4.5.2. Heat transfer between the solid bed and the walls

Heat transfer between the solid bed and the walls occurs only by radiation since the two surfaces are not connected to each other. The radiative heat flux Q_{rws} between the walls and the solid bed is calculated as

$$Q_{rws} = \sigma A_{sw} \varepsilon_{sw} \left(T_w^4 - T_s^4\right) \tag{78}$$

where A_{sw} presents the solid bed heat exchange surface and ε_{sw} presents the emissivity between the walls and the solid bed surface, which is affected by the gas emissivity. The ε_{sw} is calculated as in (Ginsberg & Modigell, 2011):

$$\varepsilon_{sw} = \frac{\varepsilon_s \varepsilon_w \left(1 - \varepsilon_g\right)}{1 - U} \tag{79}$$

where ε_s, ε_w and ε_g present emissivities of the solid bed, walls and gas phase, respectively. The variable U is defined as in Equation 80

$$U = (1 - \varepsilon_w)\big(1 - \varepsilon_g\big)[v\big(1 - \varepsilon_g\big)(1 - \varepsilon_s) + (1 - v)] \quad (80)$$

where the variable v presents the ratio between the heat exchange area of the solid bed and the gas phase A_{sg} and the heat exchange area between the walls and the gas phase A_{gw}:

$$v = \frac{A_{sg}}{A_{gw}} \quad (81)$$

The emissivity of the walls is assumed to be 0.90 as with a refractory material being an average radiator (Perry & Green, 1997)(page 5-29).

7.4.5.3. Heat transfer between the inner walls and the gas phase

Heat transfer between the walls and the gas phase occurs by convection and radiation and the heat flux can be written as

$$Q_{wg} = Q_{rgw} + Q_{cgw} \quad (82)$$

Where the radiation term Q_{rgw} is written as in (Meisingset & Balchen, 1995)

$$Q_{rgw} = \sigma A_{gw} \frac{(\varepsilon_w + 1)}{2} \varepsilon_g (T_g^4 - T_w^4) \quad (83)$$

where $\frac{(\varepsilon_w+1)}{2}$ is the effective emissivity (Perry & Green, 1997), which can be used if the emissivity of the material is above 0.7. The convective heat flux term is:

$$Q_{cwg} = h_{cgw} A_{wg} (T_g - T_w) \quad (84)$$

where h_{cgw} is the convective heat transfer coefficient between the wall and the gas. The heat transfer coefficient h_{cgw} is calculated using the same equations as for the heat exchange between the gas phase and the solid bed for the hearths 1 to 6.

For the hearths 7 and 8, the heat exchange scheme between the walls and the gas phase differs from the heat exchange between the solid bed and the gas phase. Now, the heat exchange surface is a vertical plate with natural convection due to the stagnant gas phase. The Nusselt number for the hearths 7 and 8 is calculated as

$$Nu = 0.68 + \frac{0.67 Ra^{\frac{1}{4}}}{\left(1 + \left(\frac{0.492}{Pr}\right)^{\frac{9}{16}}\right)^{\frac{4}{9}}} \quad (85)$$

The Raleigh number (Ra) is calculated with Equation 76 where the characteristic length is now the height of the wall. The Prandtl number (Pr) is calculated with Equation 74.

7.4.5.4. Conduction inside the walls

Figure 26 illustrates the heat transfer phenomena inside the furnace wall. The wall consists of three different brick layers and of a mild steel outer shell, which is also shown in Figure 26. The walls heat exchange scheme considers four elements; heat exchange with the gas phase, the solid bed, the ambient air and the conduction between the sections of the wall. The properties, relevant to heat exchange of the wall materials are given in Table 14.

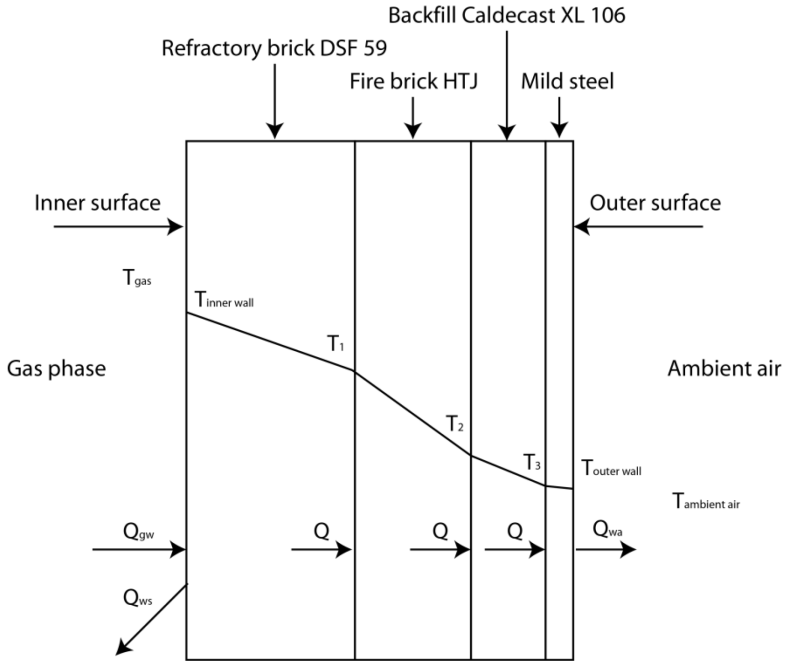

Figure 26. Structure of the walls and the heat exchange paths considering the walls.

Table 14. Wall material properties.

Material	Width (mm)	Thermal conductivity (W/m K)	Heat capacity (J/kg K)	Density (kg/m^3)
Refractory brick DSF 59 (DSF Refractories, 2009)	152	1.6	1000	2480
Fire brick HTJ (BNZ Materials, Inc., 2009)	114	0.32	1000	769
Backfill Caldecast XL 106 (Calderys, 2010)	75	0.16	1000	2350
Mild steel (0.5% carbon) (Engineers Edge, LLC, 2013)	25	54	465	7833

To solve the boundary surface temperatures of the wall layers, the heat fluxes between the walls and the gas phase and between the walls and the solid bed are calculated as described above. Next, the outer wall temperature is iterated so that the heat flux inside the wall and the heat flux to the environment are equal. The wall is considered as a multi-layered cylinder. Consequently, the heat flux through the different layers of the wall is assumed constant:

$$Q = Q_{12} = Q_{23} = Q_{34} \qquad (86)$$

Hence, the heat flux inside the wall is calculated using Equation 87 (Alopaeus, 2008)

$$Q_w = \frac{2\pi L(T_{inner\ wall} - T_{outer\ wall})}{\frac{1}{\lambda_1}\ln\left(\frac{r_2}{r_1}\right) + \frac{1}{\lambda_2}\ln\left(\frac{r_3}{r_2}\right) + \frac{1}{\lambda_3}\ln\left(\frac{r_4}{r_3}\right) + \frac{1}{\lambda_4}\ln\left(\frac{r_5}{r_4}\right)} \qquad (87)$$

where L is the height of the wall section, λ_i is the thermal conductivity of a wall layer and, r_j is the radius of the surface from the centre of the hearth. The heat flux between the outer wall and the ambient air is calculated using Equation 88

$$Q_{wa} = Q_{cwa} + Q_{rwa}$$
$$= h_{cwa} A_{wa} (T_{ambient} - T_{outer\ wall}) \quad (88)$$
$$+ \sigma A_{wa} \varepsilon_{outer\ wall} (T^4_{ambient} - T^4_{outer\ wall})$$

where Q_{cwa} is the convective heat flux term of the total heat flux and Q_{rwa} is the radiative heat flux. h_{cwa} is the convective heat transfer coefficient, Awa is the heat exchange area between the ambient air and the wall section. The emissivity of the outer wall is assumed to be constant 0.9. Calculation of the heat transfer coefficient h_{cwa} is described in Chapter 7.4.5.5.

After solving the surface temperature between the ambient air and the outer wall and obtaining the heat flux inside the wall, the temperature of the inner wall surface can be updated using the wall inner layer energy balance equation (89):

$$\frac{\partial Q_{wall\ inner}}{\partial t} = Q_{wg} - Q_{ws} - Q_w \quad (89)$$

And finally, the temperatures of the other surface layers can be updated using Equation 90:

$$\frac{\partial T_{wall\ section}}{\partial t} = -Q_w * \ln\left(\frac{r_{i+i}}{r_i}\right) \frac{1}{2\pi\lambda_i h_{wall}} \quad (90)$$

where subscript i is the number of the wall layer (number 1 presents the most inner layer and the inner surface), λ is the thermal conductivity of the wall layer material and h presents the height of the wall section.

7.4.5.5. Heat transfer between the outer walls and the environment

The heat transfer between the outer wall surface and ambient air is assumed to be natural convection on a vertical hot plate. As previously, the heat exchange coefficient is calculated using the Rayleigh number, Equation 91, and the Nusselt number, Equation 92, (Incropera et al., 2007).

$$Ra = \frac{g\beta(T_{wall\ outer} - T_{ambient})L^3}{\nu\alpha} \qquad (91)$$

where g presents the gravimetric constant 9.81 m/s^2, β is the volumetric expansion coefficient (1/T(K)), ν is the thermal diffusivity of the gas and α stands for the kinetic viscosity of the gas in the ambient air temperature. Now, $Ra_{wa} > 10^9$ and Equation 92 for the Nusselt number becomes

$$Nu_{wa} = 0.10 * Ra_{wa}^{\frac{1}{3}} \qquad (92)$$

Finally, the heat transfer coefficient between ambient air and the outer wall surface is obtained from Equation 93

$$h_{wa} = \frac{Nu_{wa}k_{air}}{L} \qquad (93)$$

where k_{air} is the thermal conductivity of the ambient air and L is the height of the wall section.

7.4.5.6. Heat transfer between the gas and the central shaft and the rabble arms

The heat exchange flux between the gas phase and the central shaft consist of the radiative Q_{rgs} and the convective Q_{cgs} heat transfer terms as shown in Equation 94. The heat transfer terms Q_{rgs} and Q_{cgs} are further described in Equations 95 and 96, respectively.

$$Q_{gs} = Q_{rgs} + Q_{cgs} \quad (94)$$

$$Q_{rgs} = \sigma A_{gs} \varepsilon_{shaft} \varepsilon_{gas} (T_{gas}^4 - T_{shaft}^4) \quad (95)$$

$$Q_{cgsa} = h_{cgs} A_{gs} (T_{gas} - T_{shaft}) \quad (96)$$

To solve the convective heat transfer coefficient h_{cgs} between the gas phase and the central shaft at the hearths 1 to 6, the following assumptions are made: the shaft is in external gas flow, the shaft is considered as a flat plate parallel to the flow and the gas flow is turbulent. Now, the heat transfer coefficient can be calculated using Equations 97-98:

$$Nu_{gs} = 0.0296 * Re^{\frac{4}{5}} * Pr^{\frac{1}{3}} \quad (97)$$

where the Reynold and Prandtl numbers are obtained using Equations 73 and 74 respectively. The Reynold number is an average of the Reynold number in the annulus between the central shaft and the hearth and of the Reynold number in the gas phase close to the shaft.

$$h_{cgs} = \frac{k_{gas}}{L} Nu_{gs} \qquad (98)$$

where L is the height of the shaft section per hearth. For the hearths 7 and 8, the heat exchange coefficient is approximated to be the same as the coefficient between the walls and the gas phase since, in both cases, the heat exchange conditions are the same: natural convection on a vertical plate.

The heat exchange equations between the rabble arms and the gas phase are similar to the case of the central shaft and the gas phase, thus the same heat flux equations 94-96 can be used, only changing the subscript *shaft* to *arms*. The Nusselt number is also calculated with the same equation 97 for the arms on the hearths 1 to 6. However, the Nusselt number calculation differs between the arms and shaft in the hearths 7 and 8. In the hearths 7 and 8, the Nusselt number is calculated using Equation 99, which applies to a long horizontal cylinder for a wide Rayleigh number range $Ra<10^{12}$ (Incropera et al., 2007) :

$$Nu = 0.60 + \frac{0.387 Ra^{\frac{1}{6}}}{\left(1 + \left(\frac{0.559}{Pr}\right)^{\frac{9}{16}}\right)^{\frac{8}{27}}} \qquad (99)$$

where the Rayleigh number is calculated using Equation 100:

$$Ra = \frac{g\beta\left(T_{gas} - T_{arms}\right)L^3}{\nu\alpha} \qquad (100)$$

where L is the diameter of the rabble arms.

7.4.5.7. Heat transfer between cooling air and the central shaft and the rabble arms

The heat flux between the cooling air and the central shaft consists of the radiative and convective terms as shown in Equation 101:

$$Q_{shaft\_cool} = Q_{rshaft\_cool} + Q_{cshaft\_cool} \quad (101)$$

The radiative and the convective heat fluxes are further derived as given in Equations 102 and 103, respectively.

$$Q_{rshaft\_cool} = \sigma A_{shaft\_cool} \varepsilon_{shaft} \quad (T_{shaft}^4 - T_{cool}^4) \quad (102)$$

$$Q_{cshaft\_cool} = h_{cshaft\_cool} A_{shaft\_cool} (T_{shaft} - T_{cool}) \quad (103)$$

The heat transfer coefficient h_{cshaft_cool} is calculated using Equation 104, which applies for flow inside a tube in turbulent conditions.

$$Nu = 0.023 * Re^{0.8} * Pr^{\frac{1}{3}} \left(\frac{\bar{\mu}}{\mu_w}\right)^{0.14} \quad (104)$$

where $\bar{\mu}$ is the dynamic viscosity of the gas in its temperature and μ_w is the dynamic viscosity of the fluid in the temperature of the wall. The Reynold and Prandtl numbers are calculated using Equations 73 and 74, respectively. For the shaft the characteristic length D_h in the Reynold equation is the inner diameter of the central shaft.

The heat transfer equations for the cooling of the rabble arms are analogous to the central shaft cooling. Only the characteristic length D_h is different. For the rabble arms it is given by Equation 105:

$$D_h = 4 * \frac{Cross\ sectional\ area\ of\ the\ arm}{Perimeter\ of\ the\ arm} \quad (105)$$

7.4.5.8. Emissivity of the solid bed

The emissivity of the solid bed is assumed to be dependent on the temperature. The solid bed consists of kaolin which is mainly a mixture of aluminium oxide and silicon oxide. The literature values for the emissivity of aluminium oxide and silicon oxide in various temperatures are given in Figure 27. In addition, as seen from Figure 27 a correlation can be derived between the emissivity of the kaolin and the temperature. Equation for the correlation is

$$\varepsilon_{solidbed} = 2.0982 * 10^{-7} * T_{solidbed}^2 - 0.00064169 * T_{solidbed} + 0.87936 \quad (106)$$

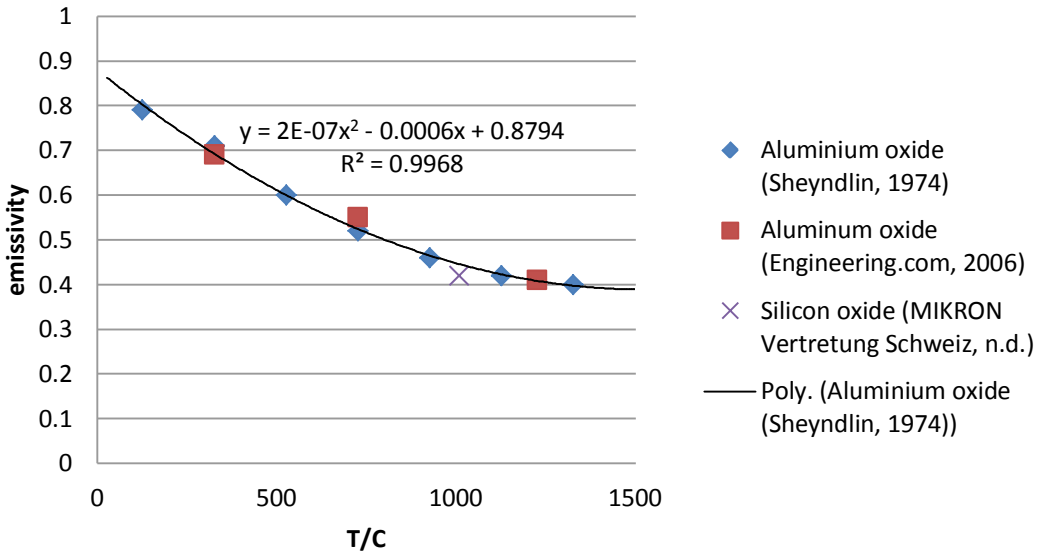

Figure 27. Graph shows the literature values of emissivities of aluminium oxide and silicon oxide and the curve of Equation 106.

7.4.5.9. Emissivity of the gas phase

The emissivity in the hearths 1 to 6 is affected by the water and carbon dioxide content and the temperature of the gas phase. Other gas phase components are not considered as they all are small two atomic components and such components do not affect the radiation properties of gas (Perry & Green, 1997). The gas phase in the hearths 7 and 8 only has oxygen and nitrogen, thus the emissivity is not calculated for those hearths. Perry and Green (1997, table 5.7) introduce a table that can be used to calculate emissivities of H2O and CO2 mixtures in different temperatures. The calculated emissivities of the gas phase in different hearths are given in Table 15 and the calculation of the emissivities is described in Appendix 2.

Table 15. The calculated gas phase emissivities.

Hearth	ε
1	0.34
2	0.32
3	0.30
4	0.27
5	0.27
6	0.23

7.4.5.10. Heat capacities of the gas components

The molar heat capacities of the gas phase components are assumed to be temperature dependent. The component heat capacities are calculated using the quantified equation 107 by (Design Institute for Physical Properties, Sponsored by AIChE, 2012). The constants A, B ,C, D and E, for each component are listed in Table 16. Figure 28 shows the calculated heat capacities for each component.

$$c_{p,i}\left[\frac{J}{kmol\ K}\right] = A + B\left[\frac{\frac{C}{T}}{\sinh\left(\frac{C}{T}\right)}\right]^2 + D\left[\frac{\frac{E}{T}}{\cosh\left(\frac{E}{T}\right)}\right]^2 \qquad (107)$$

Table 16. Constants for gas component heat capacity calculations (Design Institute for Physical Properties, Sponsored by AIChE, 2012).

Component	A	B	C	D	E
CH_4	33298	79933	2086.9	41602	991.96
O_2	29103	10040	2526.6	9356	1153.8
N_2	29105	8614.9	1701.6	103.47	909.79
H_2O	33363	26790	2610.5	8896	1169
CO_2	29370	34540	1428	26400	588

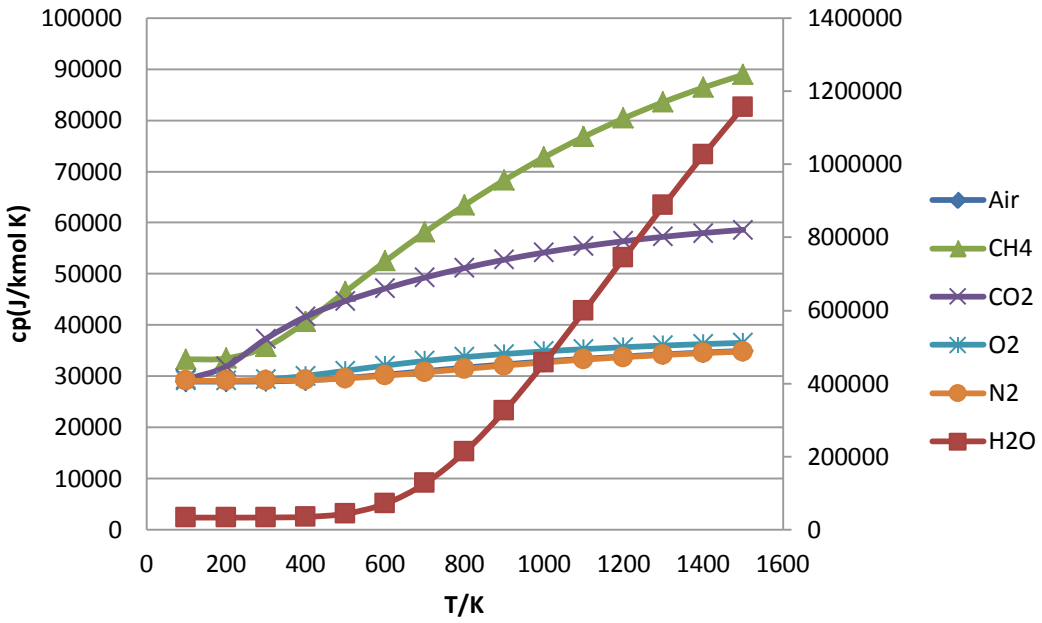

Figure 28. Temperature dependent heat capacities of the gas phase components. Water is drawn on the right side axis.

8. Experimental testing for the solid bed dynamics

The aim of the experimental testing of the solid bed dynamics is to determine the residence time of the solids on each hearth separately and to generate a solid bed dynamics matrix for each hearth describing the solids movement in the furnace. The experiments are performed with a pilot scale furnace of the Lee Moor Herreschoff furnace.

The experiments are divided into two parts; the objective of the first part of the experiments is to study the residence time distribution of the solid flow through the whole furnace. The objective for the second part is to determine the distribution of the total mass in the furnace between the hearths. Combining the results from the parts one and two, the solids residence time on each hearth can be determined and the solid bed dynamics matrix generated.

The test equipment is presented below and the methods and results of the experiments are discussed in detail in the next subchapters. The solid bed dynamics matrix is generated in Chapter 8.4.

8.1. Description of the test equipment

The main equipment used for the testing includes a pilot scale furnace and a continuous weight proportioner. The pilot scale multiple hearth furnace is a 1:12 ratio replica of the industrial furnace without heating equipment. The rabble arm configuration is the same as it is in the Lee Moor MHF. The walls are made of Perspex allowing observing the movement of the solid bed. The dimensions of the pilot furnace are given in Table 17.

Table 17. Dimensions and technical information of the pilot furnace and its motor.

Height	80 cm
Radius	25 cm
Gap between hearths	9 cm
Central shaft speed interval	0… 5 RPM
Motor power	190 W
Voltage	220/330/440 V

Figure 29 presents the pilot scale furnace and shows the rabble arms.

Figure 29. Pilot scale multiple hearth furnace (left) and the rabble arms on the plates (right).

An Engelhardt continuous weight proportioner (Figure 30) is used as the feeder device. The feeding mechanism consists of a rough and fine streams separated by a weighing pan. The desired feed rate can be entered to the feeder by accuracy of 10

grams per hour. The material is fed from the container (up left in Figure 30) to the rough feeding section. From there, the material is moved to the fine feeding section through a weighing pan which discharges the material to the fine feeding section in predetermined cycles. The cycle time is adjusted to the desired feed rate and it is calculated automatically by the machine. The material stream is fed from the fine feeding section to the furnace.

Figure 30. The feeder device.

8.1.1. Estimating the feed rate for the pilot furnace

Before executing the tests with the described equipment, a correct feed rate must be calculated for the pilot furnace. The feed rate of the industrial scale furnace varies normally between 80 to 125 kg/min. As the pilot furnace is a true geometrical replica of the real furnace, the feed rate can be scaled in the matter of volume (Johnstone & Thring, 1957). Assuming the feed material has a constant density and as the pilot furnace is a 1:12 scale model of the industrial furnace, the volumetric scaling ratio is: $\left(\frac{1}{12}\right)^3 = \frac{1}{1728}$. The scaled feed rates are calculated using Equation 108. Table 18 presents few scaled feed rates for the pilot furnace.

$$Feed\ rate_{pilot} = \frac{1}{1728} * Feed\ rate_{industrial} \qquad (108)$$

Table 18. Industrial feed rates and corresponding pilot feed rates.

Industrial feed rate (kg/min)	60	70	80	90	100	110	120	130
Pilot feed rate (g/min)	34.7	40.5	46.3	52.1	57.9	63.7	69.4	75.2

8.2. Studying the residence time distribution of the furnace

The residence time distribution through the whole pilot furnace was studied using tracer experiments. Two different tracer materials were used and the results were compared with the ones presented by Thomas et al. (2009) to see if the residence time distribution curve of the pilot furnace follows the same shape with the residence time curve of the real industrial furnace. Next, the method used to

examine the residence time distribution is described and finally the results are presented.

8.2.1. Method for examining the residence time distribution

Before executing the tracer experiments the tracer material has to be chosen. The material has two main criteria, it has to be separable from the clay powder after the experiments and it should have relatively similar flow properties as the clay powder (Thomas et al., 2009). The tracer material is separated from the powder by sieving, therefore different seeds are a viable option as tracer material as they withstand the mechanical stress caused by sieving and do not break down. Also, the bulk densities of different seeds, for example 592 kg/m3 (ANSI, 1998) for sesame seeds and 338 kg/m^3 (Anon., 2013) for coriander seeds, are close to the bulk density of kaolin powder which is 350 kg/m^3. However, due to the relatively small size of the seeds it is assumed that the flow properties can be neglected. In this case it was also noticed during the experiments that the seeds were carried with the clay powder and their flow pattern was similar.

The tracer experiments were executed using a feed rate of 70 g/min corresponding to the real feed rate of about 120 kg/min. The rotation speed of the central shaft was 3 RPM.

The steps of the tracer experiments were the following:

1) The pilot furnace was operated to a steady-state. When the total output from the bottom drop holes equaled the feed rate, the pilot was determined to be in a steady-state.
2) 100 grams of tracer material was weighed and dosed into the pilot during one minute.
3) Samples were collected from the two bottom drop holes. From the drop hole A samples were taken every 5 minutes for the first 20 minutes, and

then every minute thereafter until 46 minutes had elapsed. From the drop hole B, the samples were taken about every 7 minutes. One sample is the total output from the drop hole during one time interval.

4) After completing the sampling, the seeds were separated from the samples by sieving and weighted.

8.2.2. Results of the residence time investigation

The tracer experiment was first executed using black sesame seeds for their smaller size compared to coriander seeds and for their black colour. The results are shown in Figure 31 and the measured values are listed in Appendix 4. The peak of the residence time distribution curve occurs at around 20 minutes and the mean residence time through the pilot furnace is a little over 23 minutes. When comparing the results to the industrial results presented in Figure 4 it is clear that the peak of the pilot furnace curve appears much sooner than in the industrial experiment (42 minutes). However, the shapes of the pilot and industrial curves are similar. At first, the difference was thought to be caused by the difference between the properties of the sesame seeds and the clay powder, mainly the bulk density. Therefore, the tracer test was performed again, now using coriander seeds as the tracer since they have a bulk density close to the kaolin powder. Also, the sampling interval was modified to prevent the high peak obtained in the first test at 20 minutes.

The second residence time distribution experiment showed similar results as the first experiment as shown in Figure 31 and the measured values are listed in Appendix 4. The peak of the distribution curve occurs at around 22 minutes and the mean residence time is about 24 minutes, which differs from the industrial experiments. It was observed during the experiments that the seeds and the kaolin powder had the same flowing path and the seeds drifted along with the kaolin

powder. Therefore, the assumption of neglecting the flow properties in this case is viable.

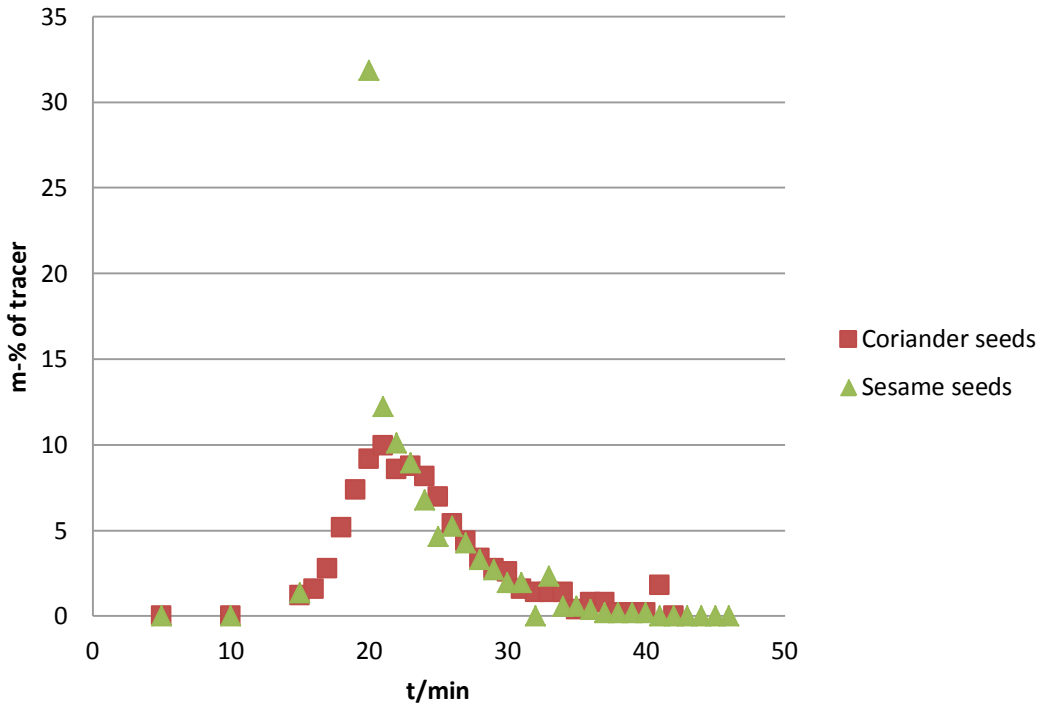

Figure 31. Results from the traces experiments. Graph shows the percentage of the tracer from the total mass of the tracer.

Since both of the two tracer experiments were executed using the same rabble arm rotation speed of 3 RPM as was in the case of industrial scale experiment and the pilot furnace is an identical 1:12 ratio replica of the industrial furnace and the only variable affecting the residence time is the central shaft rotation speed, it can be concluded that the central shaft rotation speed should be scaled down to achieve the same mean residence time. However, because the shape of the residence time distribution curve obtained from the pilot experiments is comparable to the industrial tests, the flow pattern of the solids can be assumed to be similar in both furnaces. Therefore, the pilot furnace can be used to study the mass distribution between the hearths, which is performed next.

8.3. Studying the mass distribution between the hearths

The mass distribution is studied for a nominal state which is the operation state of the furnace. Combining the results from the residence time distribution experiments together with the information of how the mass is distributed between the eight hearths, the residence time of the kaolin on each hearth can be obtained. Next, the method for studying the mass distribution is described and then the results are presented.

8.3.1. The method for examining the mass distribution

The mass distribution experiments were executed using a feed rate of 70 g/min corresponding to the real feed rate of about 120 kg/min. The rotation speed of the central shaft was 3 RPM. The steps of the mass distribution experiments were the following:

1) The pilot furnace was operated to a steady-state. When the total output from the bottom drop holes equaled the feed rate, the pilot was determined to be in a steady-state.
2) The feeder and the rabble arms of the pilot were stopped.
3) The furnace was disassembled and the mass of the material on each hearth was weighed. In addition, a photo was taken on each hearth with kaolin on it.
4) The furnace was assembled back.

8.3.2. The results of the mass distribution investigation

First, four experiments were made to determine the mass distribution between the hearths. The mass distributions obtained in the experiments are shown in Figure 32

that also shows the average distribution of the four tests. The measured values of the masses on the hearth bottoms are listed in Appendix 4. Clearly, the hearths 3 and 7 have the largest portions of kaolin, whereas the hearths 1 and 2 have the smallest portions. This indicates that the material spends relatively short time on the first two hearths and a much longer time on the hearths 3 and 7. The repeatability of the four tests was considerably good by observing Figure 32, since none of the measurements differ much. The mass distribution between the hearths can be assumed not to be affected by the central shaft rotation speed, since the previous residence time distribution experiments showed that the solids flow dynamics are not affected by the rotation speed of the central shaft because the shape of the residence time curves of the both pilot and the industrial scale tests were comparable.

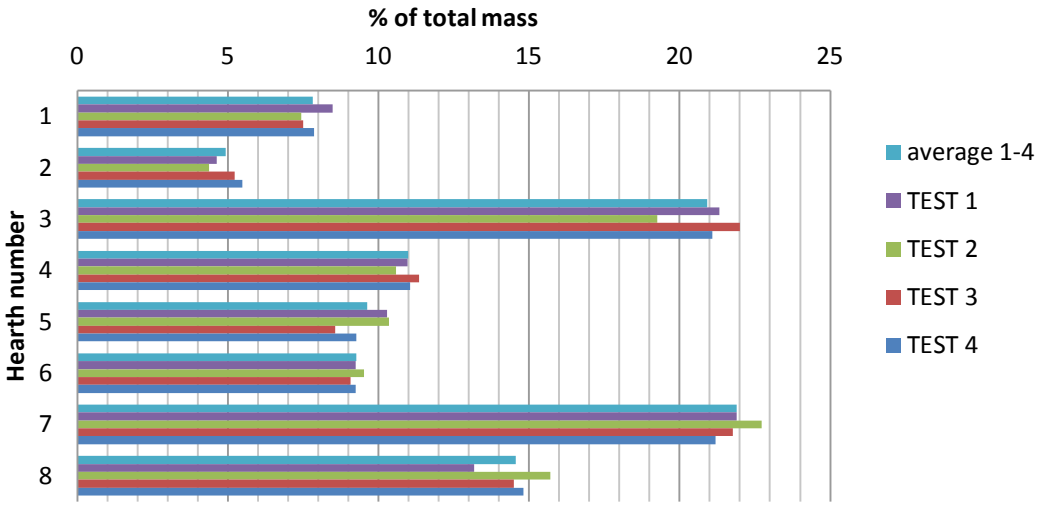

Figure 32. Mass distribution between the hearths from the tests 1, 2, 3, 4 and the average of those.

The mean residence time through the pilot was also calculated based on the mass distribution tests. The mean residence time is the total mass inside the pilot divided by the feed rate. The mean residence times are given in Table 19. From the values presented in Table 19, it can be noticed that the mean residence times obtained by

the mass distribution tests are not similar with the mean residence time determined by the tracer experiments. This inequality is caused since not all of the material inside the furnace is moving, but some of the material stays stagnant next to the walls in the 'in-hearths' or near the central shaft in the 'out-hearths'. This phenomenon can be seen from the photos presented in Appendix 3.

Table 19. Mean residence times calculated from tests 1, 2, 3 and 4.

Test	Mean residence time (min)
1	35.2
2	29.9
3	29.9
4	30.7

The mass distribution experiment was repeated again for the feed rate of 70 g/min (TEST 5) and for the feed rate of 50 g/min (TEST 6) to study the effect of the non-moving mass and the feed rate to the mass distribution and the mean residence time. Table 20 shows the mean residence times calculated from these test results. Table 20 shows that the non-moving material has a great impact on the mean residence time and on the contrary the effect of the feed rate is considerably small to the mean residence time. Now, when considering the non-moving mass when calculating the mean residence time, the mean residence times are comparable with the mean residence times obtained from the tracer experiments. Furthermore, it can be said that the non-moving mass is the reason behind the difference seen between the mean residence times acquired by the two methods, since the separation of non-moving mass and moving mass was not perfect. For example, on the top of the hearths there were thin layers of kaolin powder that were not moving but could not be separated from the moving mass.

Table 20. Mean residence time calculations considering different feed rates and non-moving mass.

Test	Mean residence time (min)
5, total mass	33.2
5, considering non-moving mass	26.8
6, total mass	33.3
6, considering non-moving mass	26.7

Figure 33 shows the mass distribution of the total mass acquired from the tests 5 and 6 compared with the average of the tests 1 to 4. The test 5 seems comparable with the previous tests but the test 6 differentiates more on the hearths 3 and 6. However, there is no obvious pattern which would describe the difference.

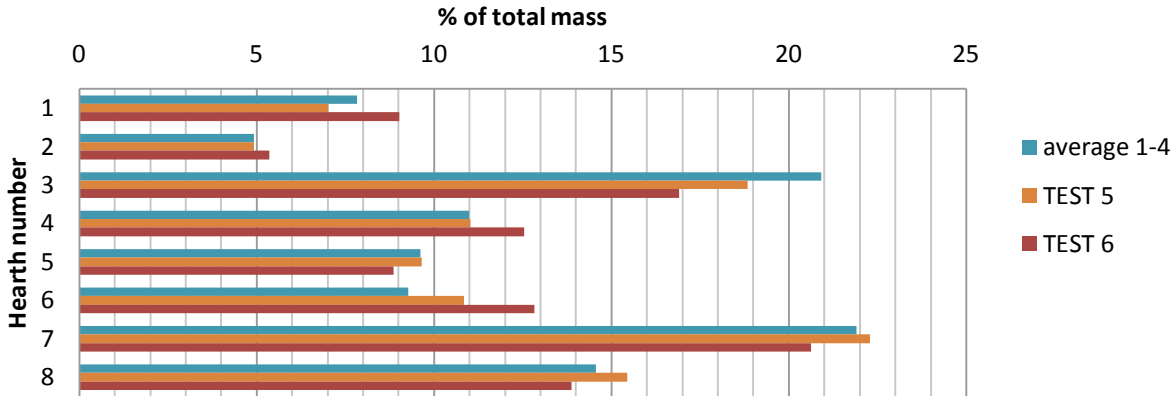

Figure 33. Graph showing distribution of the total mass in the furnace for test 5 and 6 compared with the average of the tests 1 to 4.

Figure 34 shows the distribution of the non-moving mass of the total mass on each hearth. The feed rate seems not to be a factor influencing the relative amount of non-moving mass. The difference on the hearths 5 and 8 can be explained by the difficulties in separating the moving and non-moving mass from each other. However, Figure 34 shows that the portion of non-moving mass can be over 30 percent of the total mass on each hearth varying from 5 to 34 percent.

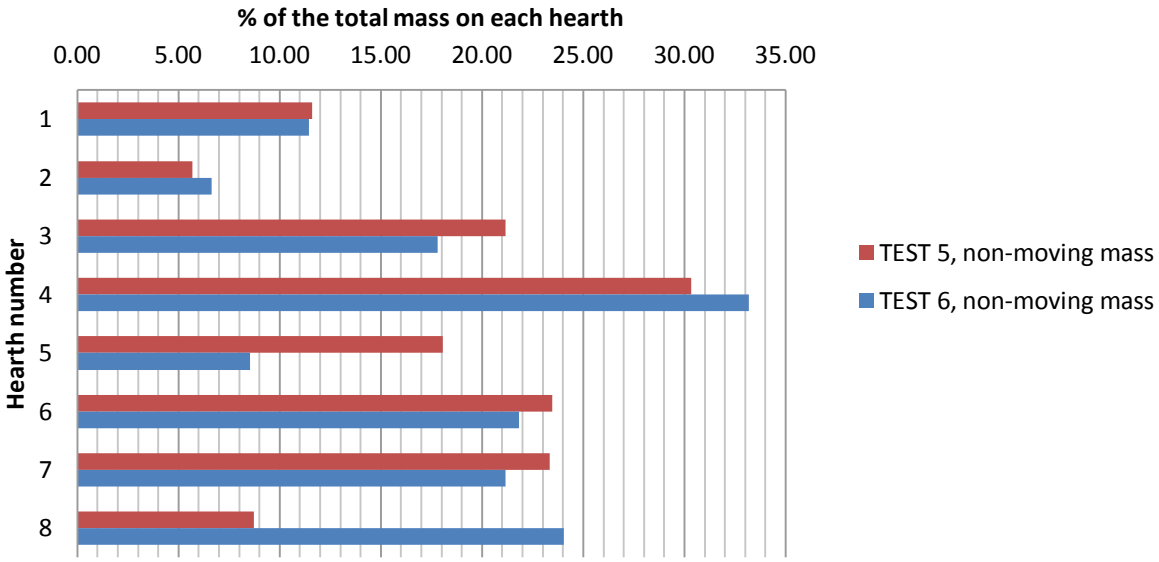

Figure 34. The distribution of the non-moving mass of the total mass on each hearth,

Figure 35 illustrates the differences between the two feed rates and the distributions of the moving and the non-moving mass compared to the total moving mass and to the total non-moving mass, respectively. There seems to be little difference between the proportions of the moving masses of the two experiments. On the contrary, there seems to be more deviation between the non-moving masses, particularly on the hearths 3, 4, 5, 7 and 8. However, since the differences are not large besides on the hearth 5, and the amount of the non-moving masses are small, the most likely reason for the difference are again the difficulties in the separation of the moving mass and the non-moving mass.

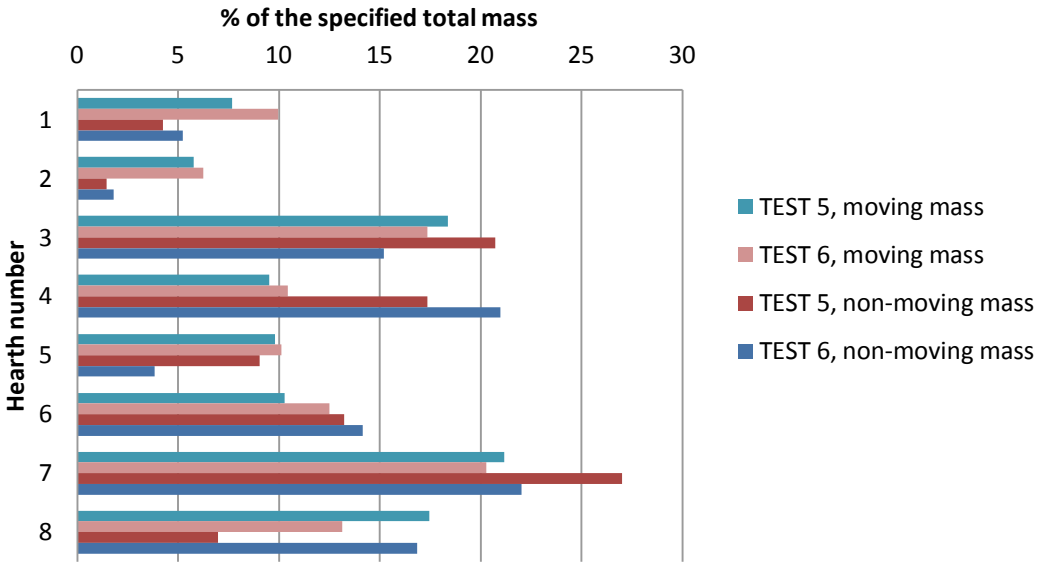

Figure 35. Graph comparing the differences between the two feed rates and the distributions of the moving and non-moving mass to the total moving mass and to the total non-moving mass, respectively.

8.4. Generating the solid bed dynamics matrix

A solid bed dynamics matrix is generated for each hearth separately to model the solids movement on the bottoms of the hearths. According to Assumption 1, the solid bed on one hearth can be divided to four or five volumes according to the furnace characteristics. Furthermore, during one rotation of the rabble arms, there is a proportion of each volume that is moved to the previous volume or to the next volume or stays in the same volume. Equation 109 presents the solid bed dynamics matrix of the upmost hearth where parameters α and a_i determine the solid movement on the first hearth.

$$D_1 = \begin{matrix} 1-a_1 & a_1 & 0 & 0 & 0 \\ a_1-\alpha & 1-a_1-a_2+\alpha & a_2 & 0 & 0 \\ 0 & a_2-\alpha & 1-a_3-a_2+\alpha & a_3 & 0 \\ 0 & 0 & a_3-\alpha & 1-a_4-a_3 & a_4 \\ 0 & 0 & 0 & a_4 & 1-a_4 \end{matrix} \quad (109)$$

In the solid bed dynamics matrix D, the row i and column i counts for the corresponding volume i. The parameter α presents the net forward flow through the volumes, which accounts for both forward and backward flows. The matrix elements a_i present the forward flow from the current volume (i+1) to the next volume i during one full central shaft rotation and the matrix elements (a_i – α) present the backward flow from the current volume i to the previous volume during one full central shaft rotation. The model assumes that there exists no forward or backward flow which would go to the second next or to the second previous volume during one full central shaft rotation. In Equation 109, there is no parameter α in elements (4,4) and (1,1) because the feed enters to the volume 4 and the material is dropped from the volume 1 to the lower hearth. Equation 110 shows the numerical form of the D matrix of the first hearth. The solid bed dynamics matrices are derived similarly for other hearths.

$$D_1 = \begin{matrix} 0.4645 & 0.5355 & 0 & 0 & 0 \\ 0.0255 & 0.4390 & 0.5355 & 0 & 0 \\ 0 & 0.0255 & 0.4390 & 0.5355 & 0 \\ 0 & 0 & 0.0255 & 0.4390 & 0.0255 \\ 0 & 0 & 0 & 0.0255 & 0.9745 \end{matrix} \quad (110)$$

The parameters used in the solid bed dynamics matrix are chosen so that the mass distribution between the hearths and the residence time distribution matches the pilot experiments. Figure 36 shows a bar graph comparing the average mass distribution obtained from the pilot experiment 1 to 4 and the mass distribution in the model. As seen from Figure 36, the mass distributions match each other relatively well.

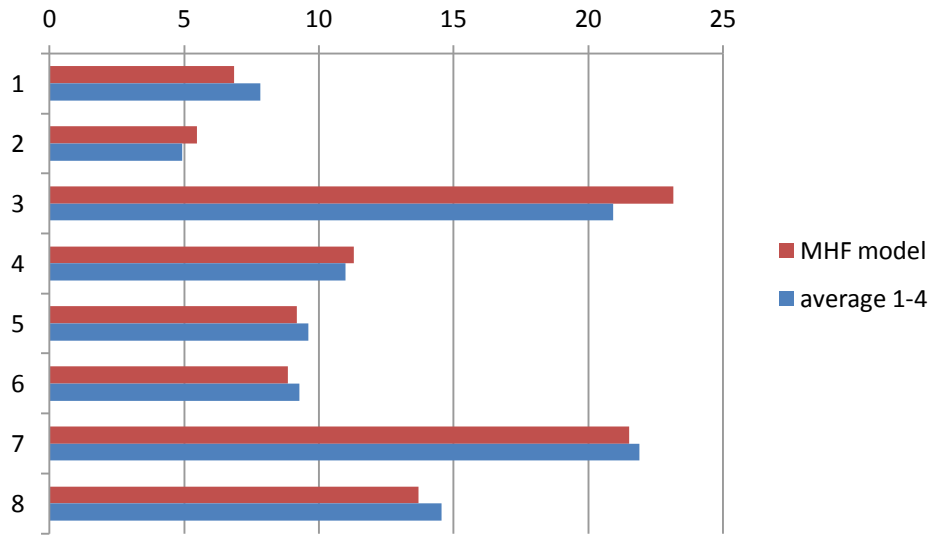

Figure 36. Bar graph showing the mass distribution in the MHF model and the average value of the experimental tests 1-4.

Figure 37 presents how the residence time distribution is implemented in the MHF model. Comparison between the residence time distribution curve of the model and the curve obtained in the industrial experiment presented in Figure 4 shows that both of the curve have similar shape. In addition, in both cases the first observations of the tracer at the outlet can be seen at around 20 minutes and the most of the tracer has exited the furnace at 80 minutes. In overall, the shape of the residence time distribution curve and the mass distribution in the MHF model are in-line with the results from the experimental tests.

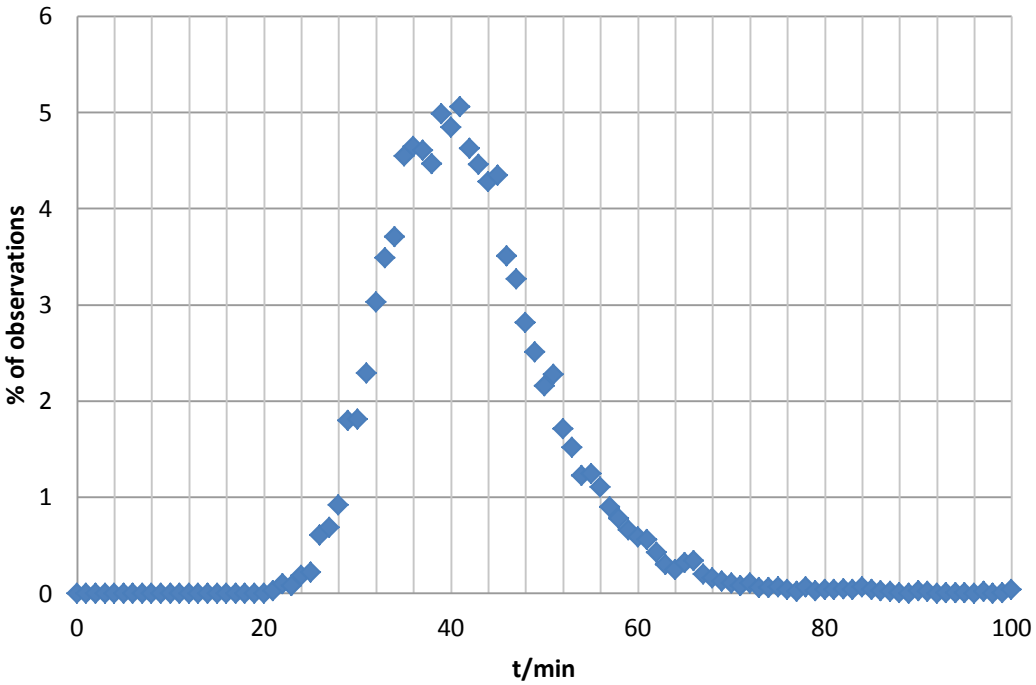

Figure 37. Graph showing the residence time distribution curve in the MHF model.

9. Solving the system of equations of the MHF

The overall scheme to solve the mathematical model of the MHF is given in Figure 38. The scheme provides the main modules of the model and the used solving algorithm for each module. One time step in the model solving scheme is divided to five consecutive steps: 1) the reaction rates, 2) the solid bed mass balance, 3) the gas phase mass and energy balance, 4) the temperatures of the walls, cooling air, arms and shaft, and 5) the solid bed energy balance. An initial stage of the furnace conditions is given for the model to begin the solving procedure.

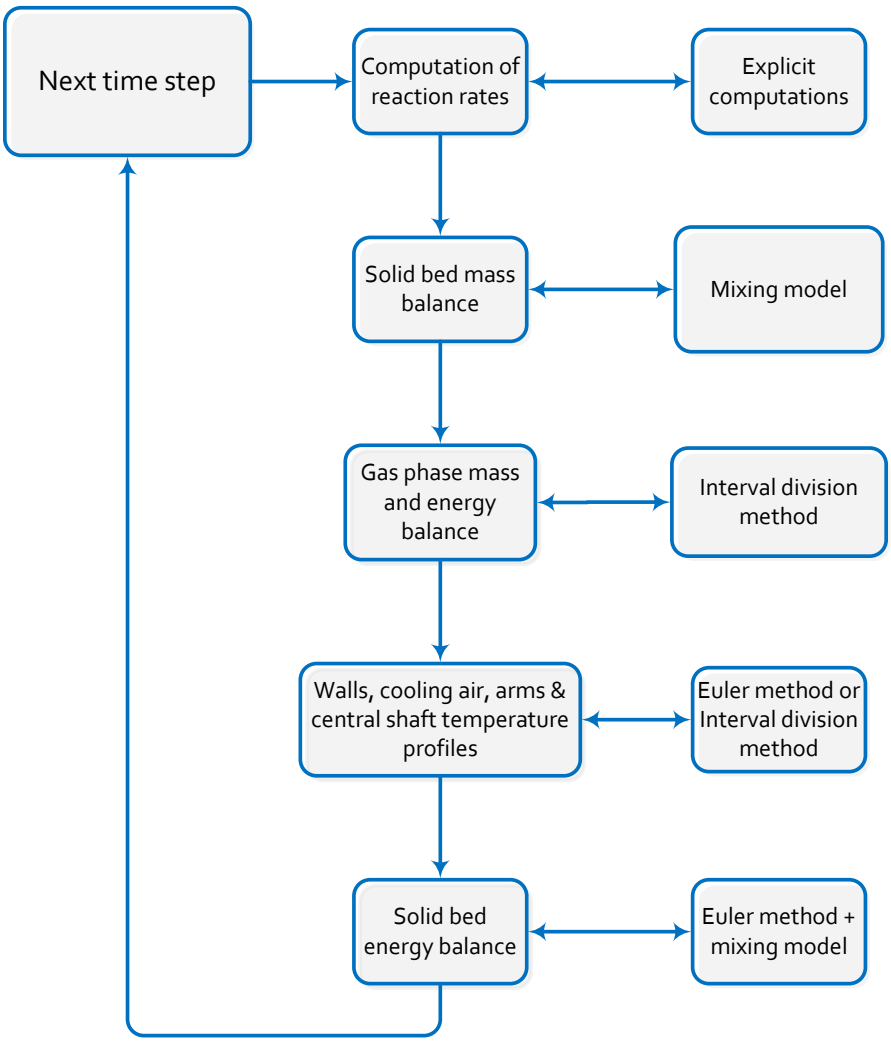

Figure 38. Model solving scheme for the MHF simulator.

The first step is to compute the reaction rates. The reaction rates for each solid component are calculated in the solid temperature using the Arrhenius equation.

The second step, the solid bed mass balance, is solved using the determined reaction rates and implementing the mixing model. The mixing model uses the solid bed dynamics matrix D to calculate the solid bed movement.

The third step is to solve the mass and energy balance of the gas phase. The gas phase temperature is solved by using the internal division method. The initial division boundaries are calculated from the gas temperature of the previous time step. Next, the current gas phase temperature is iterated so that the energy balance of the corresponding hearth is zero.

The fourth step includes solving the temperature profiles of the walls, cooling air, rabble arms and the central shaft. The temperature profile of the walls is solved by first iterating the temperature of the outer wall surface so that the energy balance of the surface equals to zero. The temperature of the other surfaces of the wall layers is solved from the inner layers towards the outer layers. The temperatures of the cooling air, arms and the shaft are calculated using the Euler method. The Euler method is implemented in the model as in Equation 111:

$$y_{n+1} = y_n + h * f(t_n, y_n) \qquad (111)$$

where the value of y_n is an approximation of the solution to the ordinary differential equation (ODE) at time t_n: $y_n \approx y(t_n)$. The step size h used in the solving algorithm is 20 seconds.

The fifth step is to solve the energy balance of the solid bed. The solids energy balance is solved by combining the Euler method, to determine the temperature of the current stage, and the mixing model, to determine the transferring of energy in the solid bed between the bed volumes. After solving the solid bed energy balance,

the current time step is finished. Subsequently, the solving procedure of the next time step is initiated by promoting the solution of the current time step as the initial stage of the next time step.

The model equations and the model parameters and their initial values are organised and tabled according to the above solving algorithm steps in Appendix 5.

10. Description of the testing environment and the graphical user interface

The testing environment used in this thesis was MathWorks™ MATLAB®. MATLAB (**mat**rix **lab**oratory) is a numerical computing environment and a fourth-generation programming language, which allows matrix manipulations, plotting of functions and data, implementation of algorithms, creation of user interfaces, and interfacing with programs written in other languages. MATLAB is widely used in academic and research institutions as well as industrial enterprises.

To make the use of the dynamic simulator more user friendly, a graphical user interface was developed. The GUI provides the user with control over several process and simulation parameters such as feed moisture percentage and simulation time. The main interface of the GUI is presented in Figure 39.

The simulation parameters; the feed moisture, the feed temperature, the burning gas and air temperature, the cooling air flow and temperature, the rotation speed and the simulation time, can be inserted to the parameter boxes. In addition, the simulation parameters can be saved and loaded for further use. The input data series, including the feed rate and the gas and air flows to the burners on the hearths 4 and 6, can be downloaded using the 'Load data series' button.

After running the simulation the simulation results are saved from the 'Save results' button. Next, the results plotting window can be opened from the 'Plotting options' button.

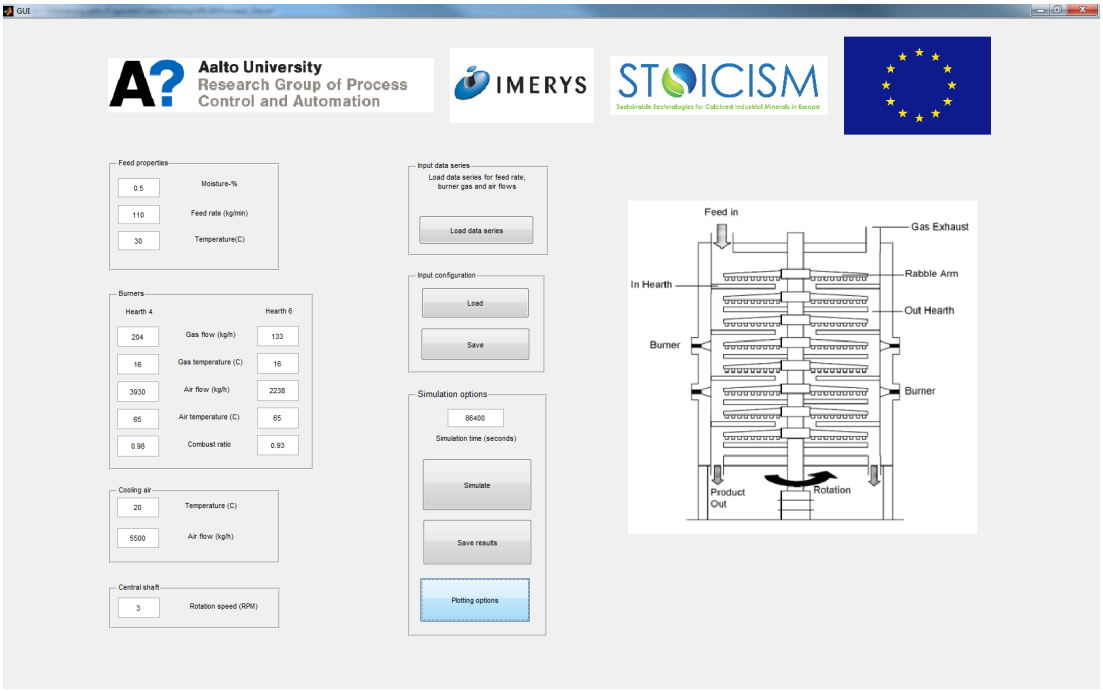

Figure 39. The main window of the simulator GUI.

The plotting options window is shown in Figure 40 The simulation results can be downloaded from the 'Import results' button for plotting and the results variables are loaded to the upper list box. The simulation results can be plotted by choosing the variable from the list box. The simulation results can also be compared with the other results or data and the comparison data is downloaded from the 'Choose results to compare' button. In the plotted figure of each hearth the simulation results are presented in blue colour and the comparison data is shown in red colour.

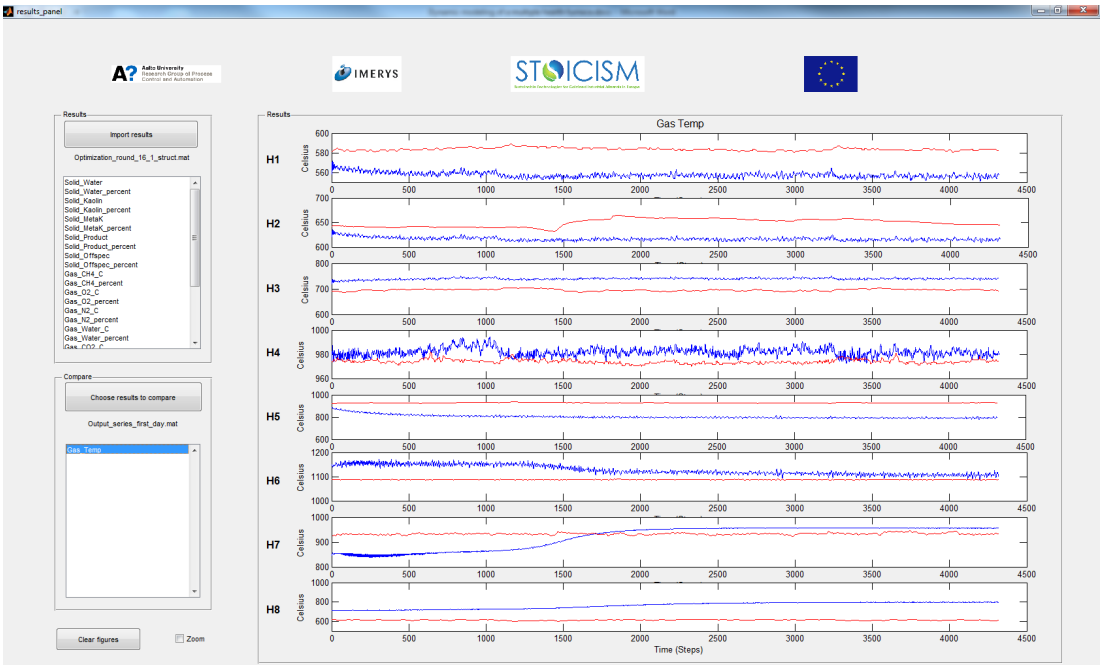

Figure 40. The results plotting window of the simulator GUI.

11. Testing the MHF model

The MHF model has been implemented in the MATLAB environment. Before the model can be tested the industrial data has to be pre-processed; the outliers and noise are removed. After the pre-processing, the model is first fitted to the steady-state operation measurements and finally the model can be tested for the dynamic behaviour.

Currently, IMERYS has provided the industrial data from a period of beginning of May 2013 to the end of November 2013. The model utilises five different inputs; the solid feed rate (kg/min), the gas and air flows (kg/h) to hearth 4 and the gas and air flows (kg/h) to the hearth 6. The temperature measurements from the gas phase next to the wall on the hearths 2 to 8 and the exhaust gas temperature are used as the output variables to validate the model. The gas phase temperature measurements used are averages of all the measurements from the specific hearth. Table 21 shows the number of the gas temperature measurements from each hearth and the exhaust. The measurements used in the simulation were extracted from the IMERYS database as Excel sheets. Afterwards, the data in the Excel sheets was converted to MATLAB structure files and concurrently the data was pre-processed to remove the outliers and noise from the measurements.

Table 21. Location of the temperature measurements of the gas phase and the number of the temperature measurements.

Location of temperature measurement	Number of temperature measurements
Exhaust	2
Hearth 2	2
Hearth 3	2
Hearth 4	4
Hearth 5	1
Hearth 6	4
Hearth 7	1
Hearth 8	2

11.1. Data pre-processing

The outliers and noise was removed from the measurements data by utilising the Hampel filter (Pearson, 2005). The Hampel filter is based on a moving-window implementation of the Hampel identifier. The Hampel filter constructs a moving data window centered at the current value x_k that includes K previous values, x_{k-K} throughx_{k-1}, and K future values, x_{k+1} through x_{k+K}. The Hampel identifier is then applied to the central point x_k in this moving window based on the median of the $2K + 1$ data values in the window and the mean absolute deviation (MAD) scale estimate computed from these data values. If x_k is declared to be an outlier, it is replaced with the median value from the data window; otherwise, it is not modified.

Also, as the sampling interval of the data is 30 seconds and the length of one time step of the model is 20 seconds, thus more data points must be created. This is executed by using linear interpolation according to Equation 112

$$y = y_a + (y_b - y_a) * \frac{x - x_a}{x_b - x_a} \text{ at the point (x,y)} \quad (112)$$

where the data point (x,y) is between the data points (x_a,y_a) and (x_b,y_b).

11.2. Steady state temperature profiles

To calculate the steady-state temperature profile, data from May 2013 was first examined to find the steady operation periods. From the data of May 2013 the feed rate of 120 kg/h had the longest steady-state operation period and it was used to adapt the model to the steady operation measurements. From this steady operation period the mean values of the input variables were calculated and they are given in Table 22.

Table 22. The steady-state inputs and outputs used for model adaptation.

Variable	Value
Feed rate	120 kg/min
Gas flow H4	221.03 kg/h
Air flow to H4	4191.4 kg/h
Gas flow to H6	133.17 kg/h
Air flow to H6	2381.4 kg/h
Extraneous air to H8	2086.8 kg/h
Cooling air flow	5280 kg/h
Cooling air exit temperature	160 °C
Product exit temperature	750 °C

The steady-state profile is fitted by optimizing the model parameters so that the mass and energy balance errors when comparing the model outputs to the

measured data are minimized. Four different types of model parameters are used in the model:

1) Burning ratios: *a* & *b* (at the hearths 4, 5 and 6 as shown in Table 23). The burning ratios are used to distribute the energy obtained from the combustion of methane between the different volumes because if all of the methane would be burned in the volume next to the walls its temperature would increase too high.

Table 23. The burning ratios.

		Volume			
		1	2	3	4
Hearth	4	$b*(1 - b)^3$	$b*(1-b)^2$	b*(1-b)	b
	5	$a*(1-a)^4$	$(1-a)^5$	0	0
	6	$a*(1-a)^3$	$a*(1-a)^2$	a*(1-a)	a

2) Form and view factor *Fs* for the solid bed surface areas. The form and view factor described the surface shape and it is used to match the energy balances of gas and solid phases on each hearth.
3) The central shaft has insulation, but its characteristics are unknown. Therefore, a heat exchange area multiplier *F* is introduced for heat exchange between the central shaft and the gas phase and between the rabble arms and the gas phase to present the insulation. The multiplier F can be estimated from the energy the cooling air absorbs from the furnace since the amount of the cooling air and the inlet and exit temperatures of the cooling air are known.
4) Extraneous air flow to hearth 8 through the bottom drop holes. This extraneous air flow is introduced for cooling purposes since there are no other mechanisms cooling the solid bed at the hearths 7 and 8 and it is known that the solid bed reaches temperature up to 1050 °C at the end of hearth 6 and the solids exit the furnace at temperature around 750 °C. In

addition, it was confirmed from the operative personnel at the plant that there really exists draft through the drop holes.

Figure 41 presents the simulated steady-state temperature profiles of the solid bed (red line) and of the gas phase (blue line) at the feed rate of 120 kg/h. The green triangles in Figure 41 denote the measured steady-state values of the gas phase temperature next to the walls. The simulated temperature profile matched well to the measured gas temperature besides on the hearths 5 and 8. On the hearth 5 the difference is 150 °C and on the hearth 8 the difference is 250 °C. The high value of the measured gas temperature at the hearth 8 is interesting since if the temperature of the gas phase would be so high the temperature gradient between the gas phase and the solid bed would be too little to provide the cooling effect to the solid bed. In addition, as the extraneous air entering the hearth 8 has ambient temperature of 20 °C, it cannot have such a high temperature as the measured one is. It can be assumed that the difference between the model and the measurement is caused by a measurement error. Another interesting phenomenon can be seen on the hearths 4 and 6 where the temperature of the gas phase is actually higher in the middle volumes than in the volume next to the burners. This can be explained by the assumption done to implement the burning ratios; not all of the methane is burnt in the outer most volume but a portion of the heat is released in the following volumes in the direction of the gas flow. The solid bed temperature rises steadily through the first two hearths where the small amount of free water is evaporated. Also, the relatively slow increase of temperature is explained by the fact that the solids move through the hearths 1 and 2 considerably fast as demonstrated in the mass distribution pilot tests. On the hearth 3 the solids temperature increase 200 °C in the volume where the solids enter the hearth. After the solid temperature reaches 450 °C the dehydroxylation reaction initiates and the temperature increases steadily through the hearths 3, 4 and 5. After all of the kaolin has reacted to form metakaolin the temperature of the solid phase starts to increase more

rapidly once more. The solid bed reaches its peak temperature at the end of the 6th hearth and the beginning of the 7th hearth. The solid bed temperature begins to decrease at the hearth 7, due to the effect of the endothermic mullite formation reaction which occurs when the temperature exceeds 1050 °C and due to the cooling effect of the gas phase.

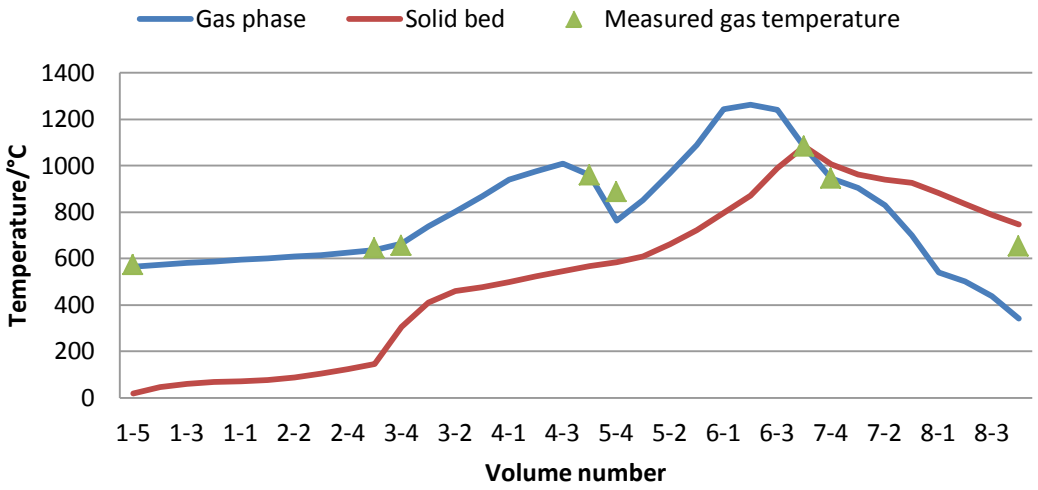

Figure 41. The steady-state temperature profile of the MHF at the feed rate of 120 kg/h. The x-axis presents the volumes of the solid and the gas phases organised in the order of the solid flow from top to bottom.

Figure 42 illustrates in which hearth each of the calcination reactions occur in the furnace and how the composition changes in the solid bed through the MHF. The volume 1-5 (1st hearth - 5th volume) is the volume where the kaolin is fed into the furnace and the volume 8-4 is the volume where the product exits the furnace. Figure 42 confirms that the metakaolin formation occurs through the hearths 3, 4 and 5, as it was seen in Figure 41 and all of the kaolin has reacted to form metakaolin at the end of the hearth 5. Next, the metakaolin is turned into the product towards the end of the sixth hearth. The product formation reaction is enhanced since the burners provide a lot of heating to the hearth 6 and the reaction itself is exothermic. The fourth reaction, mullite formation, takes place at the time

the solids are dropped from the hearth 6 to 7. In this case, the output from the furnace consists of 95 mass-% of the product and 5 mass-% of the offspec.

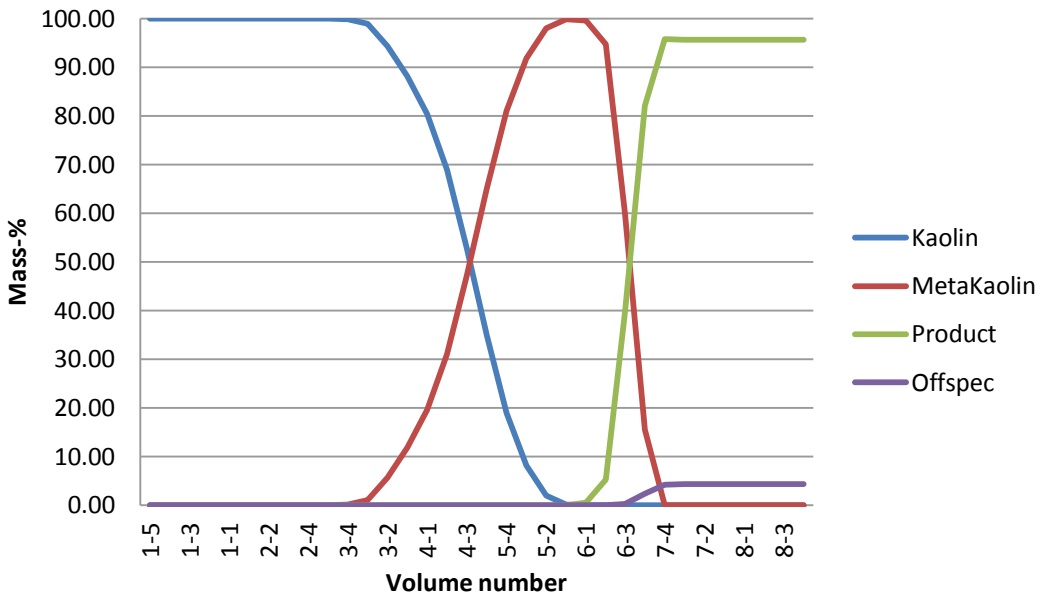

Figure 42. The steady-state composition profile of the solid bed at the feed rate of 120 kg/h. The x-axis presents the volumes of the solid and the gas phases organised in the order of the solid flow from top to bottom.

11.3. Results of the dynamic tests on the MHF model

The motivation to build the dynamic model of the MHF was to study and understand the dynamic behaviour of the physico-chemical reactions occurring inside the furnace and how those are affected by different input variables and disturbances. In addition, after the response behaviour of the furnace is known, the simulator can be used to test and implement advanced process control strategy for the industrial application.

11.3.1. Studying the model response to step changes in the input variables

The main input variables of the MHF model are the feed rate and the gas and air flows to the hearths 4 and 6. The main output variables are the temperature profile of the gas phase and the quality variables; product content on the hearths 6 and 7 and the offspec content on the hearth 7 as presented in Figure 43. The model responses are studied to understand how the output variables behave when the input variables are changed. In addition, the results from the step response tests can be used for preliminary control design. The model response was first studied by introducing a step change at 833 minutes in one of the input variables at a time according to Table 24. The gas and air flows to a specific hearth are ratio controlled so they are changed together.

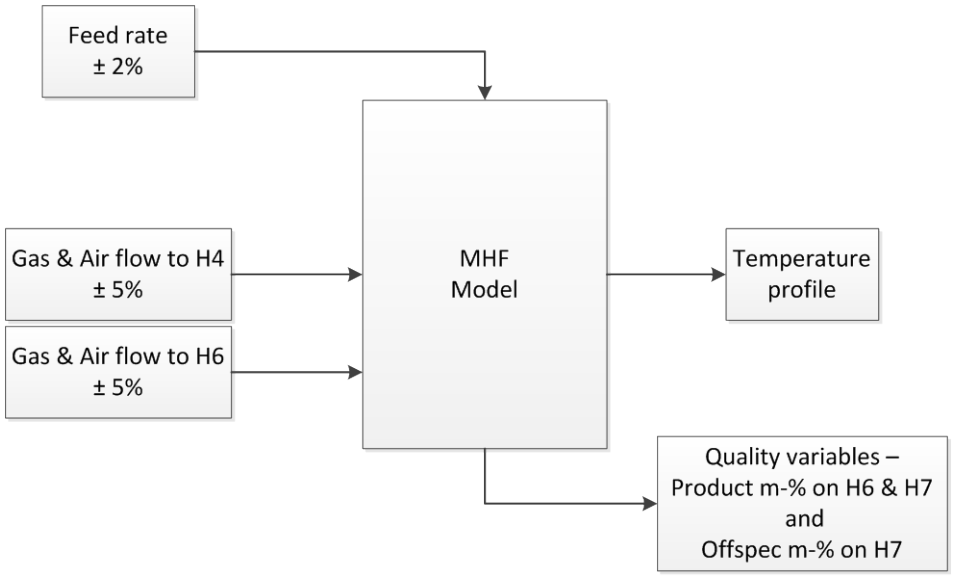

Figure 43. Figure showing the manipulated variables (inputs) of the system on the left and controlled variables (outputs) on the right.

Table 24. Initial values and the sizes of increase and decrease of the input variable for the step tests.

Variable	Initial value	Increase	Decrease
Feed rate	120 kg/min	+2 %	-2 %
Gas flow to the hearth 4	221.5 kg/h	+5 %	-5 %
Air flow to the hearth 4	4203.8 kg/h	+5 %	-5 %
Gas flow to the hearth 6	132.4 kg/h	+5 %	-5 %
Air flow to the hearth 6	2356.9 kg/h	+5 %	-5 %

The first case to study is the model behaviour under an increase in the feed rate, which was 2 percent. The model response can be seen in Figures 44 to 47. Figure 44 presents the temperature profile of the gas phase through the furnace. The gas temperatures of the exhaust and the hearths 2 to 4 decrease after the change in the feed rate and settle to a new steady state temperature. The gas temperatures of the hearths 5 and 6 decrease steadily until 1200 minutes have elapsed when a change in the gas cooling rate can be seen. This change is caused by the reactions occurring in the solid bed as can be seen in Figure 45. The temperature changes on the hearths 7 and 8 at the time of 1200 minutes and 1560 minutes can also be explained by the exothermic spinel formation reaction. The reaction is moved to the lower hearths from the hearth 6 as can be seen in Figures 45 through 47 showing the product content of the solid bed volumes in the hearths 6, 7 and 8 respectively. The increase in the temperature is caused by the spinel formation reaction as it releases energy and the temperature decreases when the spinel formation reaction rate drops on a specific hearth.

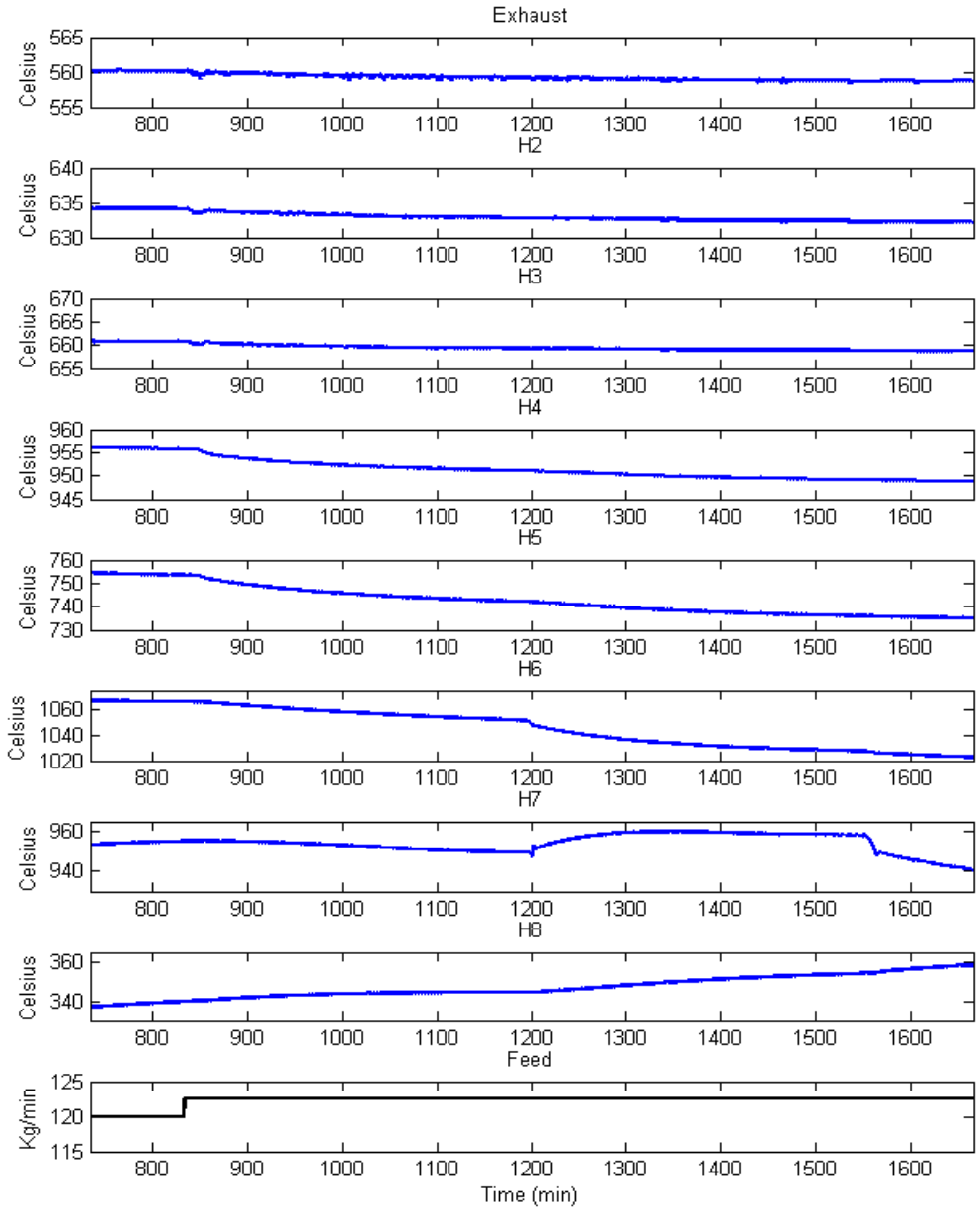

Figure 44. The response of the gas phase temperature next to the wall in the feed rate increase test.

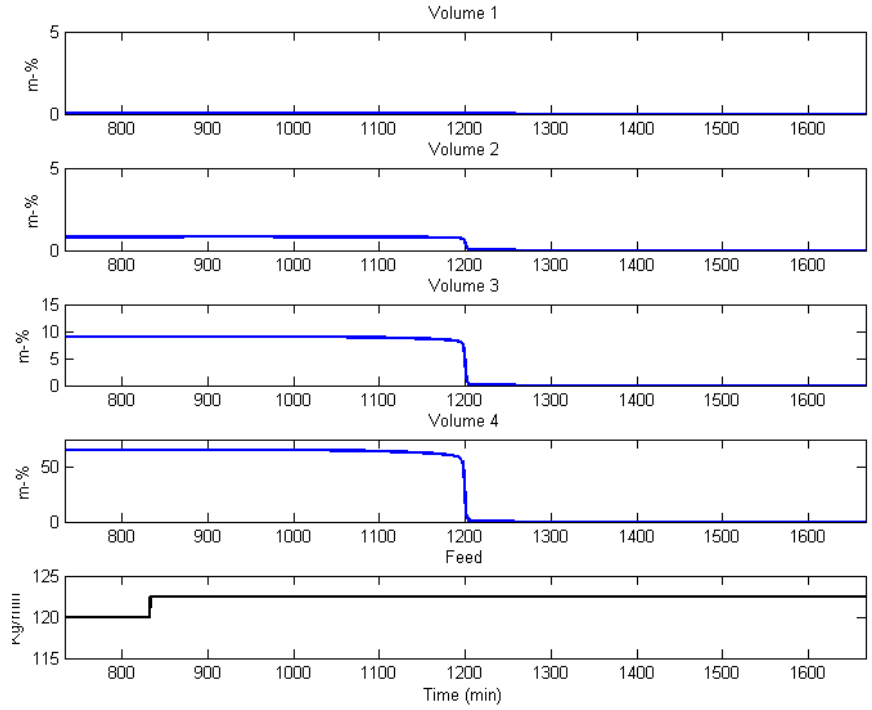

Figure 45. The response of the product content of the solid bed in the hearth 6 during the feed rate increase test.

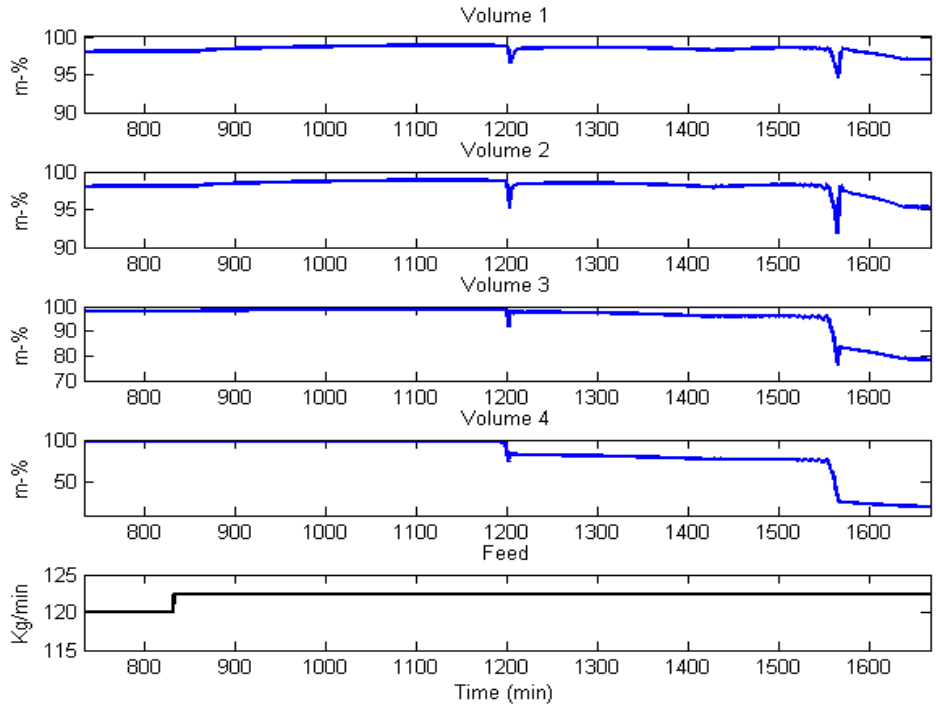

Figure 46. The response of the product content of the solid bed in the hearth 7 during the feed rate increase test.

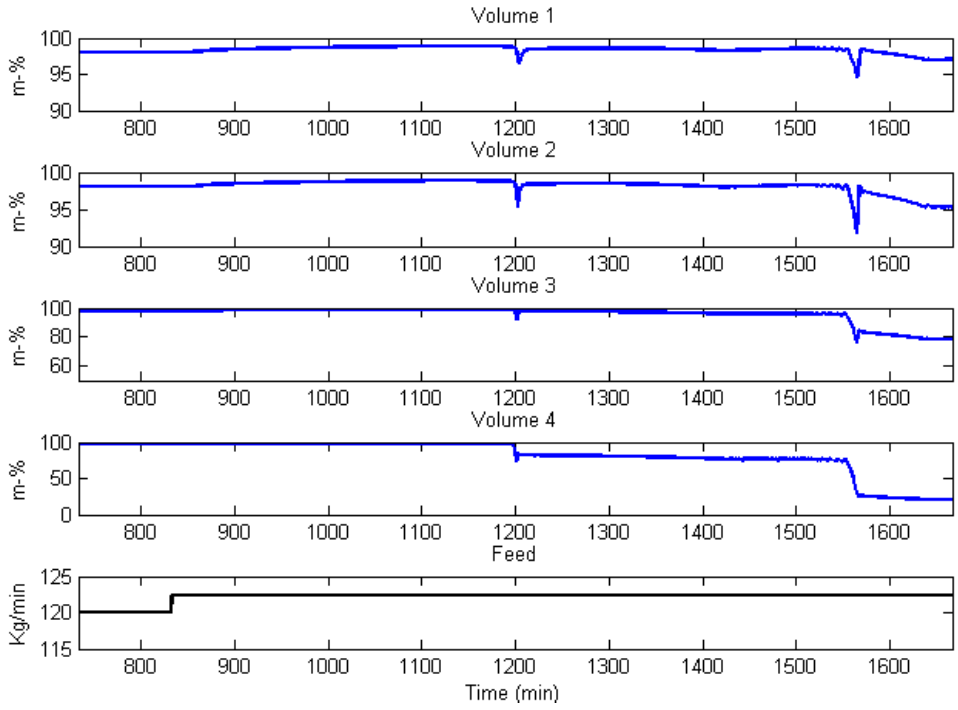

Figure 47. The response of the product content of the solid bed in the hearth 8 during the feed rate increase test.

The second study case is a 2 percent decrease in the feed rate at the time of 833 minutes. The response of the gas temperatures next to the walls can be seen in Figure 48 and the response of the product content of the solid bed in the hearths 6 and 7 is shown in Figure 49 and 50 respectively. The temperatures of the exhaust gas and the gas phases of the hearths 2 and 3 increase only 1 - 2 degrees, after the decrease of the feed rate. The temperatures of the hearths 4, 5 and 6 increase steadily after the decrease in the feed rate, since now more energy is supplied to the furnace than is required. The temperature of the hearth 7 gas phase is unchanged until 1260 minutes when it suddenly decreases. This is caused by the endothermic mullite formation reaction, which consumes energy. Figures 49 and 50 confirm that the spinel phase formation reaction rate increases at the hearth 6 and consequently the mullite formation reaction rate increases at the hearth 7, which can be seen in Figure 50 as a decrease in the product content. The temperature of the hearth 8 is unchanged since the decrease in the feed rate does not cause the reaction to reach the hearth.

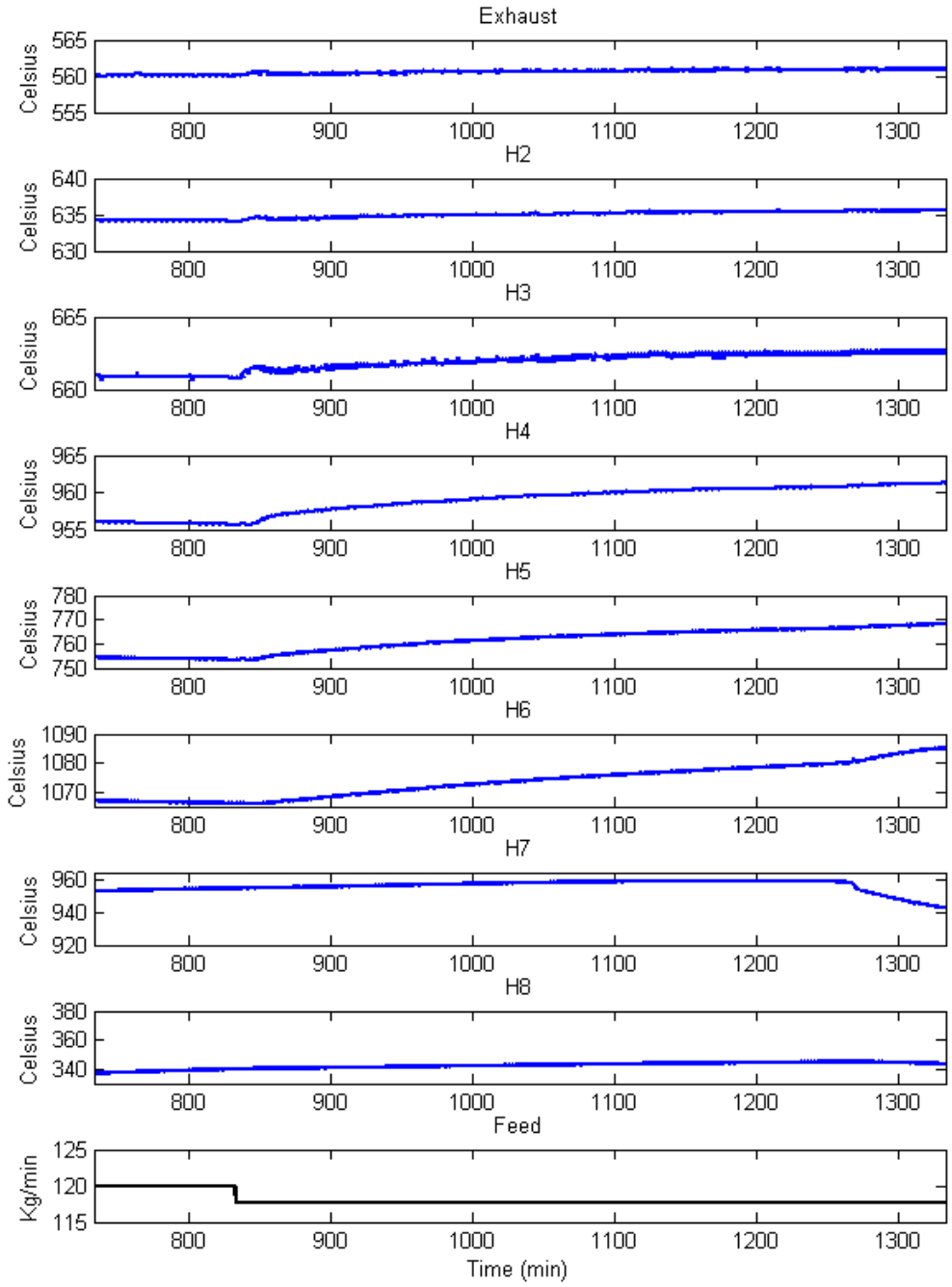

Figure 48. The response of the gas phase temperature next to the wall in the feed rate decrease test.

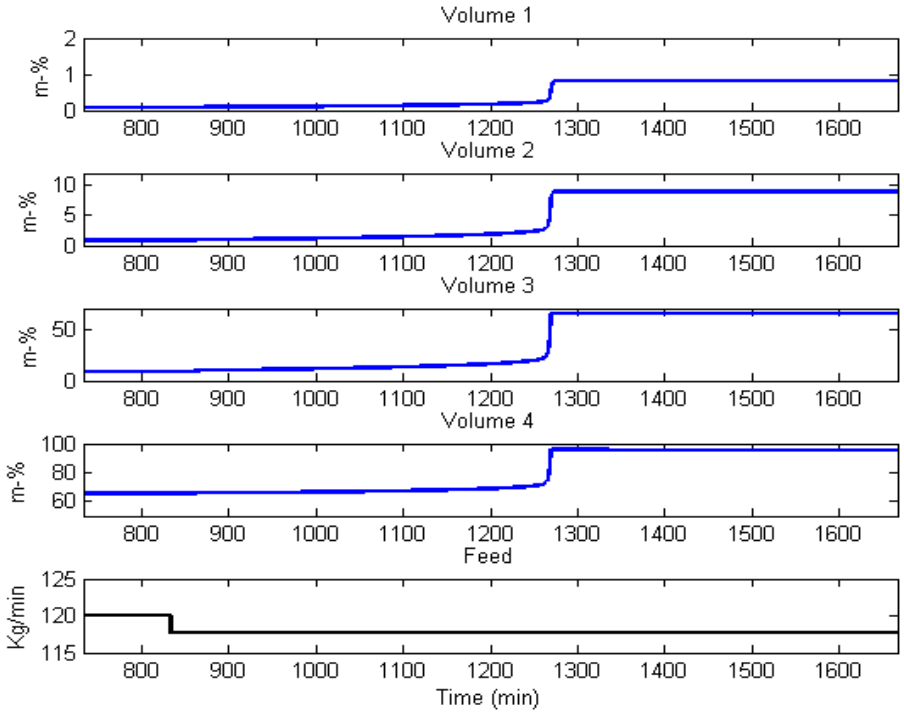

Figure 49. The response of the product content of the solid bed in the hearth 6 during the feed rate decrease test.

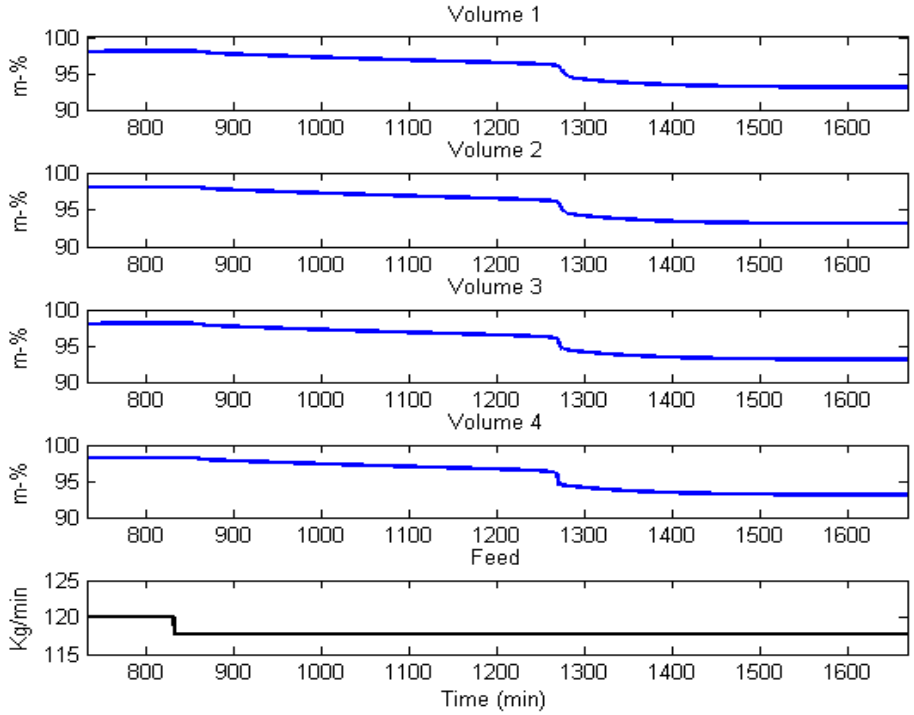

Figure 50. The response of the product content of the solid bed in the hearth 7 during the feed rate decrease test.

The third test case studies the model response to a 5 percent increase in the gas and air flows to the hearth 4. Figure 51 shows the response of the gas phase temperatures next to the wall and Figure 52 and 53 present the changes in the solid bed product content in the hearth 6 and 7 respectively. The exhaust gas temperature and the temperatures of the hearths 2 to 4 increase instantly after the step change and afterwards they reach a higher steady state as the initial temperature was. The gas temperatures of the hearths 5 and 6 increase also, but they increase steadily until they have reached a new steady state at the time of 1400 minutes. The small interruption during the increase of the hearth 6 temperature is caused by the increased spinel phase formation reaction rate, which can be seen in Figure 52. The temperature of the hearth 7 gas phase increases little until it drops at 1180 minutes. The drop of the temperature in the hearth 7 is caused by the increased reaction rate of the endothermic mullite formation reaction, which can be seen in Figure 53 as a decrease in the product content. The first increasing and then decreasing temperature of the hearth 8 gas temperature is also explained by the phenomenon occurring in the hearth 7 as first the solid bed temperature is rising, but after the endothermic mullite formation reaction begins, it starts cooling the solid bed, which can no more release as much energy to the gas phase as previously.

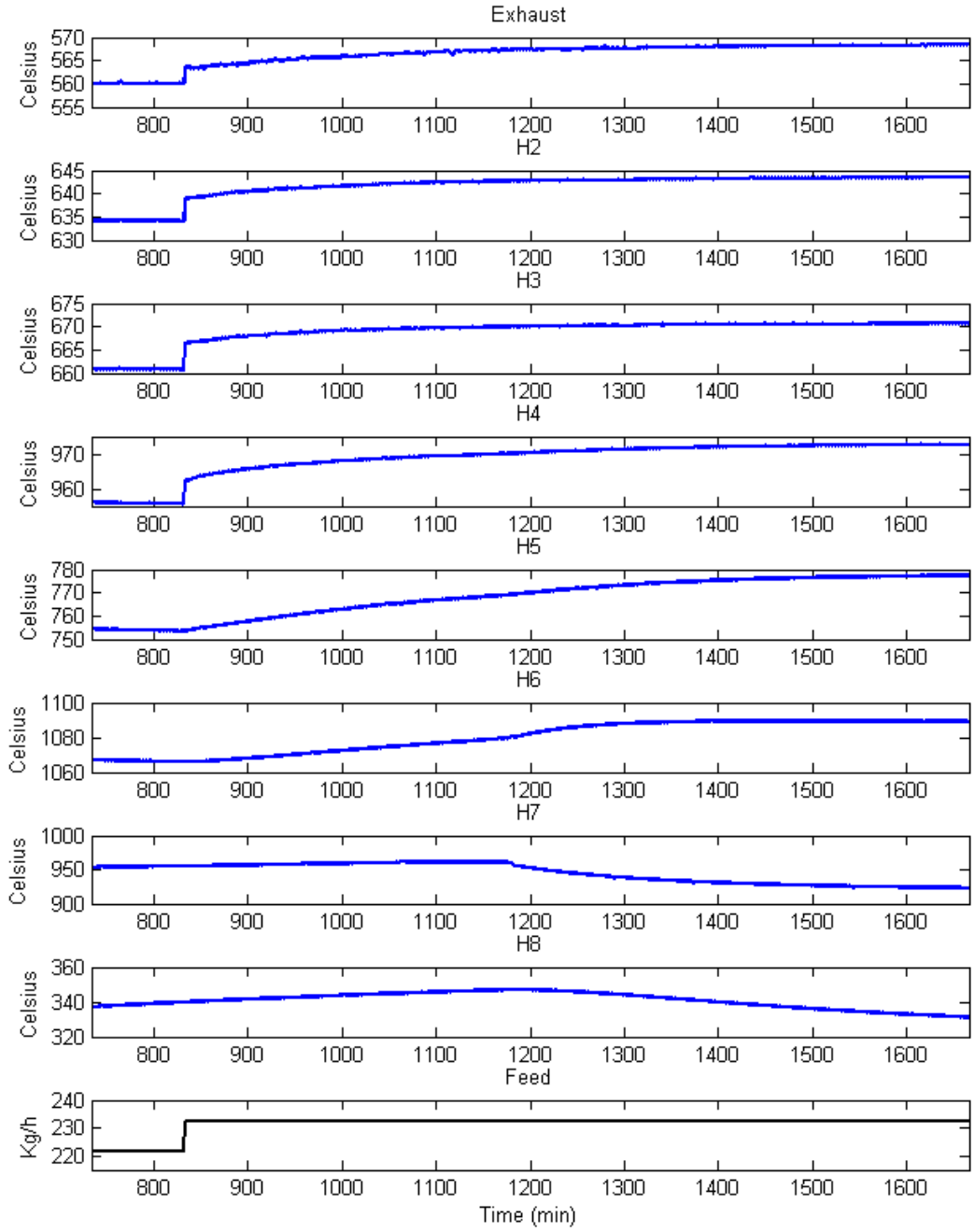

Figure 51. The response of the gas phase temperature next to the wall while increasing the gas and air flows to the hearth 4.

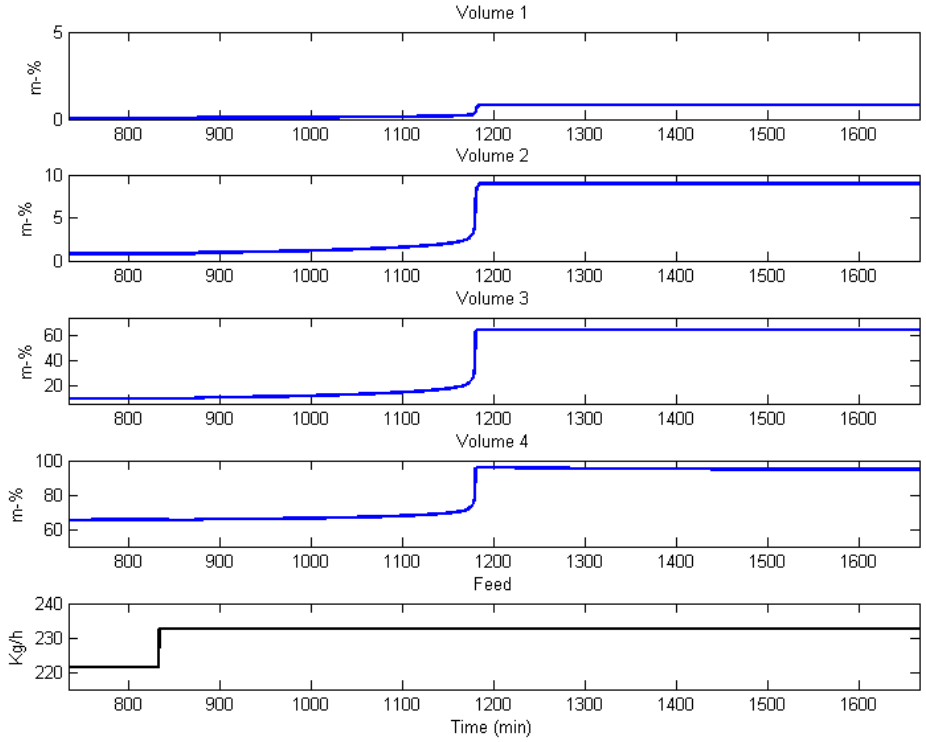

Figure 52. The response of the hearth 6 product content while increasing the gas and air flows to the hearth 4.

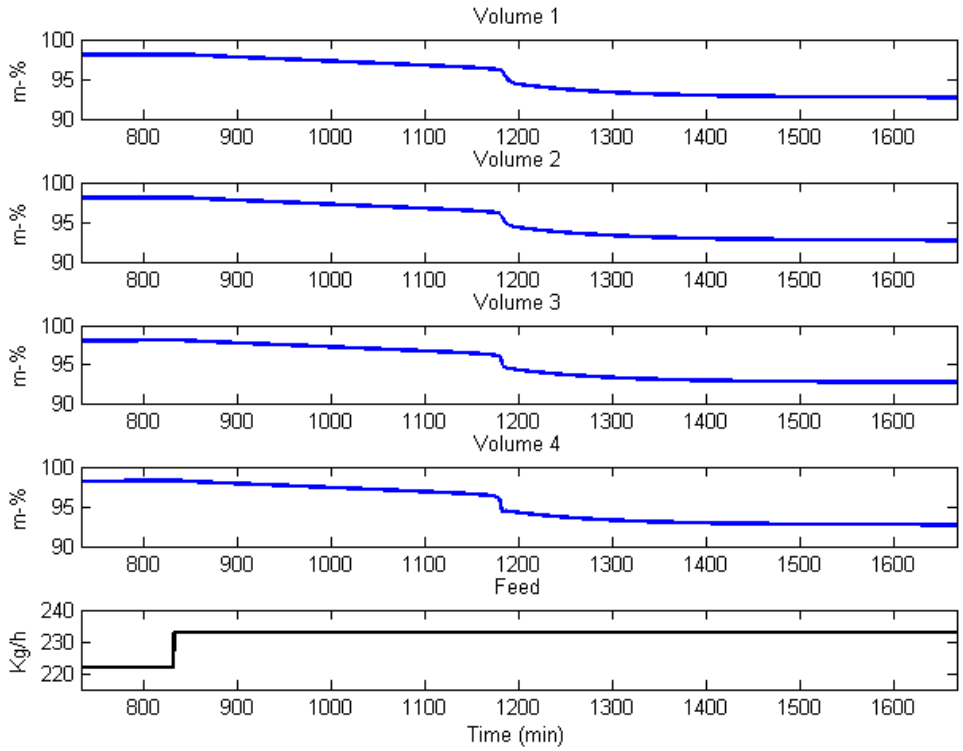

Figure 53. The response of the hearth 7 product content while increasing the gas and air flows to the hearth 4.

The fourth study case presents the model response to a decrease in the gas and air flows to the hearth 4. Figure 54 shows the response of the gas phase temperatures next to the wall and Figure 55 and 56 present the changes in the solid bed product content in the hearth 6 and 7 respectively, and Figure 57 shown the changes in the mullite content of the hearth 7 solid bed. As the gas and air flow to the hearth 4 decrease, the temperatures of the exhaust gas and the hearths 2, 3 and 4 decrease first with a steep step and then they steadily decrease reaching a steady state. The temperature of the hearth 5 decreases steadily for the whole recorded time period. The temperature of the hearth 6 gas phase decreases after the step change, but the decrease is not steady through the whole time span recorded, but the decreasing speed is affected at times of 1120 minutes and 1420 minutes. The first interruption is caused by the change in the spinel phase formation reaction rate and the second interruption is caused by the decreased temperature of the incoming gas from the hearth 7. The temperature of the gas phase in the hearth 7 stays constant until 1420 minutes when the reaction rate of the spinel phase formation reaction collapses and the reaction no more releases energy as seen in Figure 56, now the solid bed on hearth 7 is consists only of metakaolin. The temperature of the gas phase of the hearth 8 also stays almost constant until 1450 minutes when the temperature decreases caused by the change in the solid bed reactions, which can be seen from Figures 56 and 57, where the solid bed on the hearth 7 consists only of metakaolin that is also true also for the hearth 8 since there is not enough energy to heat the solid bed up to the temperature of 925 °C required for the spinel formation reaction to occur. Consequently, the output from the furnace is only metakaolin.

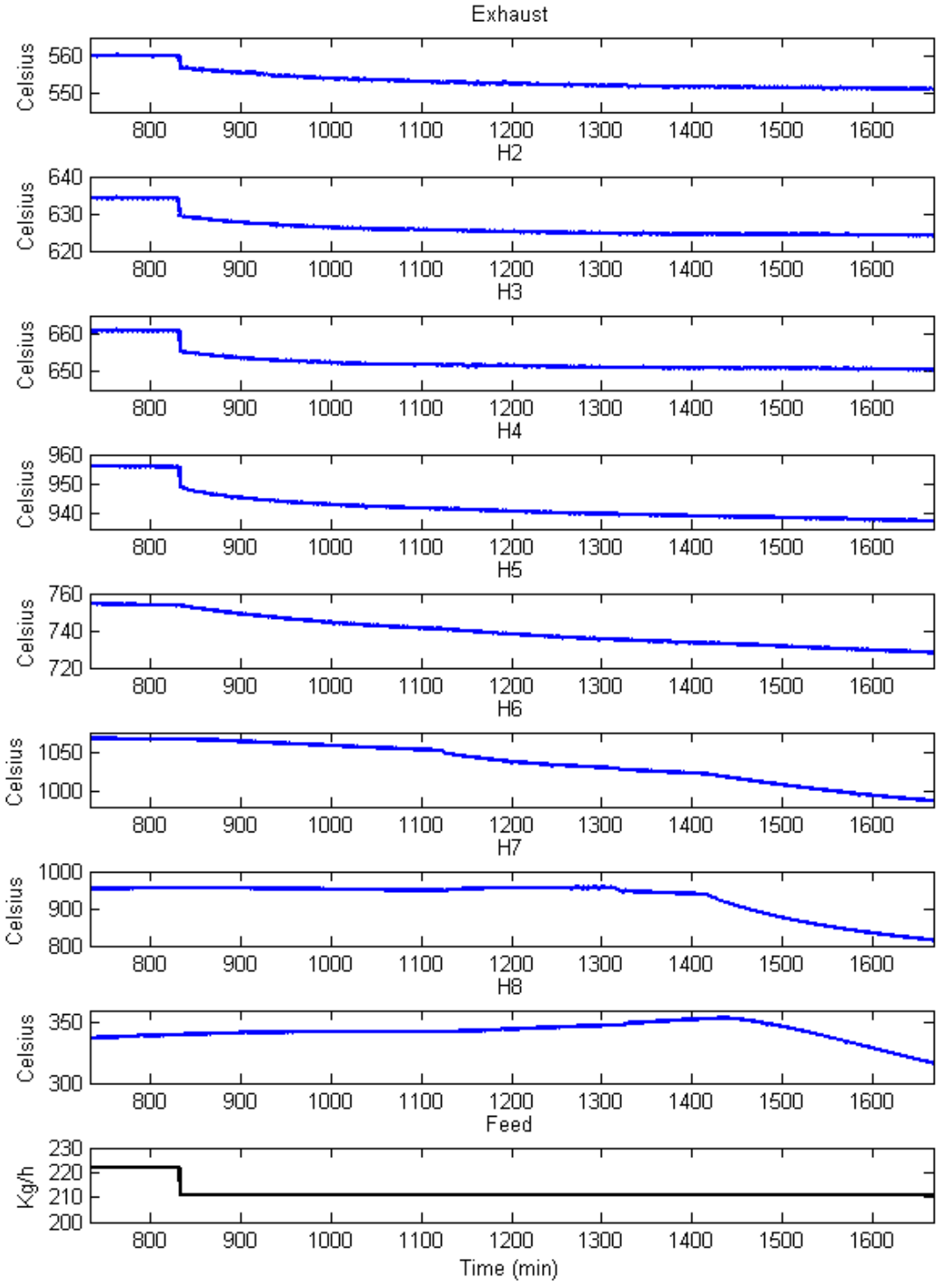

Figure 54. The response of the gas phase temperature next to the wall while decreasing the gas and air flows to the hearth 4.

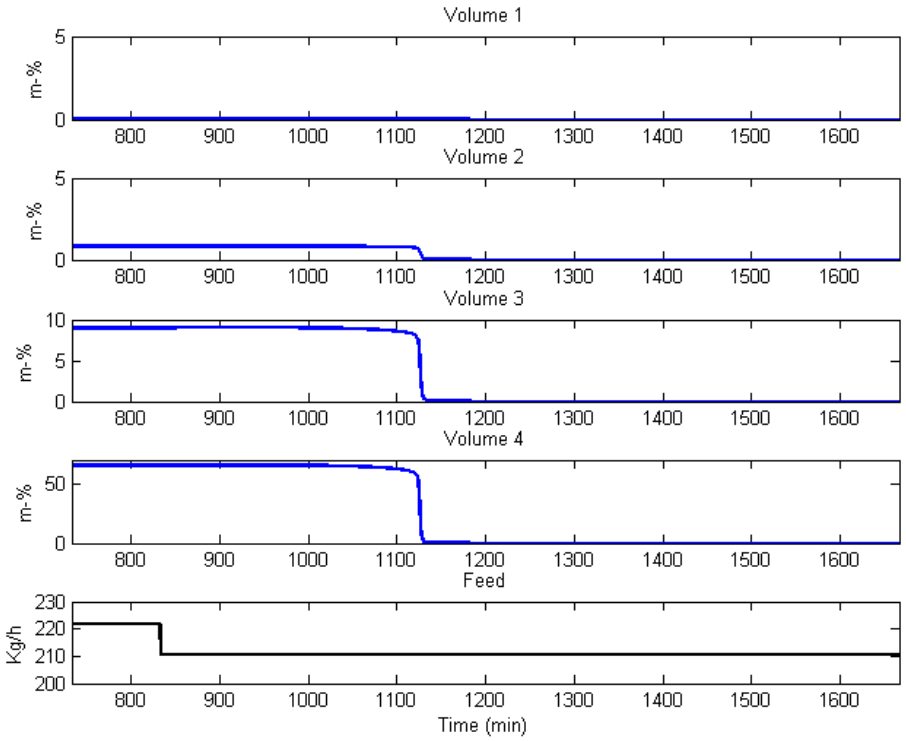

Figure 55. The response of the hearth 6 product content while decreasing the gas and air flows to the hearth 4.

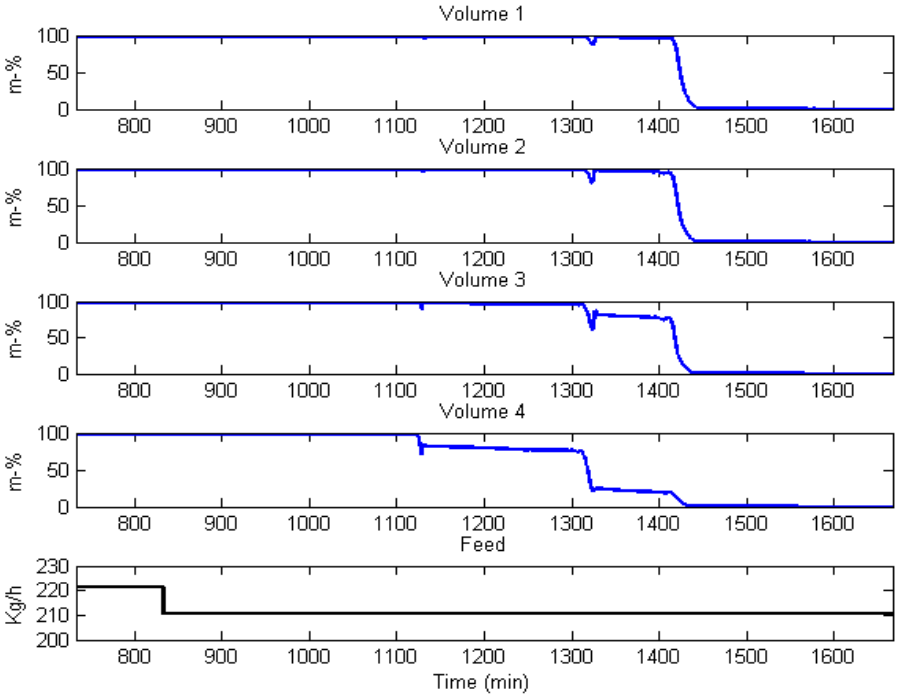

Figure 56. The response of the hearth 7 product content while decreasing the gas and air flows to the hearth 4.

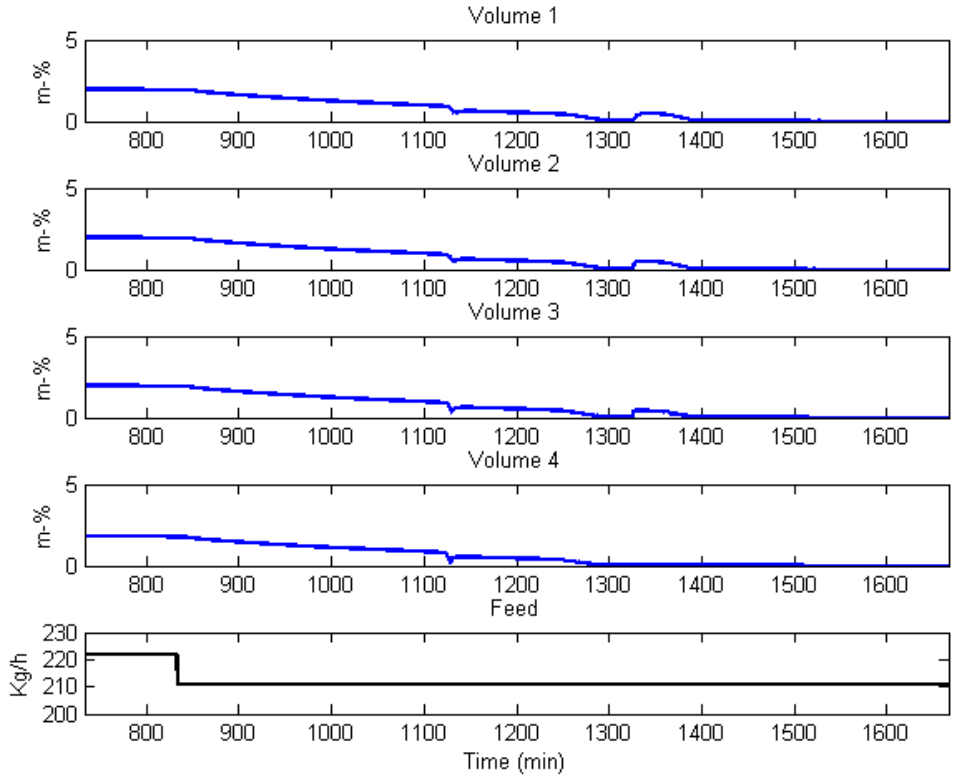

Figure 57. The response of the hearth 7 offspec content while decreasing the gas and air flows to the hearth 4.

The fifth study case investigates the response of the system to a increase in the gas and air flows to the hearth 6. Figure 58 shows the response of the gas phase temperatures next to the wall and Figure 59 and 60 present the changes in the solid bed product content in the hearth 6 and 7, respectively. While increasing the gas and air flows to the hearth 6, the temperatures of the exhaust gas and of the gas phases on the hearths 2 and 3 experience a step-like increase and then settle to a new steady state temperature. The temperature of the hearth 4 first drops by one degree and then it rises stedily to a new steady state temperature. The temperature of the hearth 5 first experiences similar step-like increase as the exhaust and the hearths 2 and 3, but afterwards it continues to rise to a new steady state temperature. Also, the temperatures of the gas phases of the hearths 6, 7 and 8 increase steadily as seen in figure 58. The product content of the solid bed in the hearth 6 rises a little as seen in Figure 59 and furthermore the increased amount of

energy in the furnace allows the mullite formation reaction rate to increase, which can be seen in Figure 60 as a decrease in the product share in the solid bed in the hearth 7.

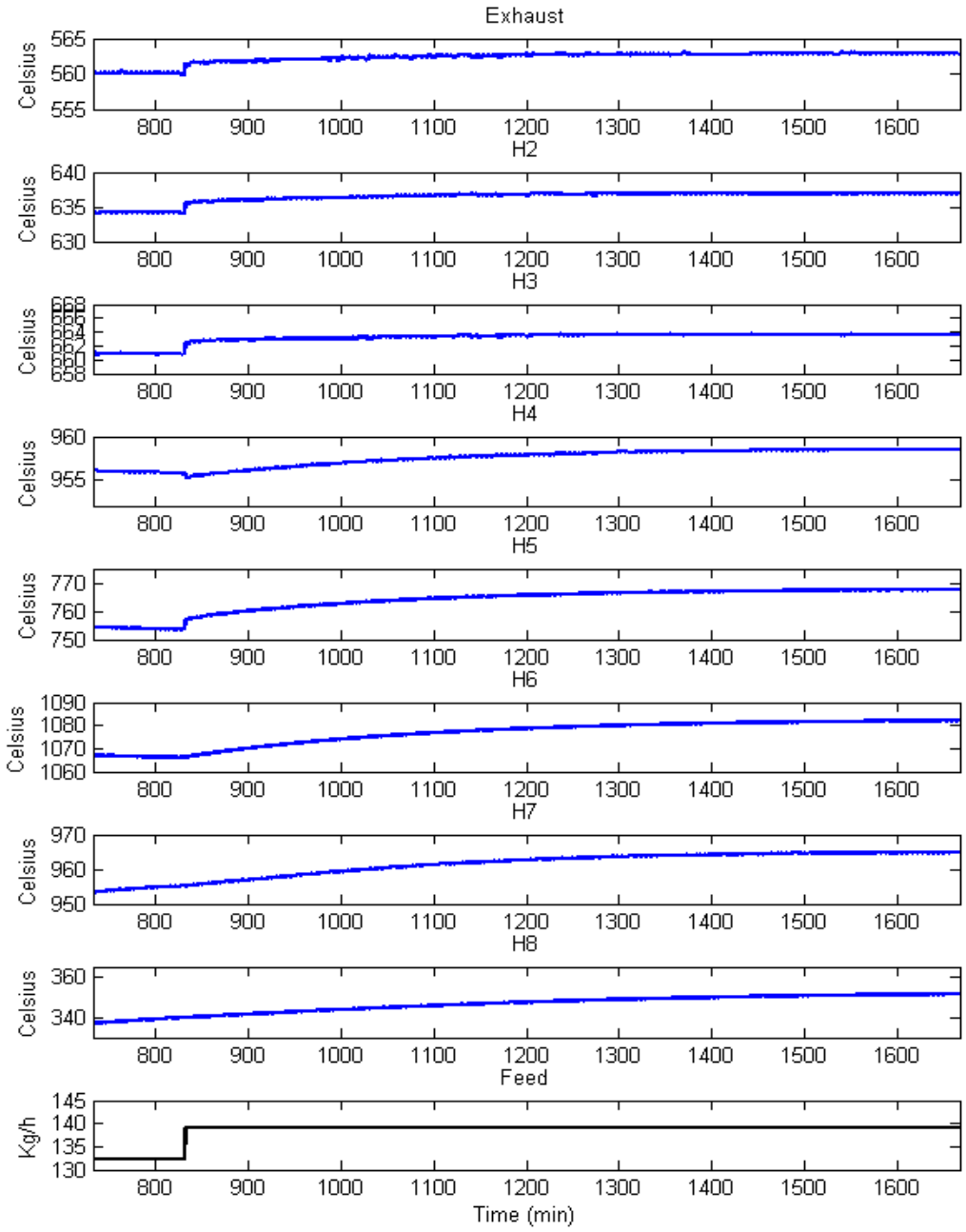

Figure 58. The response of the gas phase temperature next to the wall while increasing the gas and air flows to the hearth 6.

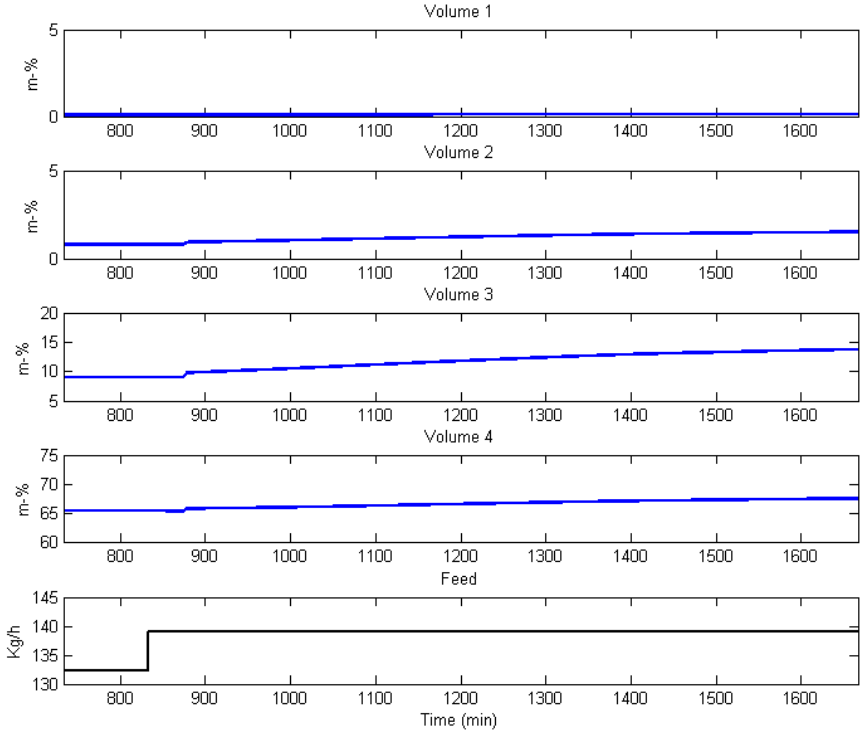

Figure 59. The response of the hearth 6 product content while increasing the gas and air flows to the hearth 6.

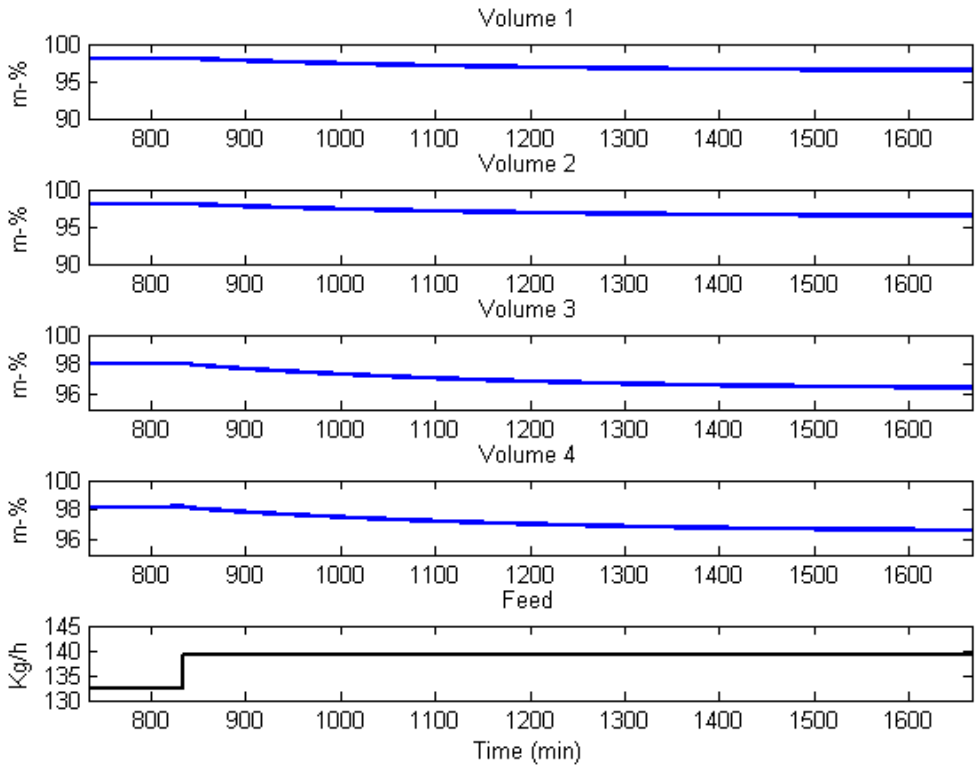

Figure 60. The response of the hearth 7 product content while increasing the gas and air flows to the hearth 6.

The last of the step response tests for individual input variables studies the effect of decrease in the gas and air flows to the hearth 6. Figure 61 shows the response of the gas phase temperatures next to the wall and Figure 62 and 63 present the changes in the solid bed product content in the hearth 6 and 7, respectively, and Figure 64 present the amount of offspec in the solid bed in the hearth 7. The responses of the temperatures of the exhaust gas and the gas phases of the hearths 2 to 5 are exactly the opposite of the previous case where the gas and air flows were increased and the temperatures decrease. The temperature of the hearth 6 starts decreasing slowly reaching a steady state at the time of 1500 minutes after the step change, but then at the time of 1540 minutes the temperature of the gas drops 20 degrees. This drop is caused by the drop in the reaction rate of the spinel formation reaction, which can be seen in Figure 62. After the step in the gas and air flows the temperature of the hearth 7 gas phase decreases steadily until reaching steady state at 1500 minutes, however the temperature increases suddenly after 1540 minutes as the spinel formation reaction is moved to occur at the hearth 7 as can be seen in Figure 63. The drop in the mullite content of the solid bed in the hearth 7 seen in Figure 64 confirms that the spinel phase reaction is occurring now in the hearth 7.

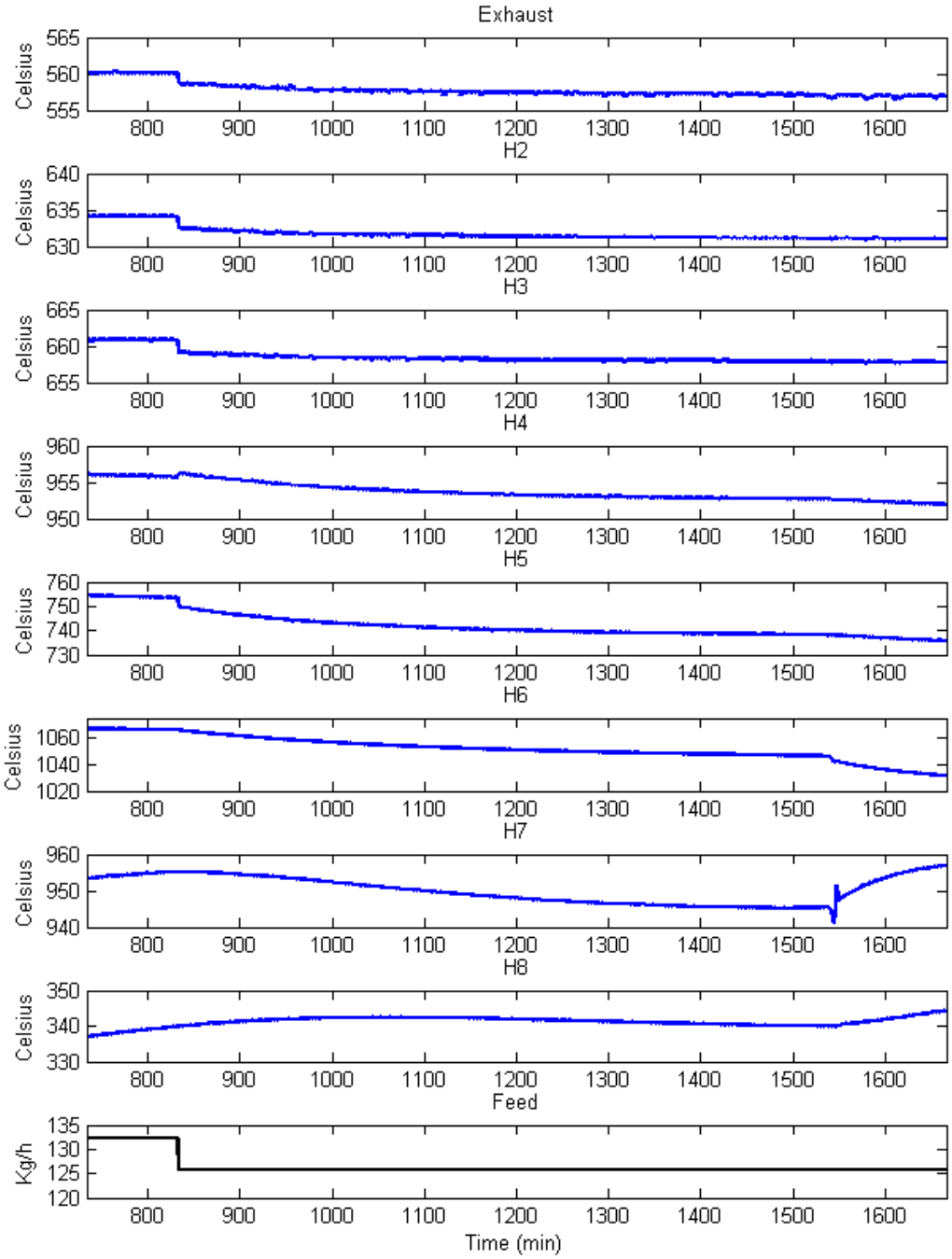

Figure 61. The response of the gas phase temperature next to the wall while decreasing the gas and air flows to the hearth 6.

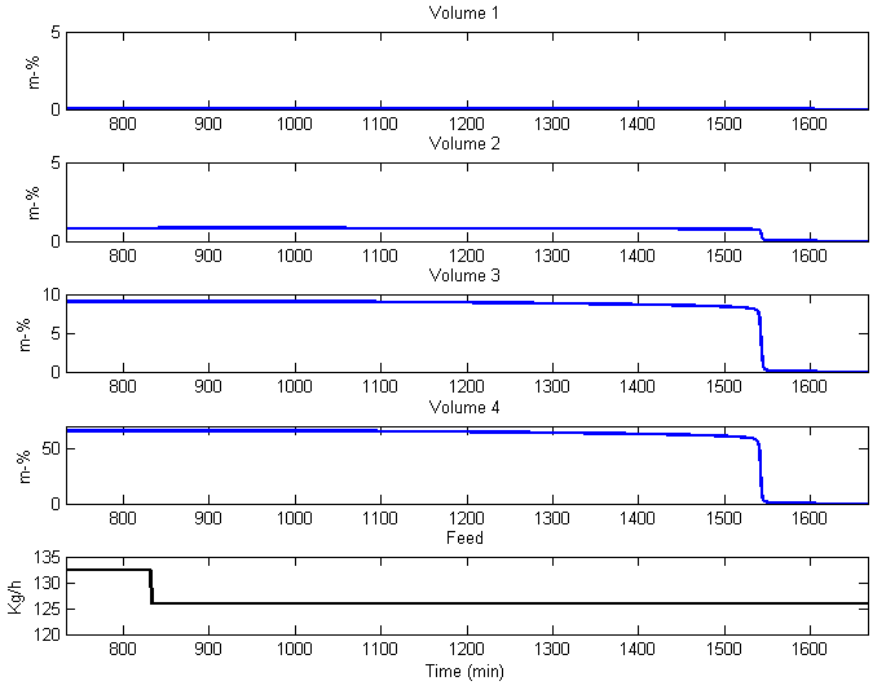

Figure 62. The response of the hearth 6 product content while decreasing the gas and air flows to the hearth 6.

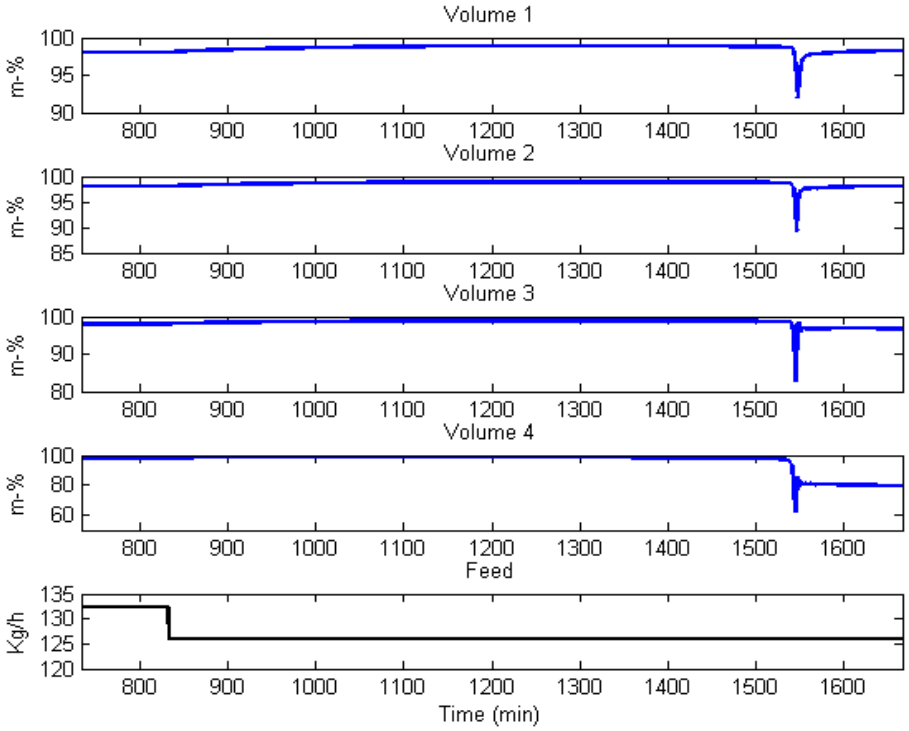

Figure 63. The response of the hearth 7 product content while decreasing the gas and air flows to the hearth 6.

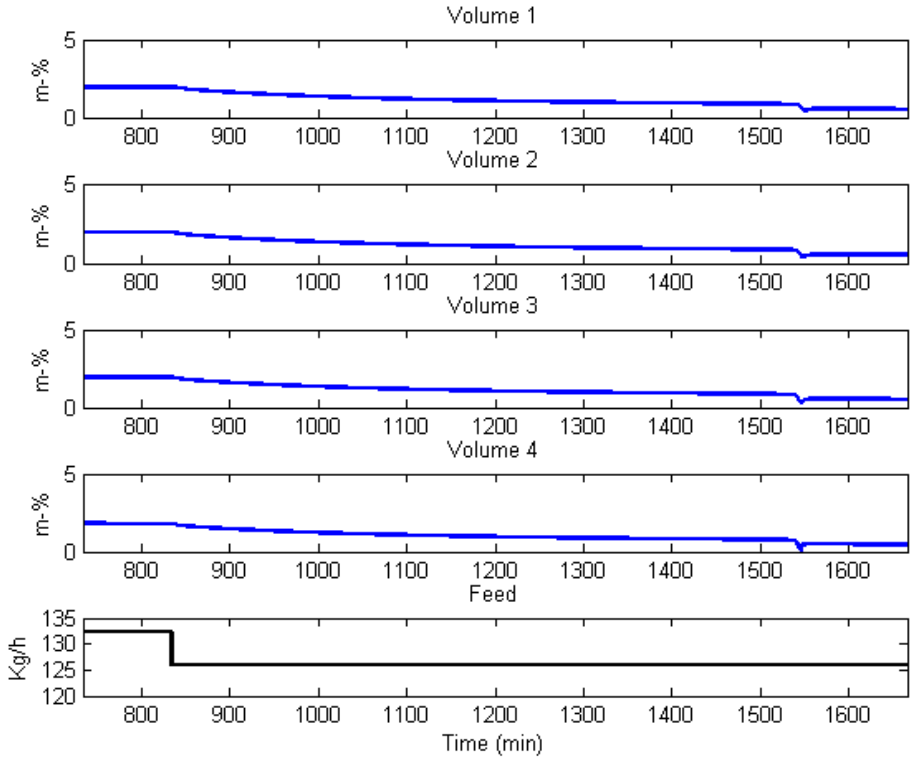

Figure 64. The response of the hearth 7 offspec content while decreasing the gas and air flows to the hearth 6.

As a conclusion for the individual step tests for each input variable, the model responses can be said to be reasonable. The gas phase temperatures show fast responses to the changes in the gas and air flows, which confirm the assumption of fast dynamics in the gas phase, however if the temperature of the gas phase is mainly affected by the changes in the solid bed temperatures it can take considerably longer time for the temperature to reach a new steady state. When considering the changes in the solid bed the first response can be seen almost immediately after the change in the input variables, however in some cases the more significant responses can be noticed after much longer time, even 700 minutes, which denotes the ability of the solid bed itself and the walls and the hearth roofs and bottoms to reserve heat slowing down the energy dynamics of the solid bed.

Additionally, the dynamic behaviour of the MHF model was tested with a step increase and a decrease in the feed rate and in the gas and air flows to the hearths 4 and 6 simultaneously at the time of 833.3 minutes. The results for the increase step test are presented in Figures 65 and 66, and the results for the decrease step are presented in Figures 67, 68 and 69.

The temperature profile for the gas phase volumes next to the wall are shown in Figure 65, where the bottom curve presents the step change in the feed rate. After the step down in the five input variables the temperatures of the exhaust and hearths 2 to 4 increase and stabilize quickly, however the increase of the temperature is less than ten degrees. Interestingly, the temperatures of the hearths 5 and 6 first increase and then decrease over a period of time to a lower temperature than the temperature before the step. The first noticed increase of the temperatures occurs because of the feed rate and the gas and air flows are changed simultaneously. Consequently, the instantly increased gas flow increases the temperature of the gas phase but the amount of the solid material is still the same as it was before the step change since there exists a small delay before the increased feed rate affects the amount of the solids on the hearths 5 and 6. The same phenomenon is also noticed in the exhaust temperature and in the temperatures of the hearths 2, 3 and 4. Moreover, the temperatures of the gas phases of the hearths 7 and 8 increase since the temperature of the solid bed increases and it releases more heat to the gas phase, while simultaneously the air flow through the bottom drop holes stays constant. It is also noticeable that the temperatures of the exhaust and the gas phases in the hearths 2 to 4 stabilize faster than the temperatures of the gas phases on the bottom four hearths.

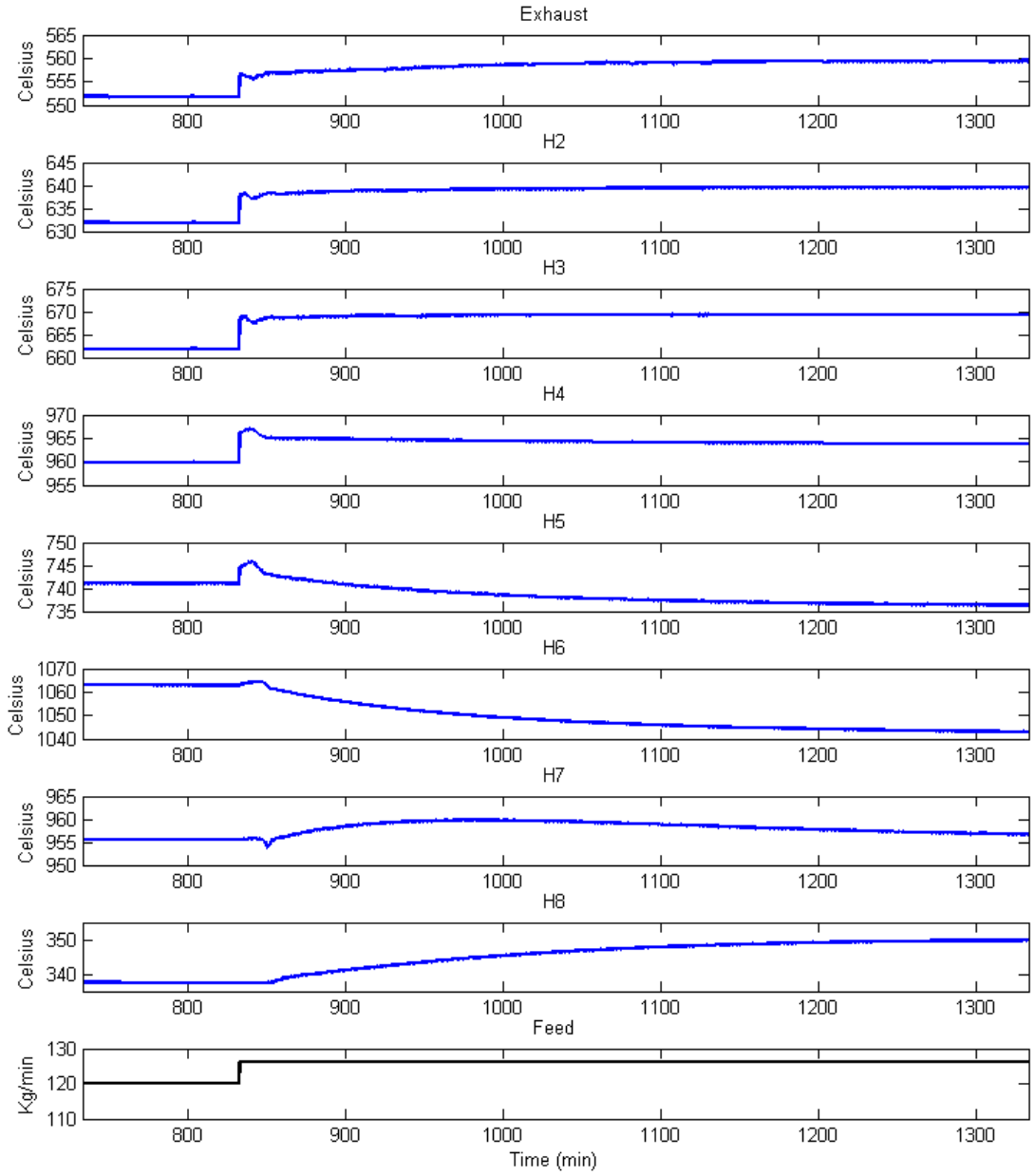

Figure 65. The responses of the gas phase temperatures next to the wall to the step up test.

Figure 66 shows the product content of the solid bed in the volumes 3 and 4 of the hearths 6 and 7. First, after the step change, the product content of the volume three in the hearth 6 raises a bit, but shortly after the delay in the solid bed movement the product content decreases almost to zero. The same decrease behaviour takes place in the volume 4 of the hearths 6 and 7 meaning that the

amount of energy supplied to the furnace is not enough to keep the product formation reaction occurring with required intensity on the hearth 6, but the reaction takes place later in the furnace. Also, from this type of behaviour it is evident that the ratio of the feed rate and the required supplied heat is not the same with different feed rates. However, from the product content curve of the volume 3 in the hearth 7, it is noticeable that actually the final product content increases and the mullite content decreases. This happens because the temperature of the solid bed in the hearth 7 is cooled down by the cooler gas phase than on the hearth 6 and so the temperature of the solid bed is not high enough for the mullite formation reaction to take place and the reaction does not have the excess energy it requires.

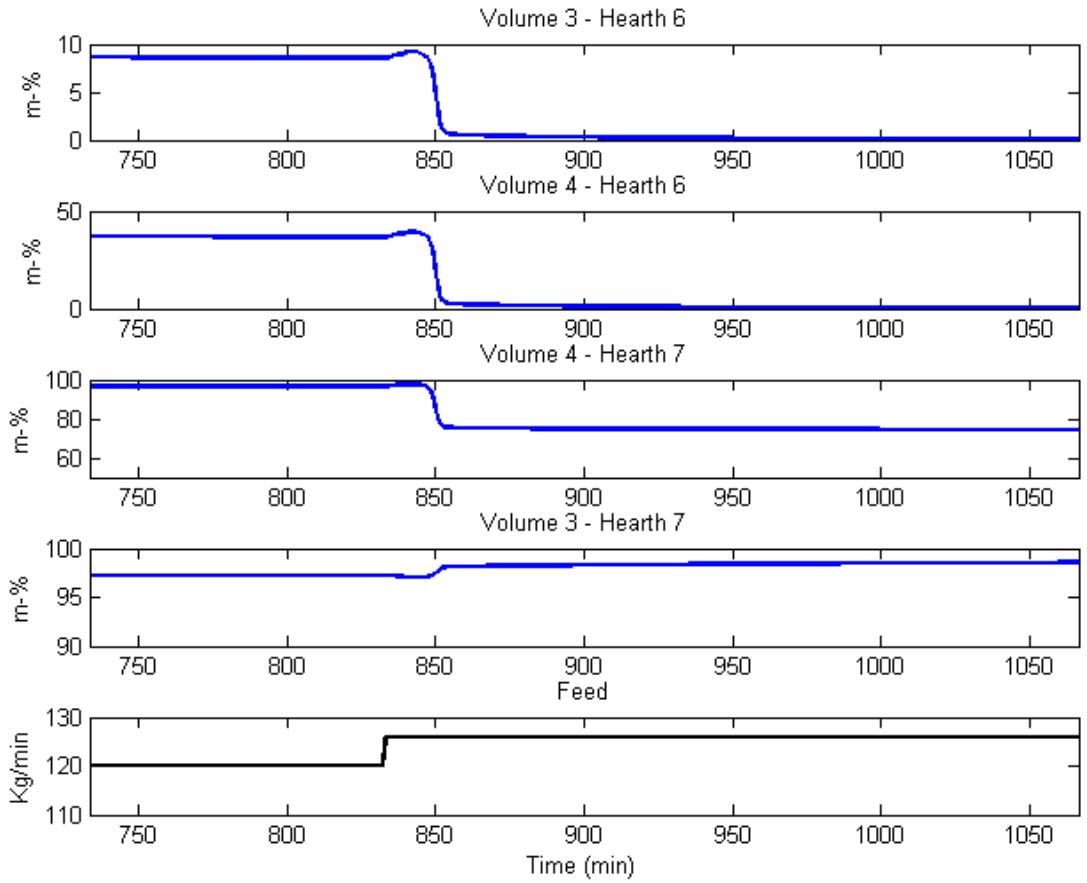

Figure 66. The response of the solid bed product content in volumes 3 and 4 in hearths 6 and 7 to the step up experiment.

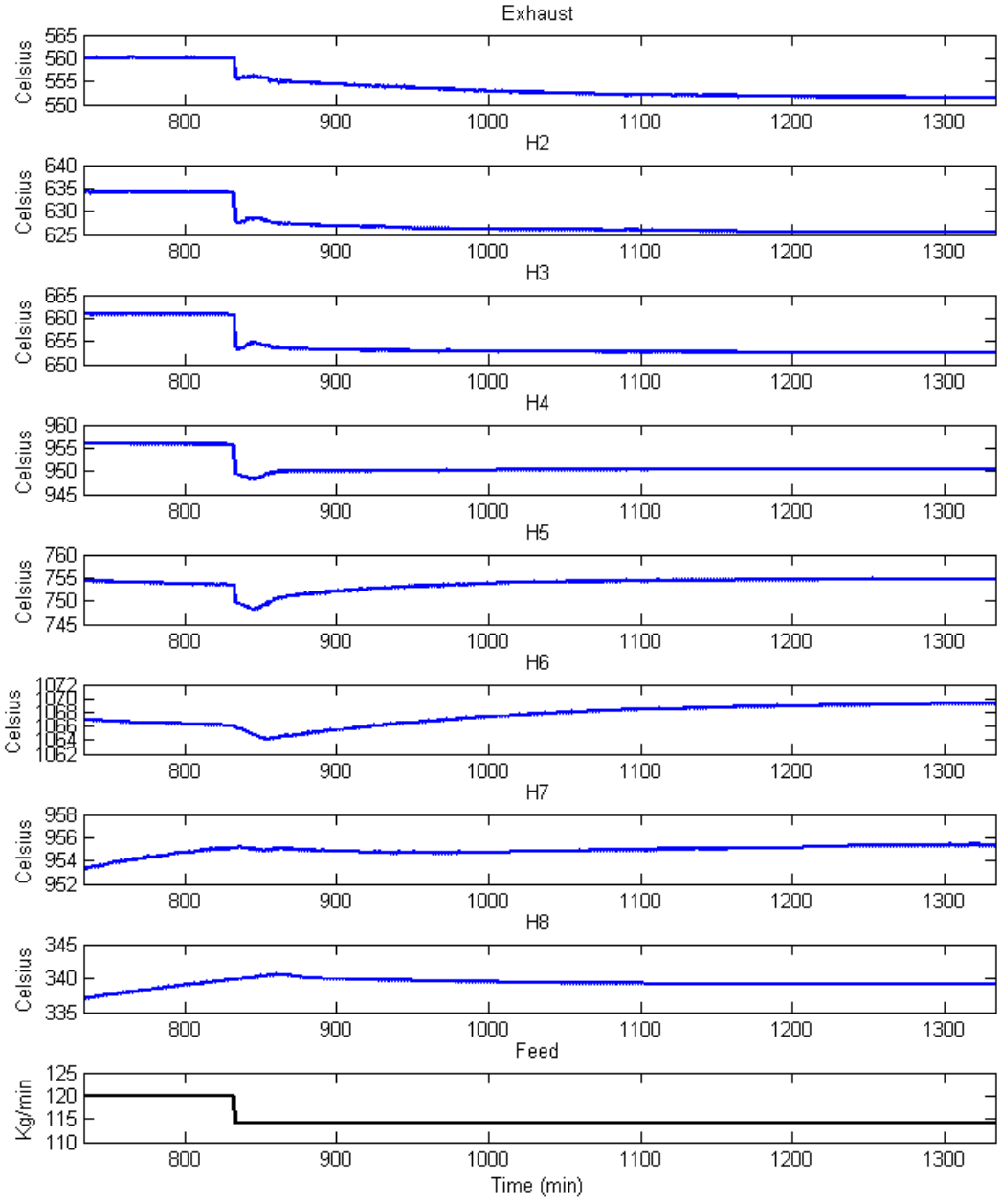

Figure 67. The response recorded in the gas phase temperature next to the wall in the step down test.

Figure 67 presents the temperatures of the gas phase volumes next to the wall during the step down test. Opposite to the step up test, the temperatures of the exhaust gases and the gas in hearths 2 to 5 decrease instantly. Afterwards, the temperatures raise a little and afterwards they settle to lower temperatures than the starting temperatures were except the temperature of the hearth 5. The small

increase step is caused by the same delay in the solid movement as was in previous case. The gas temperatures in the hearths 5 and 6 tend to increase over the time, but eventually they do reach a stable state. The temperatures of the hearths 7 and 8 stay constant during the test.

Figures 68 and 69 present the solid bed product contents in the hearths 6 and 7 respectively during the step down test. The solid bed composition in the hearth 6 stays almost constant during the step test, only a small increase can be seen in the product level of the volume 3.

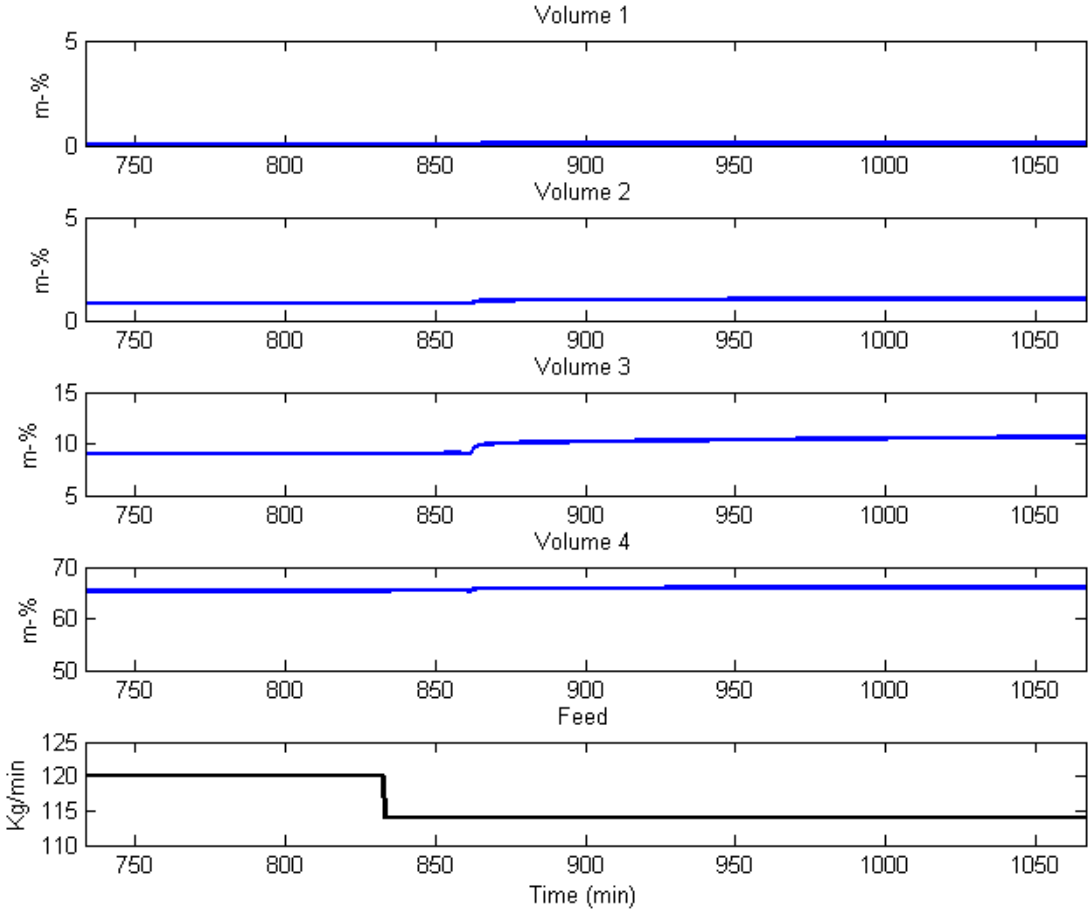

Figure 68. The response of the solid bed product content in the hearth 6 during the step down test.

Figure 69 shows that the solid bed product content has reached its highest level already in the volume 4 in the hearth 7. The solid bed product content in the hearth 7 stays almost constant during the test, only a small effect can be seen after the step change.

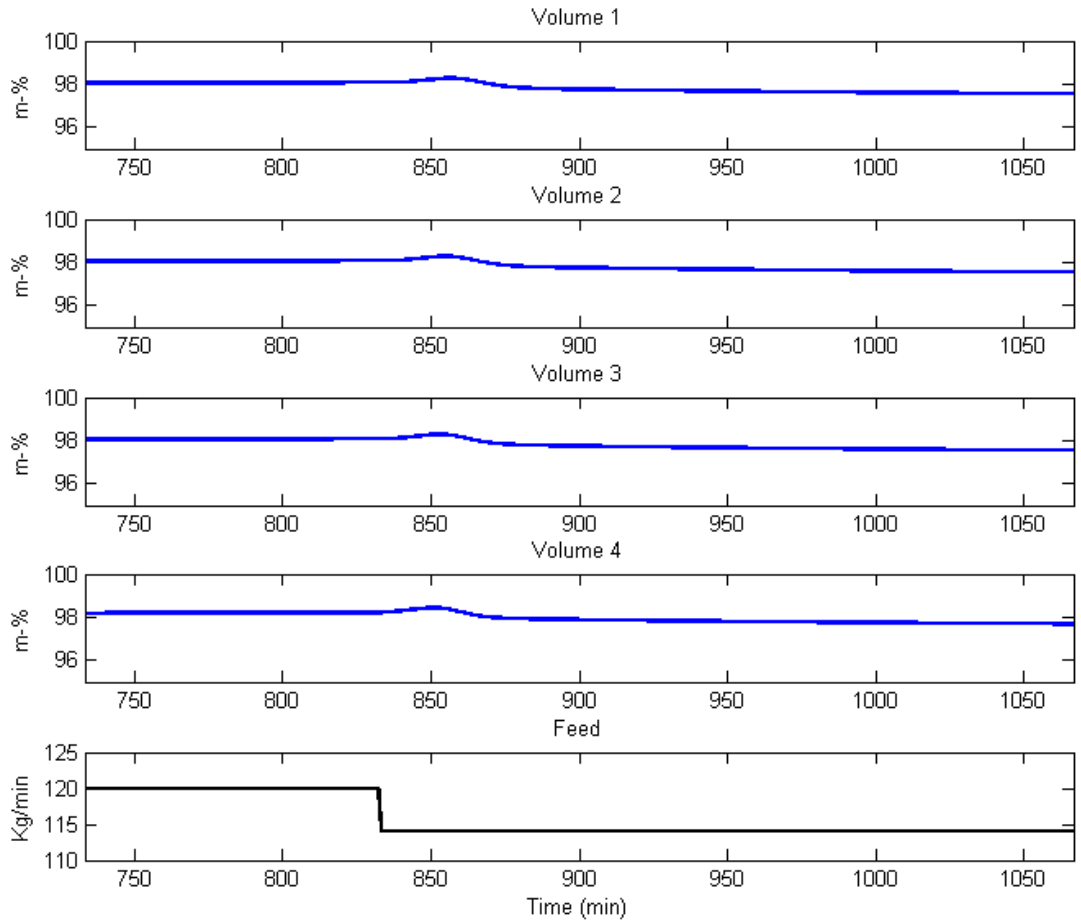

Figure 69. The response of the solid bed product content in the hearth 7 during the step down test.

As a conclusion, the input variables; the feed rate and the gas and air feeds to the hearths 4 and 6, should not be changed simultaneously in normal operation, but a small delay should be introduced to the gas and air feeds to ensure constant operation conditions inside the furnace and to obtain steady end product. In addition, as demonstrated by these step tests, the amount of supplied gas should

be optimized to achieve the maximum product content and the minimum mullite content as possible in the end product.

11.3.2. Studying the dynamic behaviour of the MHF model with industrial data

In this chapter the dynamic behaviour of the MHF model is studied utilizing the real industrial data in the simulator. It is noticeable that under normal operation the MHF furnace is under control and the process is run in a closed-loop, which may cause difference between the industrial data and the model behaviour.

The dynamic behaviour of the model utilizing industrial data was studied in three different cases:

1) Test the model performance with a feed rate of 110 kg/h.
2) Test how the model responses to an increase in the feed rate.
3) Test how the model responses to a decrease in the feed rate.

The first test case is performed to confirm if the model parameters, which were fitted for the feed rate of 120 kg/min, are also applicable with other process conditions. Data from the period of May 2013, when the feed rate was 110 kg/min, was chosen for this case study. Figure 70 shows the behaviour of the model at the hearths 5 and 6 when the feed rate is 110 kg/min. The graph shows that the model follows the measured data relatively well. The temperature difference of 150 °C on the hearth five is the same as was noticed with the steady-state model.

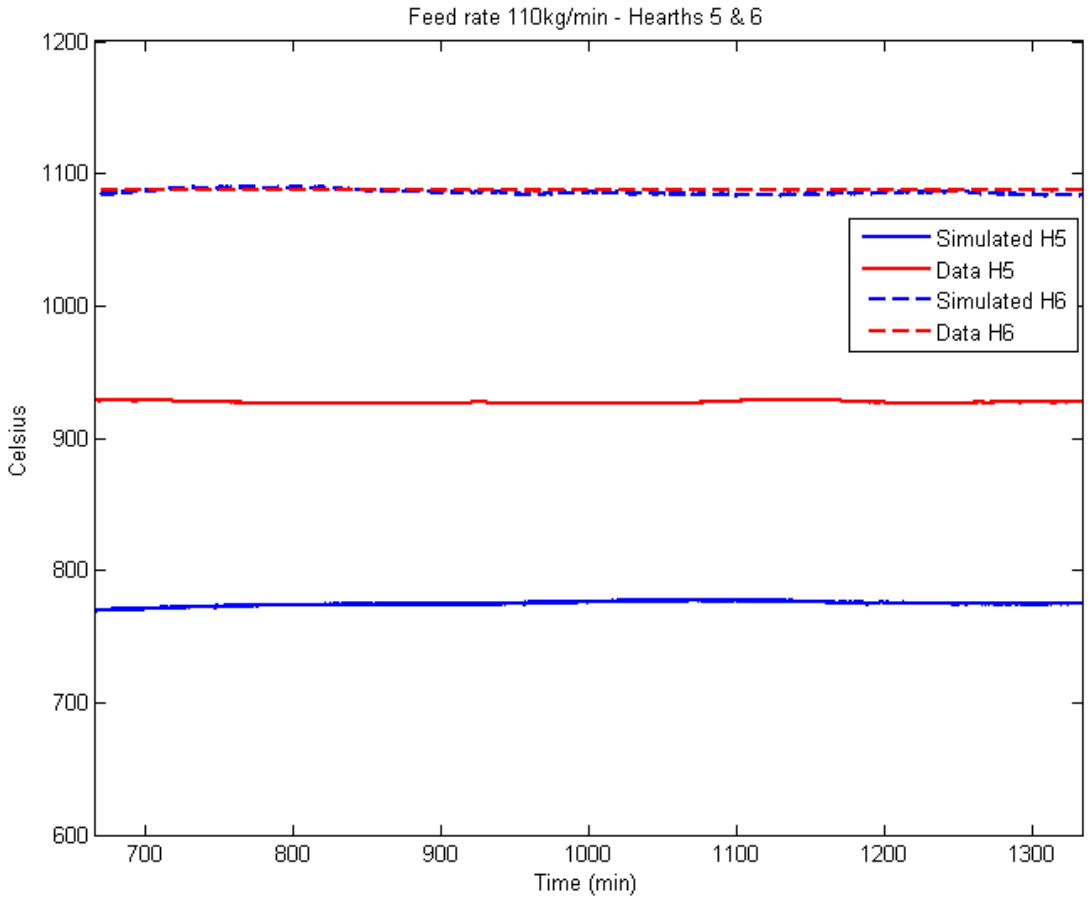

Figure 70. Model behaviour with feed rate of 110 kg/min.

The second test case is performed to study if the model response matches the recorded data during the increase in the feed rate. Figure 71 shows the simulated model response compared to the measurements. As it can be seen from the figure below, the model responses well to the step change and the estimated temperatures behave similarly as the measured temperatures. Especially, the similar response behaviour can be seen very clearly between the simulated curve and the recorded data on the hearth 7.

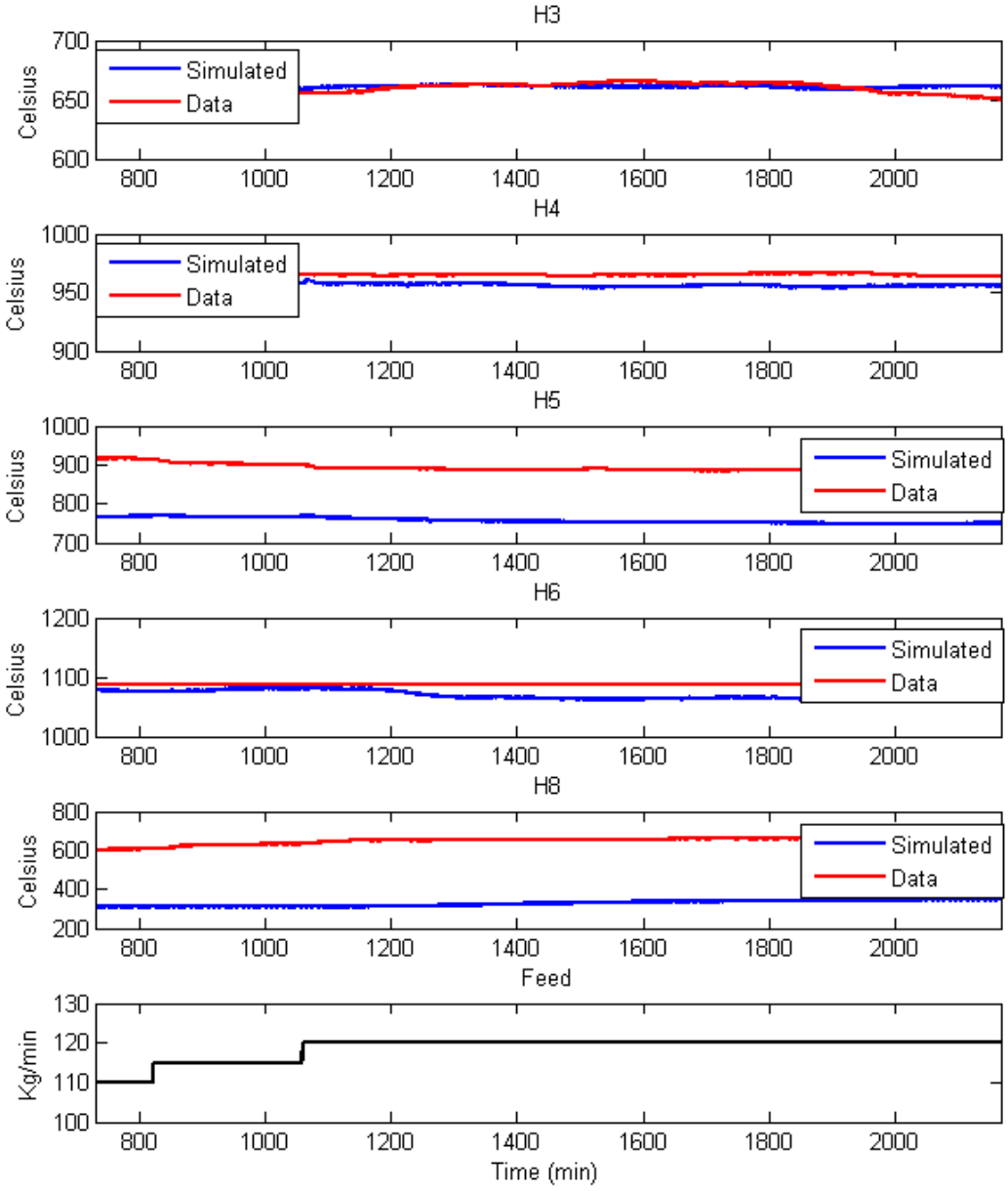

Figure 71. Comparison of model output and measured data during increase in the feed rate.

Figure 72 shows the model behaviour for the third and last test case; operation under a step-like decrease in the feed rate. The results show that the estimated temperatures on hearths the 4, 5 and 6 follow the corresponding recorded temperatures, which is especially seen at the hearth 5 where the behaviour of the curves is very much similar despite the steady difference of 120 °C between the simulated and recorded data.

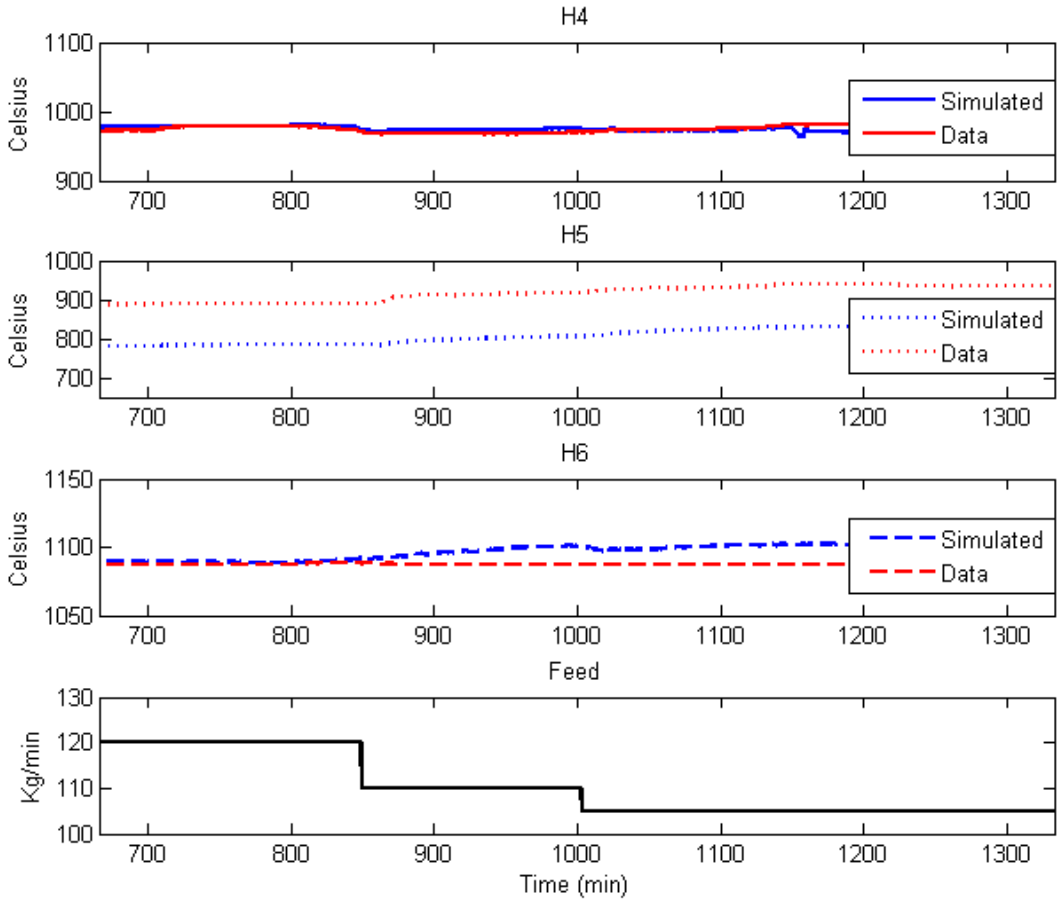

Figure 72. Graph showing the simulated and measured temperatures at hearths 4, 5 and 6 during a decrease step in the feed rate.

Furthermore, the test case three was studied more closely by analysing the composition of the solid bed. Figures 73, 74 and 75 describe the phenomena occurring in the solid bed on the hearth 6. Figure 73 shows how the metakaolin content of each solid volume on the hearth 6 changes during the step change in the feed rate. The volume 1 is the volume where the solids enter the hearth 6 and the volume 4 is the exit volume of the hearth 6. Studying Figure 73 more closely, it is noticeable that the first step change in the feed rate from 120 kg/min to 110 kg/min does have impact to the metakaolin content of the volumes. In the volumes 1 and 4 the metakaolin content is not affected by the first step change suggesting that the product formation occurs in the same volumes with the same intensity as before.

However, in the volumes 2 and 3, the step change in the feed rate clearly has some effect. In both two volumes, the metakaolin content begins to decrease after a steady period experienced under the feed rate of 120 kg/min. In the volume 2 the metakaolin content decreases steadily from the value of 91 mass-percent to the value of 84 mass-percent and in the volume 3 the metakaolin content drops steadily from 61 to 47 percent after the first step change. Next, after the second step change in the feed rate from 110 kg/min to 105 kg/min, the changes in the composition of the volumes become much more evident. The metakaolin content drops in the volume 1 from 97 to 92 percent, in the volume 2 from 84 to 60 percent and in the volume 3 from 47 close to zero percent. This behaviour shows that the product formation reaction occurs earlier, which is confirmed in Figure 74 that presents the product contents of the four volumes on the hearth 6.

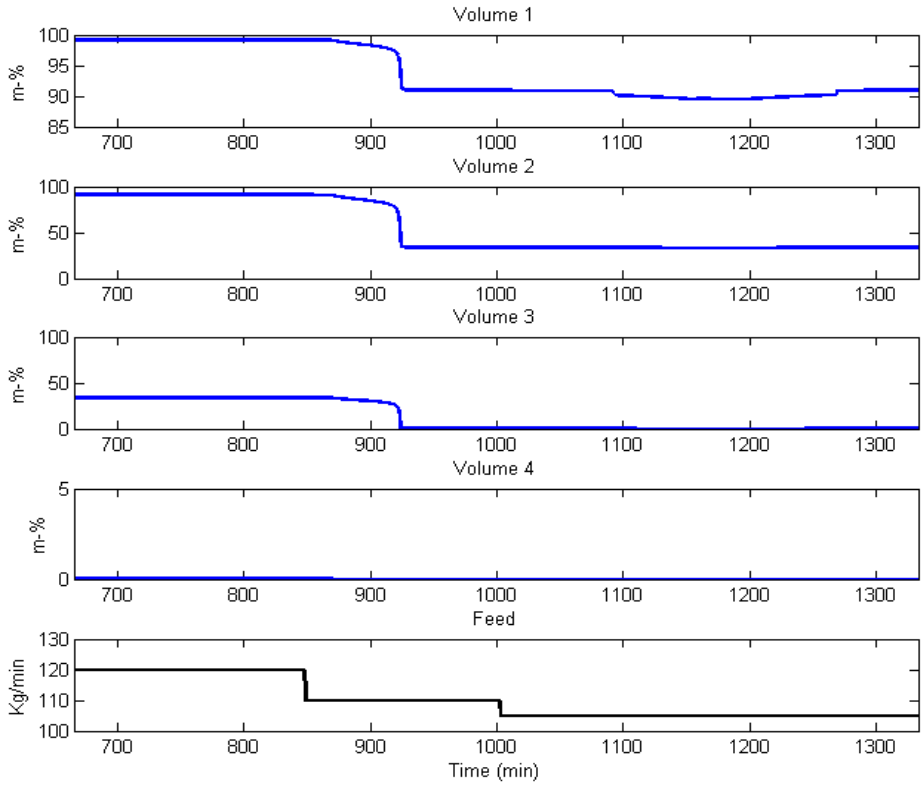

Figure 73. The metakaolin content of the solid bed on hearth 6 during decrease of feed rate.

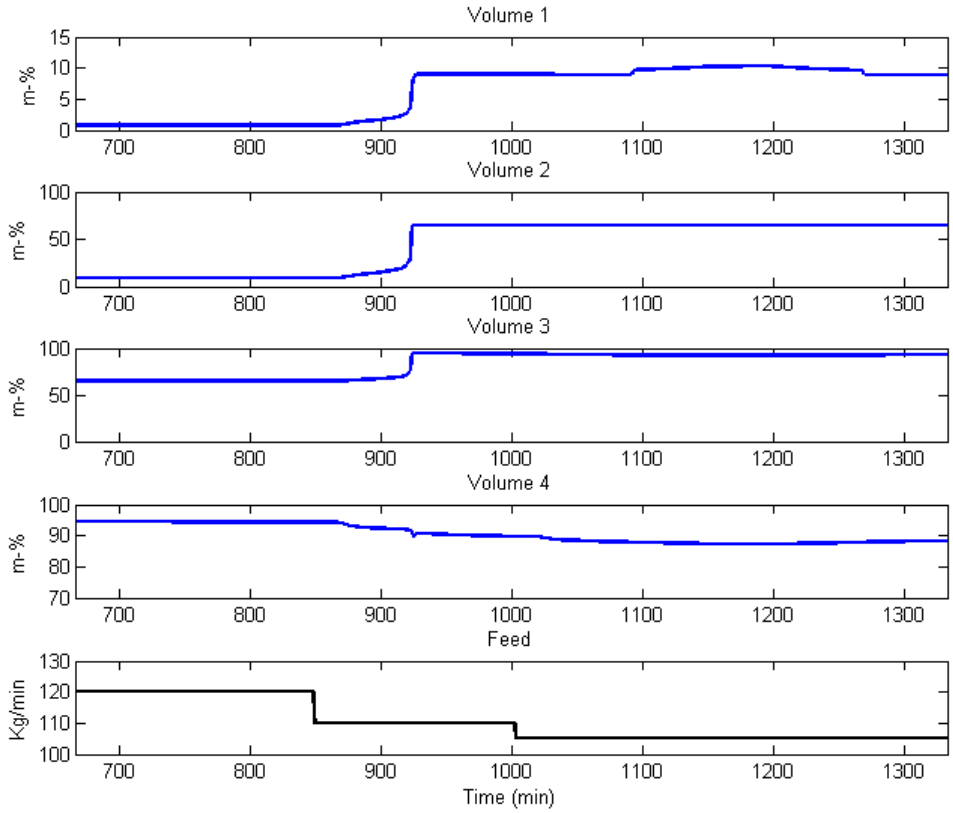

Figure 74. The product content of the solid bed on hearth 6 during decrease in the feed rate.

From Figure 74 it can be seen that the both feed rate changes have the same effect on the product content that was noticed for the metakaolin content on the hearth 6 in Figure 73. Following this further, the most important change occurs after the second feed rate decrease in the volumes 3 and 4, where first in the volume 3 the product content raises up to 93 percent from 52 percent and in the volume 4 the product content decreases from 93 percent to 84 percent. This decrease in the product content is explained by the fact that the product formation reaction has occurred earlier and the temperature of the solids has raised high enough to enable the offspec formation reaction and therefore some product is converted into offspec due to excessive heat supplied to the hearth 6. The detected phenomenon is also confirmed by Figure 75 showing the offspec content of the volumes in the hearth 6.

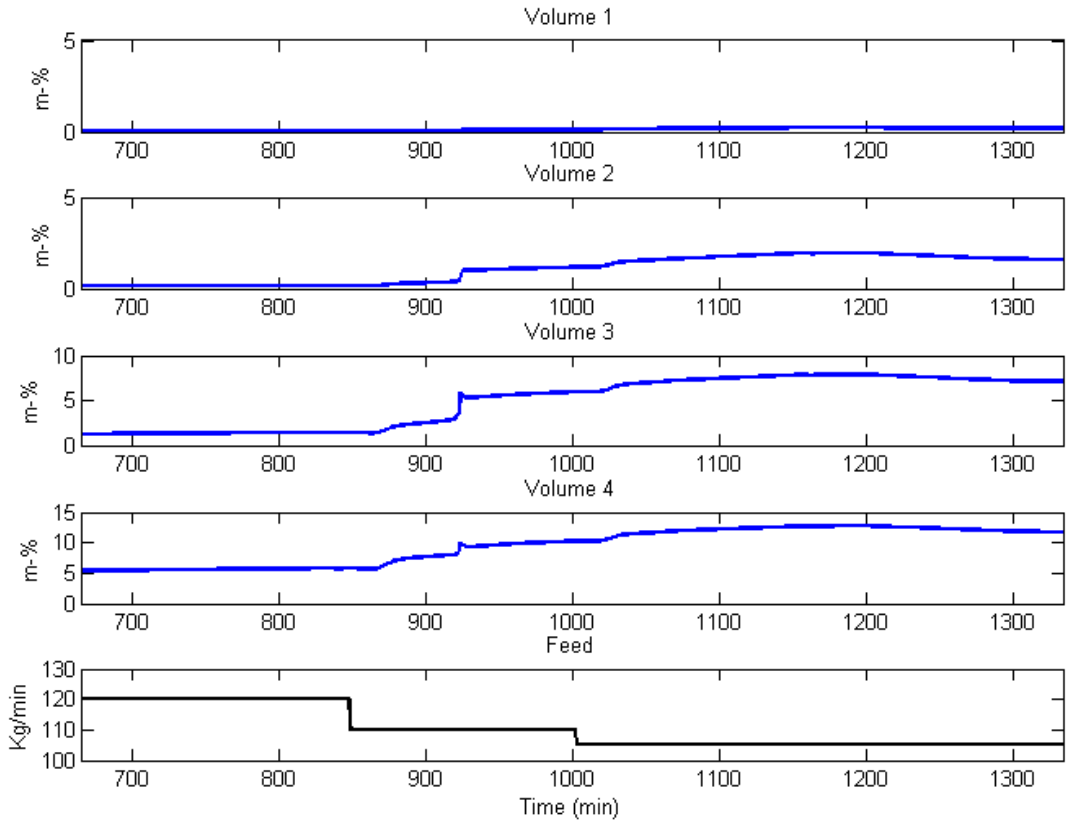

Figure 75. The mullite (offspec) content of the solid bed on hearth 6 during decrease in the feed rate.

Figure 75 shows how the decrease in the feed rate increases mullite (offspec) content in the hearth 6. In the first volume there is not any relevant change in the mullite content and it stays close to zero. In the second volume after the first step change the mullite content increases from zero to 1.5 mass percent and after the second step the mullite content increase to 2 mass percent. Furthermore, in the volumes 3 and 4 the first step change in the feed rate starts to first slowly increase the mullite content and then after about 40 minutes the mullite content surges rapidly reaching a steady state. Subsequently, when the second decrease in the feed rate occurs, the mullite content rises even more, but slowly. After reaching a new steady state the mullite content in the volume 3 has raised from 2 to 7 percent and in the volume 4 the mullite content has raised from five percent up to as high as 12 percent.

The presented three case studies have shown that the estimated temperature profile matches the measured data point relatively well and the modelled temperature estimates have similar behaviour when studying a dynamic response to the step changes in the feed rate. In addition, the third case study showed that the MHF model can be used to study the physico-chemical phenomena occurring inside the furnace as it was shown that a decrease in the feed rate increased the offspec content of the solid bed.

12. Conclusions

The aim of this thesis was to develop a concept of a dynamic model of a MHF to study the physico-chemical phenomena occurring inside the furnace and to provide a dynamic simulator for monitoring purposes. First in the literature part, common kaolin wet processing production chain was introduced after which the kaolin calcination process was studied. Next, calcination reactions and the effects of factors, such as heating rate, particle size and impurities in the raw material to the calcination reactions were studied. Additionally, five different mathematical models similar to the kaolin calcination were reviewed to understand the restrictions and requirements of development of a dynamic model of the MHF.

The dynamic model of the MHF was developed in the experimental part. First, the modelling equations for the reaction kinetics, mass and heat transfer and conservation, including the heat exchange parameters, were described. Next, experimental test were successfully executed with a pilot model of the industrial furnace to determine the solid bed dynamics matrix describing the solid bed movement and mass distribution in the furnace. Following, the algorithms used to solve the system of the model equations are introduced; the reaction rates are solved explicitly, the solid bed mass transfer is calculated using the specifically developed mixing model, the mass and energy balances of the gas phase are solved with the internal division method, the temperature profiles of the cooling air, the central shaft and the arms and the walls are computed using the Euler method combined with internal division and the solid bed energy balance is solved combining the Euler method with the mixing model. The MHF model was implemented under the MATLAB environment which is described in Chapter 10. In addition, the graphical user interface was developed for the MHF simulator.

After describing the pre-processing performed for the industrial data, the results of the tests executed for the dynamic model were presented. The model response was tested for increase and decrease step changes in three different inputs, namely the

feed rate, the gas and air flows to the hearth 4 and the gas and air flows to the hearth 6. In addition, the response for simultaneous changes in each input variables was studied and finally the dynamics of the simulated model was tested and validated using real industrial data. The response of the gas phase temperature was almost immediate and the response time of changes in the solid bed composition was noticed to be even over 700 minutes in some cases. The long response time of the solid bed was caused by the heat reservation capability of the furnace walls, hearth roofs and bottoms and the solid bed. Comparing the simulated results obtained from the dynamic model to that of the industrial data, the model behaves satisfactorily and the simulated temperature profile matches to the measured temperatures.

References

Alopaeus, V., 2008. *Kemian laitetekniikka 1*. Study material. Espoo: TKK.

Anon., 2013. *aqua-calc conversins and calculation*. [Online] Available at: http://www.aqua-calc.com/page/density-table/substance/spices-coma-and-blank-coriander-blank-seed [Accessed 30 December 2013].

ANSI, 1998. *Density, Specific Gravity, and Mass-Moisture Relationships of Grain for Storage*. [Document] American National Standards Institute Available at: http://www.bime.ntu.edu.tw/~dsfon/graindrying/ASAE/501.pdf [Accessed 30 December 2013].

Bellotto, M., Gualtieri, A., Artioli, G. & Clark, S.M., 1995. Kinetic Study of the Kaolinite-Mullite Reaction Sequence. Part I: Kaolinite Dehydroxylation. *Phys Chem Minerals*, 22, pp.207-14.

BNZ Materials, Inc., 2009. *Insulating fire brick*. Product data sheet. BNZ Materials, Inc.

Calderys, 2010. *Technical data sheet - Calde Cast XL 106 C/G*. Technical data sheet. Calderys.

Castelein, O., Soulestin, B., Bonnet, J.P. & Blanchart, P., 2001. The influence of heating rate on the thermal behavior and mullite formation from a kaolin raw material. *Ceramics International*, 27, pp.517-22.

Chandrasehar, S. & Ramaswamy, S., 2002. Influence of mineral impurities on the properties of kaolin and it's thermally treated products. *Applied Clay Science*, 21, pp.133-42.

CRC_Handbook, 2005. *CRC Handbook of Chemistry and Physics*. [Online] Boca Raton: CRC Press (Internet version) Available at: http://www.hbcpnetbase.com [Accessed 18 December 2013].

Criado, J.M., Ortega, A., Real, C. & Torres de Torres, E., 1984. RE-EXAMINATION OF THE KINETICS OF THE THERMAL DEHYDROXYLATION OF KAOLINITE. *Clay Minerals*, 19, pp.653-61.

Design Institute for Physical Properties, Sponsored by AIChE, 2012. *DIPPR Project 801 - Full Version*. [Online] Design Institute for Physical Property Research/AIChE Available at: http://app.knovel.com/hotlink/toc/id:kpDIPPRPF7/dippr-project-801-full [Accessed 23 December 2013].

DSF Refractories, 2009. *DSF 59 - The Product Description Sheets*. Product Description Sheet. DSF Refractories.

Engineering.com, 2006. *Emissivity*. [Online] Available at: http://www.engineering.com/Library/ArticlesPage/tabid/85/ArticleID/151/Emissivity.aspx [Accessed 23 December 2013].

Engineers Edge, LLC, 2013. *Thermal Properties of Metals, Conductivity, Thermal Expansion, Specific Heat*. [Online] Available at: http://www.engineersedge.com/properties_of_metals.htm [Accessed 23 December 2013].

Franks, R.G.E., 1972. *Modeling and simulation in chemical engineering*. 1st ed. New York: Wiley.

Ginsberg, T. & Modigell, M., 2011. Dynamic modelling of a rotary kiln for calcination of titanium dioxide white pigment. *Computer and Chemical engineering*, 35, pp.2437-46.

Ginsberg, T., Modigell, M. & Wilsmann, W., 2011. Thermochemical characterisation of the calcination process step in the sulphate method for production of titanium dioxide. *Chemical engineering research and design*, 89, pp.990-94.

Grim, R.E., 1962. *Applied clay mineralogy*. New York, USA: McGraw-Hill.

Gualtieri, A., Belloto, M., Artioli, G. & Clark, S.M., 1995. Kinetic Study of the Kaolinite-Mullite Reaction Sequence. Part II: Mullite Formation. *Phys Chem Minerals*, 22, pp.215-22.

Hearle, J.A., 2012. *Lee Moor Herreschoff Calciner #3 Operational Manual*. Operational Manual.

Incropera, DeWitt, Bergman & Lavine, 2007. *Fundamentals of Heat and Mass Transfer*. 6th ed. Hoboken: Wiley.

Johnstone, R.E. & Thring, M.W., 1957. *Pilot plants, Models, and Scale-up Methods in Chemical Engineering*. New York: McGraw-Hill Book Company.

Langer, A.M., 1967. Evaluation of kaolinite and quartz differential thermal curves with a new high temperature cell. *The American Mineralogist*, 52, pp.509-23.

Liu, X. & Jiang, J., 2007. Mass and heat transfer in a continuous plate dryer. *Drying technology: An international journal*, 22, pp.1621-36.

Martins, M.A., Oliveira, L.S. & Franca, A.S., 2001. Modeling and simulation of petroleum coke calcination in rotary kilns. *Fuel*, 80, pp.1611-22.

Mazumdar, S. & Mukherjee, B., 1983. Structural Characterization of the Spinel Phase in the Kaolin-Mullite Reaction Series Through Lattice Energy. *Journal of the American Ceramic Society*, 66(9), pp.610-12.

Meisingset, H.C. & Balchen, J.G., 1995. Mathematical modelling of a rotary hearth coke calciner. *Modeling, identification and control* , 16, pp.193-212.

MIKRON Vertretung Schweiz, n.d. *Table of emissivity of various surfaces*. [Online] Available at: http://www-eng.lbl.gov/~dw/projects/DW4229_LHC_detector_analysis/calculations/emissivity2.pdf [Accessed 23 December 2013].

Murray, H.H., 2005. Clays. In *Ullmann's encyclopedia of industrial chemistry*. Weinheim: Wiley-VCH Verlag GmbH & Co. pp.203-35.

Murray, H.H., 2007. *Applied clay mineralogy - Occurrences, Processing and Application of Kaolins, Bentonites, Palyqorskite-Sepiolite, and Common Clays*. 1st ed. Elsevier.

Murray, H.H. & Kogel, J.E., 2005. Engineered clay products for the paper industry. *Appied Clay Science*, 29, pp.199-206.

Pearson, R.K., 2005. *Mining imperfect data: dealing with contamination and incomplete records*. Philadelphia: Society for Industrial and Applied Mathematics.

Perry, R.H. & Green, D.W., 1997. *Perry's chemical engineering handbook*. New York: McGraw-Hill.

Petzold, D., Poppe, B. & Träger, T., 1985. Kalorimetrische Bestimmung der Dehydroxylierungsenthalpie von Kaolinit. *Silicattechnik*, 36, pp.352-54.

Ptacek, P. et al., 2012. The kinetics and mechanism of kaolin powder sintering I. The dilatometric CRH study of sinter-crystallization of mullite and cristobalite. *Powder Technology*, 232, pp.24-30.

Ptacek, P. et al., 2010. Isothermal kinetic analysis of the thermal decomposition of kaolinite: The thermogravimetric study. *Thermochmica Acta*, 501, pp.24-29.

Ptacek, P. et al., 2010. The non-isothermal kinetic analysis of the thermal decomposition of kaolinite by thermogravimetric analysis. *Powder technology*, 204, pp.222-27.

Ptacek, P. et al., 2013. The influence of structure order on the kinetics of dehydroxylation of kaolinite. *Journal of the European Ceramic Society*, 33(13-14), pp.2793-99.

Ptacek, P. et al., 2011. The kinetic analysis of the thermal decomposition of kaolinite by DTG technique. *Powder Technology*, 208, pp.20-25.

Ptacek, P. et al., 2010. The kinetics of Al-Si spinel phase crystallization from calcined kaolin. *Journal of Solid State Chemistry*, 183, pp.2565-69.

Ptacek, P. et al., 2010. The non-isothermal kinetics analysis of the thermal decomposition of kaolinite by Effluent Gas Analysis technique. *Powder Technology*, 203, pp.272-76.

Saito, Y., Hayasho, S., Yasumori, A. & Okada, K., 1996. Effects of calcining conditions of kaolinite on pore structures of mesoporous materials prepared by the selective leaching of calcined kaolinite. *Journal of porous materials*, 3, pp.233-39.

Schieltz, N.C. & Soliman, M.R., 1966. Thermodynamics of the Various High Temperature Transformations of Kaolinite. In *Proceedings of the 13th National Conference on Clays and Clay Minerals*. New York, 1966. Pergamon Press.

Sheyndlin, ed., 1974. *Emissivity properties of solid materials*. Moscow: Energy.

Slade, R.C.T., Davies, T.W. & Atakul, H., 1991. Flash Calcination of Kaolinite: Mechanistic Information from Thermogravimetry. *Journal of Material Chemistry*, 1, pp.751-56.

Thomas, R., 2010. *High temperature processing of kaolinitic materials*. PhD Thesis. University of Birmingham.

Thomas, R. et al., 2009. Residence time investigation of a multiple hearth kiln using mineral tracers. *Chemical Engineering and Processing*, 48, pp.950-54.

Thurlow, C., 2005. *China clay from Cornwall & Devon, An illustrated account of the modern China Clay Industry*. 4th ed. St Austell: Cornish Hillside Publications.

Wang, H., Li, C., Peng, Z. & Zhang, S., 2011. Characterization and thermal behavior of kaolin. *J. Therm. Anal. Calorim.*, 105, pp.157-60.

Voglauer, B. & Jörgl, H.P., 2004. Dynamic model of a roast process for simulation and control. *Mathematical and computer modelling of dynamical systems*, 10, pp.217-30.

Appendices

1. Derivation of the spinel phase peak temperature
2. The gas phase emissivity
3. Photos from the pilot experiments
4. Results of the pilot experiments
5. The model equations and the model parameters and their values

1 Derivation of the spinel phase peak temperature

Equation 6, the peak temperature of the spinel phase where the reaction is at its highest intensity as a function of the heating rate, can be derived from the listed values (Ptacek et al., 2010) given in Table 25. Figure 54 shows the curve of the peak temperature and the corresponding trend curve and its equation.

Table 25. Values for heating rate Φ and peak temperature for the spinel formation reaction according to Ptacek et al. (2010).

Φ (K/min)	T_{peak} / K	T_{peak} / °C
1	1220.57	947.42
2	1230.57	957.42
3	1236.17	963.02
4	1239.47	966.32
5	1243.37	970.22
6	1245.37	972.22
7	1248.17	975.02
8	1250.27	977.12
9	1252.17	979.02
10	1253.67	980.52
15	1259.57	986.42
20	1264.07	990.92
25	1267.67	994.52
30	1270.37	997.22
35	1272.87	999.72
40	1274.77	1001.62

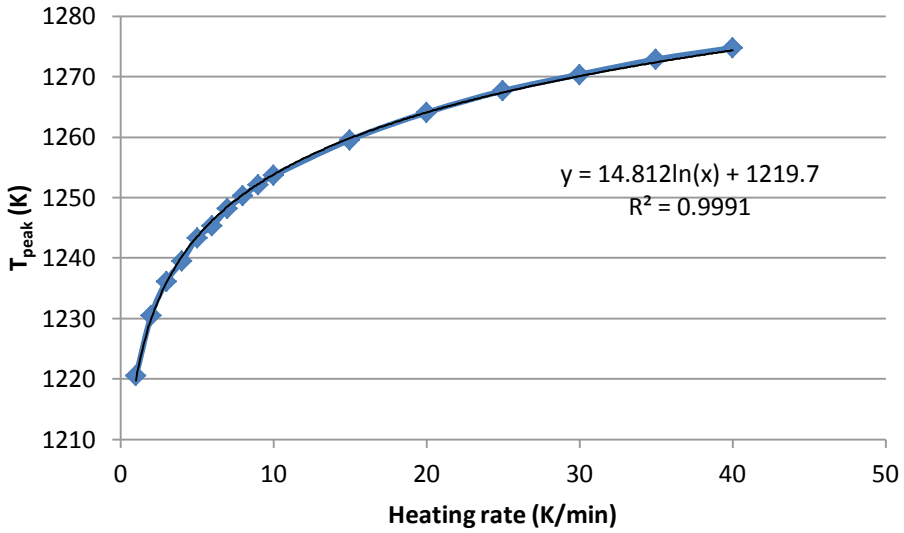

Figure 76. Graph showing the peak temperature of the spinel formation reaction as a function of heating rate.

2 The gas phase emissivity

The gas phase emissivity is calculated according to Perry and Green (1997):

First, the ratios between water and carbon dioxide contents in the gas phase are calculate and then the right columns to be used are determined from Figure 55.

Table 26. Gas phase water and carbon content on hearths 1-6 and the calculated ratios. pw is the water proportion in the gas phase and pc is the carbon dioxide content of the gas phase.

V%, CO2	V%,H2O	pw/pc	pw/(pw+pc)
6.3	28.6	4.523408	0.818952356
6.6	24.9	3.743176	0.78917079
7.0	20.4	2.903267	0.743804371
7.3	14.5	2	0.666666667
6.3	12.6	2	0.666666667
6.0	12.0	2	0.666666667

The following columns were chosen from Figure 55 according to previous calculations:

2	3
⅔(0.6–0.7) corresponding to CH_4, covering natural gas and refinery gas	¾(0.7–0.8) corresponding to $(CH_6)_x$, covering future high H_2 fuels

T, K	*b*	*n*	*b*	*n*
1000	444	0.34	455	0.35
1500	540	0.42	548	0.42
2000	572	0.51	594	0.52

Secondly, the corresponding values for n and b were interpolated according to the hearth temperatures (given in Table 27).

Next, the values for the gas emissivities were calculated using equation

$$\varepsilon_C T = b(pL - 0.015)^n$$

where L is the height of the hearth and p is the pressure (1 atm). The calculated gas phase emissivities are given in Table 27.

Table 27. Temperatures of the gas phase, interpolated values for the parameters b and n and the calculated emissivities of the gas phases in the hearths 1-6.

Hearth	Temp C	b	n	ε
1	620	435.098	0.33502	0.34
2	700	449.978	0.34622	0.32
3	800	468.578	0.36022	0.30
4	900	477.216	0.36768	0.27
5	1000	496.416	0.38368	0.27
6	1100	515.616	0.39968	0.23

TABLE 5-8 Emissivity ε_G of H_2O:CO_2 Mixtures

Limited range for furnaces, valid over 25-fold range of $p_{w+c}L$, 0.046–1.15 m atm (0.15–3.75 ft. atm)

p_w/p_c	0	½	1	2	3	∞
$\frac{p_w}{p_w+p_c}$	0	⅓(0.3–0.42)	½(0.42–0.5)	⅔(0.6–0.7)	¾(0.7–0.8)	1
	CO_2 only	corresponding to $(CH)_x$, covering coal, heavy oils, pitch	corresponding to $(CH_2)_x$, covering distillate oils, paraffins, olefines	corresponding to CH_4, covering natural gas and refinery gas	corresponding to $(CH_6)_x$, covering future high H_2 fuels	H_2O only

Constants b and n of Eq., $\varepsilon_C T = b(pL - 0.015)^n$, pL = m atm, T = K

T, K	b	n	b	n	b	n	b	n	b	n	b	n
1000	188	0.209	384	0.33	416	0.34	444	0.34	455	0.35	416	0.400
1500	252	0.256	448	0.38	495	0.40	540	0.42	548	0.42	548	0.523
2000	267	0.316	451	0.45	509	0.48	572	0.51	594	0.52	632	0.640

Constants b and n of Eq., $\varepsilon_C T = b(pL - 0.05)^n$, pL = ft. atm, T = °R

T, °R	b	n	b	n	b	n	b	n	b	n	b	n
1800	264	0.209	467	0.33	501	0.34	534	0.34	541	0.35	466	0.400
2700	335	0.256	514	0.38	555	0.40	591	0.42	600	0.42	530	0.523
3600	330	0.316	476	0.45	519	0.48	563	0.51	577	0.52	532	0.640

Full range, valid over 2000-fold range of $p_{w+c}L$, 0.005–10.0 m atm (0.016–32.0 ft. atm)
Constants of Eq., $\log_{10} \varepsilon_C T_G = a_0 + a_1 \log pL + a_2 \log^2 pL + a_3 \log^3 pL$

		pL = m atm, T = K					pL = ft. atm, T = °R				
$\frac{p_w}{p_c}$	$\frac{p_w}{p_w+p_c}$	T, K	a_0	a_1	a_2	a_3	T, °R	a_0	a_1	a_2	a_3
		1000	2.2661	0.1742	–0.0390	0.0040	1800	2.4206	0.2176	–0.0452	0.0040
0	0	1500	2.3954	0.2203	–0.0433	0.00562	2700	2.5248	0.2695	–0.0521	0.00562
		2000	2.4104	0.2602	–0.0651	–0.00155	3600	2.5143	0.3621	–0.0627	–0.00155
		1000	2.5754	0.2792	–0.0648	0.0017	1800	2.6691	0.3474	–0.0674	0.0017
½	⅓	1500	2.6451	0.3418	–0.0685	–0.0043	2700	2.7074	0.4091	–0.0618	–0.0043
		2000	2.6504	0.4279	–0.0674	–0.0120	3600	2.6686	0.4879	–0.0489	–0.0120
		1000	2.6090	0.2799	–0.0745	–0.0006	1800	2.7001	0.3563	–0.0736	–0.0006
1	½	1500	2.6862	0.3450	–0.0816	–0.0039	2700	2.7423	0.4561	–0.0756	–0.0039
		2000	2.7029	0.4440	–0.0859	–0.0135	3600	2.7081	0.5210	–0.0650	–0.0135
		1000	2.6367	0.2723	–0.0804	0.0030	1800	2.7296	0.3577	–0.0850	0.0030
2	⅔	1500	2.7178	0.3386	–0.0990	–0.0030	2700	2.7724	0.4384	–0.0944	–0.0030
		2000	2.7482	0.4464	–0.1086	–0.0139	3600	2.7461	0.5474	–0.0871	–0.0139
		1000	2.6432	0.2715	–0.0816	0.0052	1800	2.7359	0.3599	–0.0896	0.0052
3	¾	1500	2.7257	0.3355	–0.0981	0.0045	2700	2.7811	0.4403	–0.1051	0.0045
		2000	2.7592	0.4372	–0.1122	–0.0065	3600	2.7599	0.5478	–0.1021	–0.0065
		1000	2.5995	0.3015	–0.0961	0.0119	1800	2.6720	0.4102	–0.1145	0.0119
∞	1	1500	2.7083	0.3969	–0.1309	0.00123	2700	2.7238	0.5330	–0.1328	0.00123
		2000	2.7709	0.5099	–0.1646	–0.0165	3600	2.7215	0.6666	–0.1391	–0.0165

Figure 77. Table to calculate the emissivity of a water-carbon dioxide gas mixture. (Perry & Green, 1997)

3 Photos from the pilot experiments

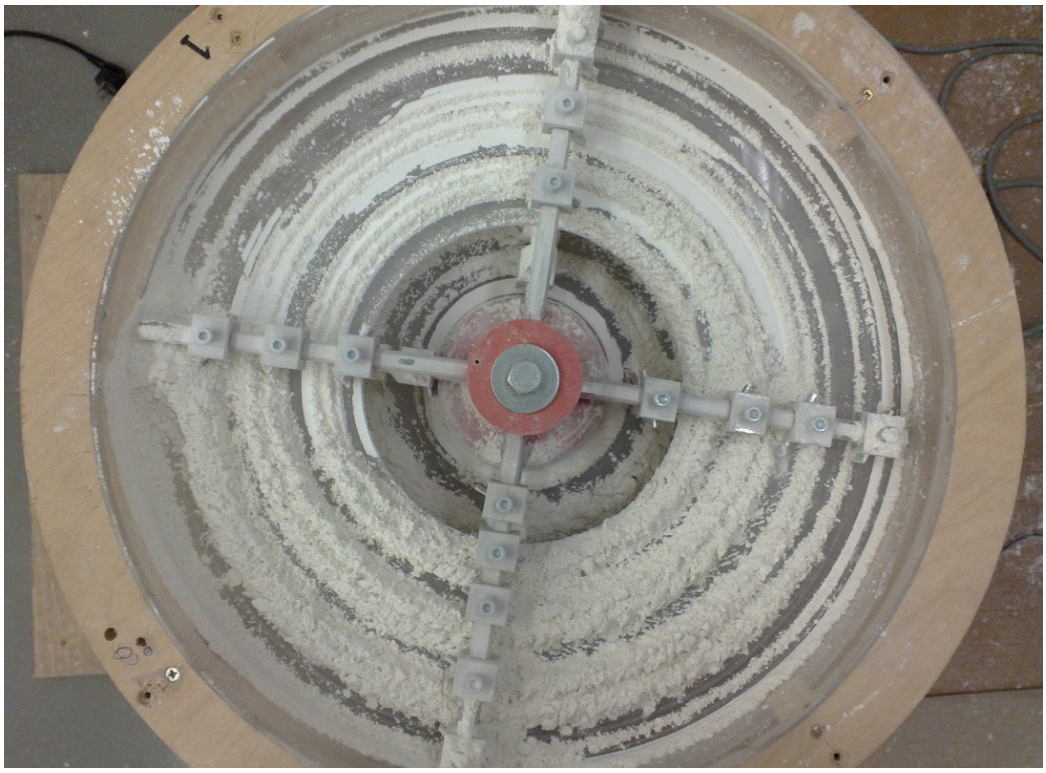

Figure 78. Hearth 1.

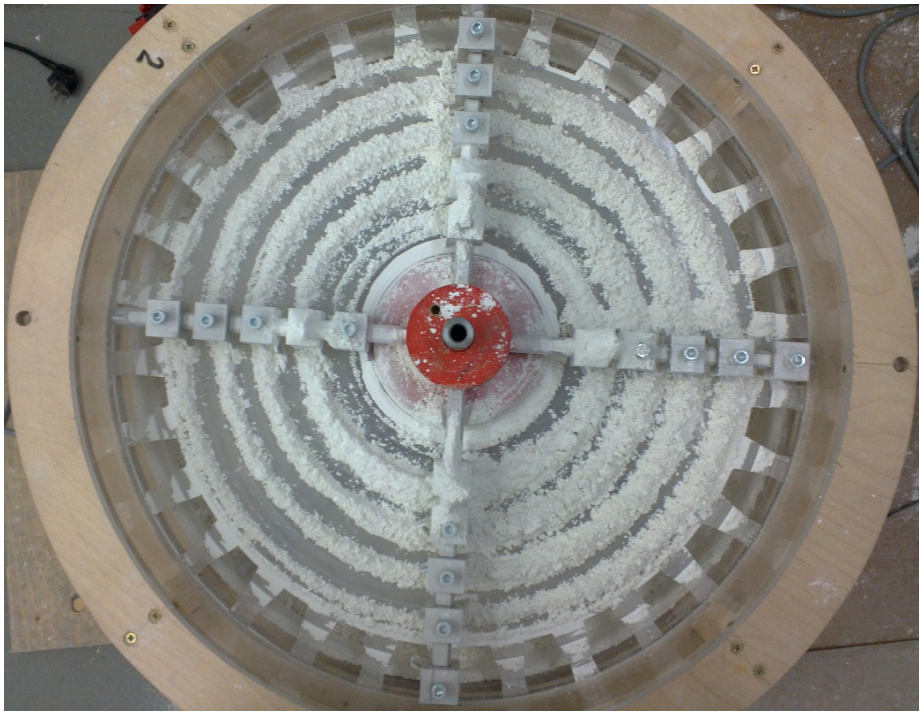

Figure 79. Hearth 2.

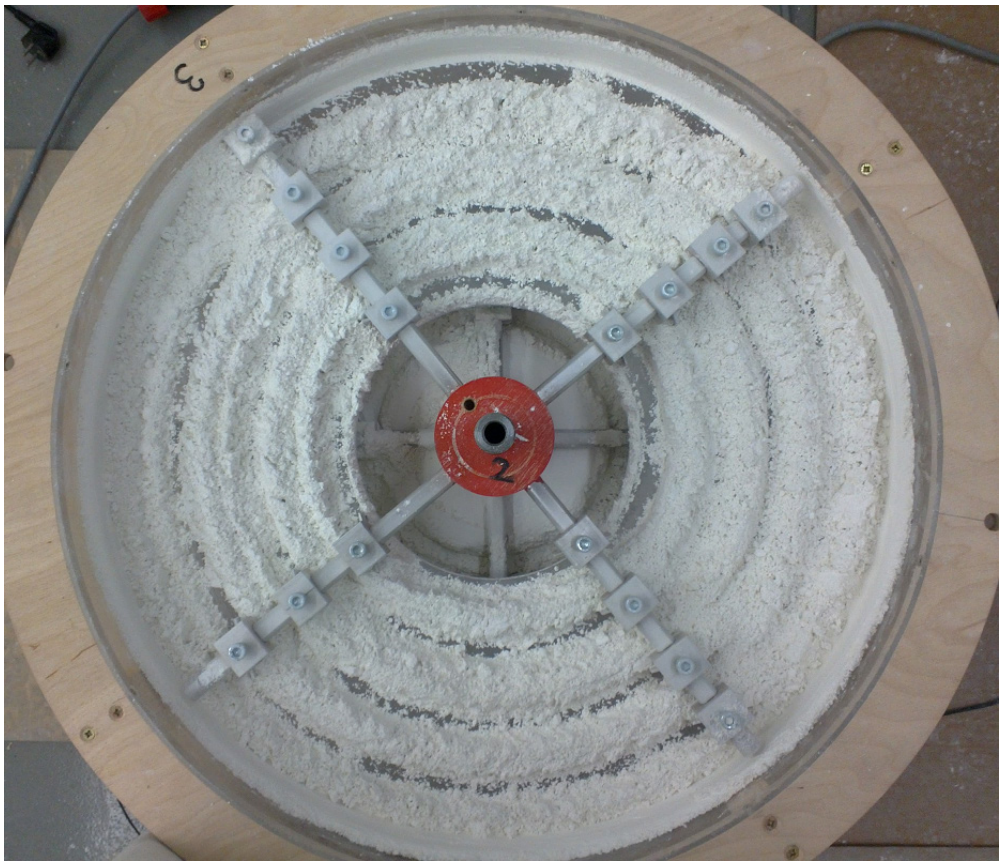

Figure 80. Hearth 3.

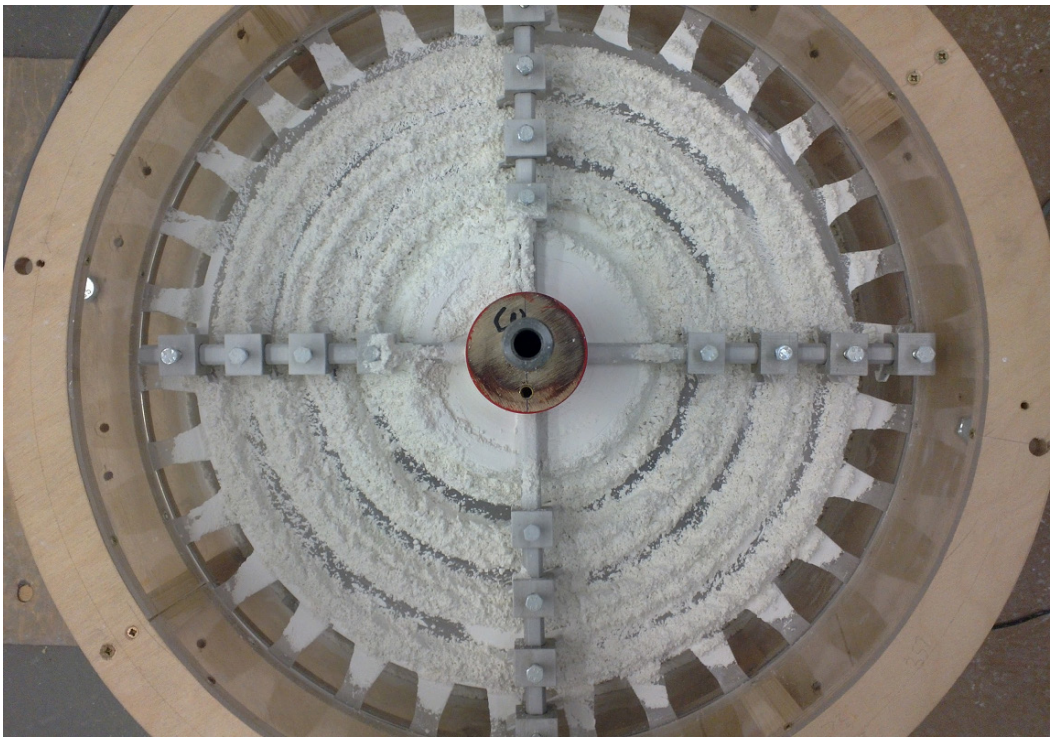

Figure 81. Hearth 4.

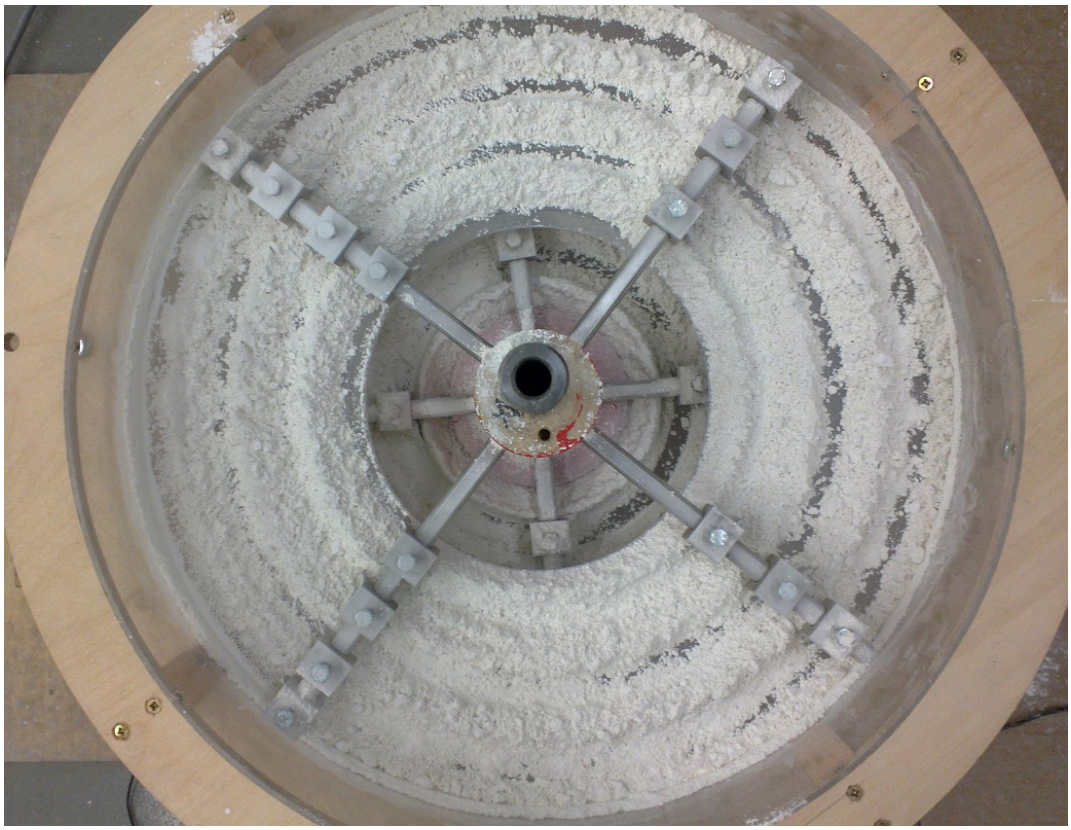

Figure 82. Hearth 5.

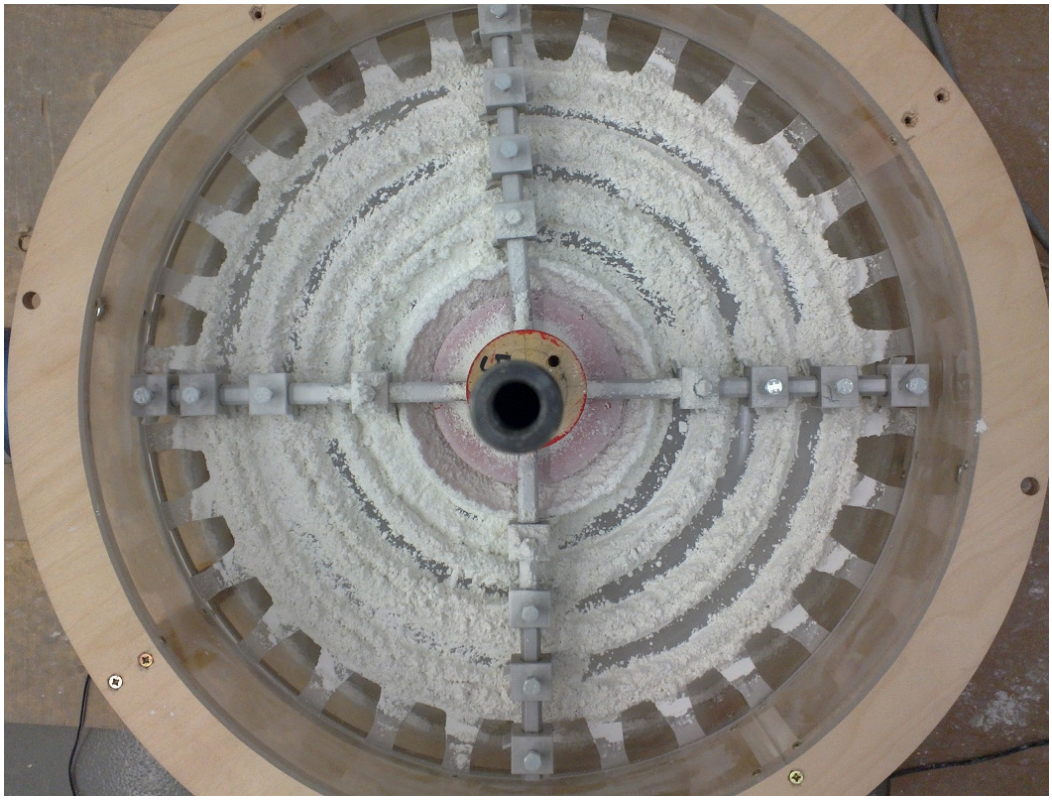

Figure 83. Hearth 6.

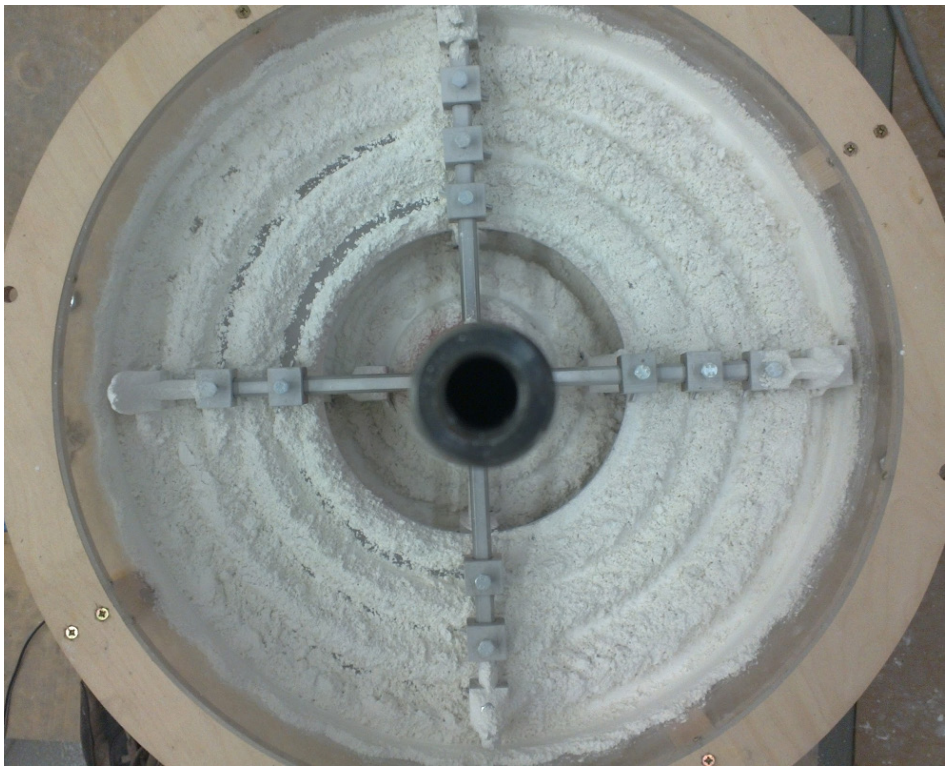

Figure 84. Hearth 7.

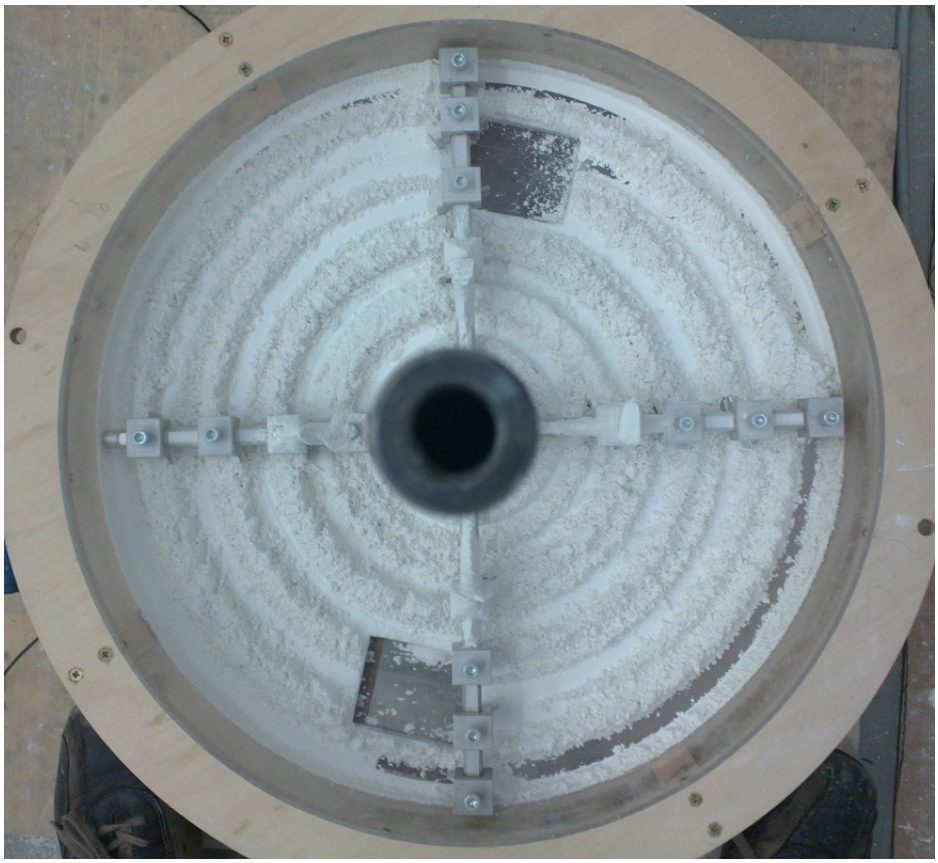

Figure 85. Hearth 8.

4 Pilot experiment results

Table 28. Test results from the residence time distribution test with sesame seeds.

A side				B side	
Sample number	**t(min)**	**Total mass (g)**	**m seeds (g)**	**t(min)**	**Total mass (g)**
1	5	177.4	0	7.5	245.7
2	10	160	0	14	-
3	15	175.9	0.7	19	166.4
4	20	170.6	16.4	25.5	243.8
5	21	42.7	6.3	31.5	214.5
6	22	37.9	5.2	38.5	245.2
7	23	39.2	4.6	47.5	311.62
8	24	37.6	3.5		
9	25	30.3	2.4		
10	26	39.9	2.7		
11	27	35.7	2.2		
12	28	36.4	1.7		
13	29	37	1.4		
14	30	35.8	1		
15	31	39.1	1		
16	32	-	-		
17	33	68.5	1.2		
18	34	32.2	0.3		
19	35	31.3	0.3		
20	36	34.2	0.2		
21	37	31.8	0.1		
22	38	31.2	0.1		
23	39	31.8	0.1		
24	40	35.6	0.1		
25	41	33.8	0		
26	42	31.4	0		
27	43	35.1	0		
28	44	34.1	0		
29	45	34.4	0		
30	46	33.3	0		

Table 29. Test results from the residence time distribution test with coriander seeds.

A side			
Sample number	t(min)	Total mass (g)	m seeds (g)
1	5	166.9	0
2	10	167.6	0
3	15	199.4	0.6
4	16	37.7	0.8
5	17	34	1.4
6	18	35.2	2.6
7	19	36	3.7
8	20	38.2	4.6
9	21	37.1	5
10	22	34.6	4.3
11	23	33.6	4.4
12	24	33.1	4.1
13	25	29.8	3.5
14	26	30	2.7
15	27	26.2	2.2
16	28	26.3	1.7
17	29	27.3	1.4
18	30	26	1.3
19	31	27.8	0.8
20	32	24.8	0.7
21	33	26.5	0.7
22	34	35.7	0.7
23	35	13.7	0.2
24	36	25.1	0.4
25	37	29	0.4
26	38	22.6	0.1
27	39	26.1	0.1
28	40	30	0.1
29	41	112	0.9
30	42	-	-
31	43	78.9	0.4
32	44	77	0.4

B side	
t(min)	Total mass (g)
7.5	249.1
14	246.7
19.5	190.5

Table 30. Test results from the mass distribution tests 1 - 4.

		TEST 1	TEST 2	TEST 3	TEST 4
Hearth	1	209	155.7	157	169.1
	2	113.9	91.5	109.5	118
	3	525.2	402.8	460.2	453.5
	4	270.1	221.3	237.6	237.7
	5	253.2	216.5	179.3	199.2
	6	227.7	199	189.7	198.6
	7	539.2	475.3	455.2	456
	8	324.6	328.6	303.2	318.7
	Sum	2462.9	2090.7	2091.7	2150.8

Table 31. Test results from the mass distribution test 5.

		TEST 5		
		Mass on hearth	Non-moving mass (g)	Moving mass (g)
Hearth	1	162.7	18.9	143.8
	2	114.4	6.5	107.9
	3	437	92.5	344.5
	4	255.6	77.5	178.1
	5	223.8	40.4	183.4
	6	251.8	59.1	192.7
	7	517	120.6	396.4
	8	358.2	31.2	327
	Sum	2320.5	446.7	1873.8

Table 32. Test results from the mass distribution test 6.

		TEST 6		
		Mass on hearth	Non-moving mass (g)	Moving mass (g)
Hearth	1	150.1	132.9	17.2
	2	89.1	83.2	5.9
	3	281.6	231.5	50.1
	4	208.6	139.4	69.2
	5	147.6	135	12.6
	6	213.5	166.9	46.6
	7	343.3	270.7	72.6
	8	230.9	175.4	55.5
	Sum	1664.7	1335	329.7

5 The model equations and the model parameters and their values

This Appendix lists all the equations, parameters and their initial values utilized in the model solving algorithm. The first section covers the computation of the reaction rates, the second section introduces the solid mass balance calculation, and the third section shows the mass and energy balance solving for the gas phase. The fourth section provides the equations, parameters and their initial values for the solving step of the walls, cooling air, rabble arms and the central shaft temperature profiles and finally the last section covers the solid bed energy balance calculation.

Step 1. Computation of the reaction rates

Computation of the reaction rates utilizes two equations, Equations 40 and 41, which require three parameters; frequency factor A, activation energy E_A and reaction enthalpies for each reaction are listed in Table 33 and the initial temperatures of the solid bed volumes are given in Table 34.

Arrhenius reaction rate coefficient

$$k = Ae^{-\frac{E_A}{RT}} \quad (40)$$

Reaction rate

$$R_i = k_i C_i \quad (41)$$

Table 33. Parameters and initial values for Equation 40.

Reaction	**Frequency factor (1/s)**	**Activation energy (J/mol)**	**Reaction enthalpy (kJ/kg)**
Evaporation	$5 * 10^7 \frac{1}{\mathrm{s}}$	$61000 \frac{\mathrm{J}}{\mathrm{mol}}$	2258.22
Dehydroxylation	$1 * 10^7 \frac{1}{\mathrm{s}}$	$145000 \frac{\mathrm{J}}{\mathrm{mol}}$	891.00
Spinel (product) formation	$5 * 10^{33} \frac{1}{\mathrm{s}}$	$856000 \frac{\mathrm{J}}{\mathrm{mol}}$	-212.89
Mullite formation	$1 * 10^{17} \frac{1}{\mathrm{s}}$	$522000 \frac{\mathrm{J}}{\mathrm{mol}}$	1301.70

Table 34. Initial values of the temperatures of the solid bed volumes.

		Volume				
		1	**2**	**3**	**4**	**5**
Hearth	**1**	77.3	71.4	60	45.8	287.8
	2	83.7	96.1	113.2	134.5	158.1
	3	493.8	475.2	416.9	308.5	-
	4	515.2	547.4	570.1	592.4	-
	5	729.9	671.1	622.3	606.7	-
	6	804.9	870	950	1053.3	-
	7	956.3	973.2	1001.1	1069.6	-
	8	905.2	851.5	798.3	753.5	-

Step 2. Solid bed mass balance

The solid bed mass balance solving procedure utilizes Equation 55 and the parameters listed in Table 35.

General mass continuity equation of the solids

$$\frac{\partial m}{\partial t} = m_{in} - m_{out} - R_r \qquad (55)$$

Table 35. Parameters and their initial values for the second step.

Parameter	**Initial value**
Feed rate	Given as data series
Feed inflow composition	99.5 % of kaolin, 0.5 % of water
Reaction rates	Computed in Step 1
Loss of Ignition	14 %
Solid bed dynamics matrix D for each hearth	Given in Tables 36-43
Initial values for the solid bed compositions	Given in Tables 44-48

Table 36. Solid bed dynamics matrix D1.

0.4645	0.5355	0	0	0
0.0255	0.439	0.5355	0	0
0	0.0255	0.439	0.5355	0
0	0	0.0255	0.439	0.0255
0	0	0	0.0255	0.9745

Table 37. Solid bed dynamics matrix D2.

0.16	0.04	0	0	0
0.84	0.12	0.04	0	0
0	0.84	0.12	0.04	0
0	0	0.84	0.12	0.04
0	0	0	0.84	0.16

Table 38. Solid bed dynamics matrix D3.

0.82	0.18	0	0
0.03	0.79	0.18	0
0	0.03	0.79	0.18
0	0	0.03	0.82

Table 39. Solid bed dynamics matrix D4.

0.681	0.029	0	0
0.319	0.652	0.029	0
0	0.319	0.652	0.029
0	0	0.319	0.681

Table 40. Solid bed dynamics matrix D5.

0.637	0.363	0	0
0.033	0.604	0.363	0
0	0.033	0.604	0.363
0	0	0.033	0.637

Table 41. Solid bed dynamics matrix D6.

0.626	0.034	0	0
0.374	0.592	0.034	0
0	0.374	0.592	0.034
0	0	0.374	0.626

Table 42. Solid bed dynamics matrix D7.

0.832	0.168	0	0
0.028	0.804	0.168	0
0	0.028	0.804	0.168
0	0	0.028	0.832

Table 43. Solid bed dynamics matrix D8.

0.736	0.044	0	0
0.264	0.692	0.044	0
0	0.264	0.692	0.044
0	0	0.264	0.736

Table 44. The solid bed water content in kgs.

		Volume				
		1	**2**	**3**	**4**	**5**
Hearth	**1**	0.1093	0.2118	0.2325	0.2378	0.0095
	2	0.0399	0.0117	0.0011	0	0
	3	0	0	0	0	-
	4	0	0	0	0	-
	5	0	0	0	0	-
	6	0	0	0	0	-
	7	0	0	0	0	-
	8	0	0	0	0	-

Table 45. The solid bed kaolin content in kgs.

		Volume				
		1	**2**	**3**	**4**	**5**
Hearth	**1**	49.75	49.75	49.75	49.75	49.75
	2	44.2222	44.2222	44.2222	44.2222	44.2222
	3	130.4231	139.6428	145.7647	147.1336	-
	4	56.1988	49.267	38.5677	26.7999	-
	5	0.2099	2.1977	6.5831	14.2575	-
	6	0.0004	0	0	0	-
	7	0	0	0	0	-
	8	0	0	0	0	-

Table 46. The solid bed metakaolin content in kgs.

		Volume				
		1	**2**	**3**	**4**	**5**
Hearth	**1**	0	0	0	0	0
	2	0	0	0	0	0
	3	14.6065	6.6775	1.4128	0.2355	-
	4	10.6828	16.6442	25.8456	35.9659	-
	5	58.8332	57.1237	53.3524	46.7524	-
	6	56.052	55.4619	50.3379	32.8565	-
	7	0	0	0	0	-
	8	0	0	0	0	-

Table 47. The solid bed product content in kgs.

		Volume				
		1	**2**	**3**	**4**	**5**
Hearth	**1**	0	0	0	0	0
	2	0	0	0	0	0
	3	0	0	0	0	-
	4	0	0	0	0	-
	5	0	0	0	0	-
	6	0.0589	0.6478	5.7545	23.1733	-
	7	130.798	130.798	130.902	132.441	-
	8	108.998	108.998	108.998	108.998	-

Table 48. The solid bed mullite (offspec) content in kgs.

		Volume				
		1	**2**	**3**	**4**	**5**
Hearth	**1**	0	0	0	0	0
	2	0	0	0	0	0
	3	0	0	0	0	-
	4	0	0	0	0	-
	5	0	0	0	0	-
	6	0.0002	0.0017	0.019	0.0817	-
	7	6.1137	6.1137	6.0096	4.4701	-
	8	5.0948	5.0948	5.0948	5.0948	-

Step 3. Gas phase mass and energy balance

The gas phase mass and energy balance calculation involves Equations 59-61, 64, 65, 68-77, 82-85, 94-100, 106 and 107. The parameters for these equations are listed in Table 49.

Gas phase mass balance equation

$$n_{i,in} - n_{i,out} - R_i = 0 \quad (59)$$

Equation to calculate the amount of incoming gas

$$n_{i,in} = c_i^{j+1} F \quad (60)$$

Equation to calculate the real volume of gas

$$F_{real} = F_{NTP}\frac{T_{real}}{T_{NTP}} \quad (61)$$

Gas phase energy balance equation

$$\dot{Q}_{gas,in} - \dot{Q}_{gas,out} + Q_{combustion} + Q_{gw} + Q_{gs} + Q_{gshaft} + Q_{garms} = 0 \quad (64)$$

Gas enthalpy equation

$$\dot{Q}_{gas} = \sum_{i=1}^{5} n_i \int_{300K}^{T_{gas}} c_{p,i} \quad (65)$$

Heat flux between the solid bed and the gas phase

$$Q_{gs} = Q_{rgs} + Q_{cgs} \quad (68)$$

Radiation term between the solid bed and the gas phase

$$Q_{rgs} = \sigma A_{gs}\varepsilon_s\varepsilon_g(T_g^4 - T_s^4) \quad (69)$$

Convective heat flux term between the solid bed and the gas phase

$$Q_{cgs} = h_{cgs}A_{gs}(T_g - T_s) \quad (70)$$

Nusselt number

$$Nu = \frac{hL}{k_g} \quad (71)$$

Nusselt number (2)

$$Nu = 0.23 * Re^{\frac{4}{5}} * Pr^{0.35} \quad (72)$$

Reynold number	$Re = \frac{\rho v D_h}{\mu}$	*(73)*
Prandtl number	$Pr = \frac{c_p \mu}{k}$	*(74)*
Nusselt number under natural convection	$Nu = 0.54 Ra^{1/4}$	*(75)*
Rayleigh number	$Ra = \frac{g\beta(T_s - T_g)L^3}{\nu\alpha}$	*(76)*
Characteristic length	$L = \frac{A}{P}$	*(77)*
Heat flux between the inner walls and the gas phase	$Q_{wg} = Q_{rgw} + Q_{cgw}$	*(82)*
Radiative heat exchange term between the inner wall and the gas phase	$Q_{rgw} = \sigma A_{gw} \frac{(\varepsilon_w + 1)}{2} \varepsilon_g (T_g^4 - T_w^4)$	*(83)*
Convective heat exchange term between the inner wall and the gas phase	$Q_{cwg} = h_{cgw} A_{wg} (T_g - T_w)$	*(84)*

Nusselt number for the hearths 7 and 8

$$Nu = 0.68 + \frac{0.67Ra^{\frac{1}{4}}}{\left(1 + \left(\frac{0.492}{Pr}\right)^{\frac{9}{16}}\right)^{\frac{4}{9}}} \quad (85)$$

Heat flux between the gas phase and the central shaft and the arms

$$Q_{gs} = Q_{rgs} + Q_{cgs} \quad (94)$$

Radiative heat exchange term between the gas phase and the central shaft and the arms

$$Q_{rgs} = \sigma A_{gs} \varepsilon_{shaft} \varepsilon_{gas} (T_{gas}^4 - T_{shaft}^4) \quad (95)$$

Convective heat exchange term between the gas phase and the central shaft and the arms

$$Q_{cgsa} = h_{cgs} A_{gs} (T_{gas} - T_{shaft}) \quad (96)$$

Nusselt number (the shaft is in external gas flow and it is considered as a flat plate parallel to the flow and the flow is turbulent)

$$Nu_{gs} = 0.0296 * Re^{\frac{4}{5}} * Pr^{\frac{1}{3}} \quad (97)$$

Heat transfer coefficient between the central shaft and the gas phase

$$h_{cgs} = \frac{k_{gas}}{L} Nu_{gs} \quad (98)$$

Nusselt number for the rabble arms (long cylinders and Ra<10^{12})

$$Nu = 0.60 + \frac{0.387Ra^{\frac{1}{6}}}{\left(1 + \left(\frac{0.559}{Pr}\right)^{\frac{9}{16}}\right)^{\frac{8}{27}}} \quad (99)$$

Rayleigh number for above equation

$$Ra = \frac{g\beta\left(T_{gas} - T_{arms}\right)L^3}{\nu\alpha} \quad (100)$$

Emissivity of the solid bed

$$\varepsilon_{solidbed} = 2.0982 * 10^{-7} * T_{solidbed}^2 - 0.00064169 * T_{solidbed} + 0.87936 \quad (106)$$

Heat capacity of a gas component

$$c_{p,i}\left[\frac{J}{kmol\ K}\right] = A + B\left[\frac{\frac{C}{T}}{\sinh\left(\frac{C}{T}\right)}\right]^2 + D\left[\frac{\frac{E}{T}}{\cosh\left(\frac{E}{T}\right)}\right]^2 \quad (107)$$

Table 49. Parameters and their initial values for the third step (1/2).

Parameter	**Initial value**
Gas flows to the hearths 4 and 6	Given as data series
Air flows to the hearths 4 and 6	Given as data series
Extraneous air flow to the hearth 8	2086.8 kg/h
Gas flow composition	100 % of methane
Air flow composition	80 % of nitrogen, 20 % of oxygen
Combustion ratios a and b	a = 0.499, b = 0.769
Air feed temperature	65 °C
Gas feed temperature	16 °C

Table 50. Parameters and their initial values for the third step (2/2).

Parameter	**Initial value**
Emissivity of the solid bed	Function of temperature
Emissivity of the gas phase	see Appendix 2
Emissivity of the inner wall surface	0.9
Emissivity of the rabble arms	0.9
Emissivity of the central shaft	0.9
Combustion energy of methane	802 kJ/mol
Initial values for the solid bed volume temperatures	Given in Table 34
Heat capacity parameters A, B, C, D and E for each gas component	Given in Table 16
Initial values for the gas phase composition	Given in Tables 51-55
Initial values for the gas phase temperature	Given in Table 56
Initial values for the wall layer temperatures	Given in Table 57
Initial values for the rabble arms temperatures	Given in Table 58
Initial values for the central shaft temperature	Given in Table 58
Heat exchange areas between the solid bed and the gas phase	Given in Table 59
Heat exchange areas between the inner wall and the gas phase	Given in Table 60
Heat exchange coefficients between the solid bed and the gas phase	Given in Table 61
Heat exchange coefficients between the inner wall and the gas phase	Given in Table 62
Heat exchange area between the rabble arms and the gas phase	0.7411 m^2 per hearth
Heat exchange area between the central shaft and the gas phase	Given in Table 62
Heat exchange coefficient between the rabble arms and the gas phase	Given in Table 62
Heat exchange coefficient between the central shaft and the gas phase	Given in Table 62

Table 51. The initial gas phase methane content in moles.

		Volume				
		1	**2**	**3**	**4**	**5**
Hearth	**1**	0	0	0	0	0
	2	0	0	0	0	0
	3	0	0	0	0	-
	4	0	0	1	4	-
	5	0	0	0	0	-
	6	0	0	1	4	-
	7	0	0	0	0	-
	8	0	0	0	0	-

Table 52. The initial gas phase oxygen content in moles.

		Volume				
		1	**2**	**3**	**4**	**5**
Hearth	**1**	13.8035	13.8035	13.8035	13.8035	13.8035
	2	13.8035	13.8035	13.8035	13.8035	13.8035
	3	13.8035	13.8035	13.8035	13.8035	-
	4	13.8035	13.8035	13.8035	13.8035	-
	5	4.9042	4.9042	4.9042	4.9042	-
	6	15.1604	15.1604	15.1604	15.1604	-
	7	0.5131	0.5131	0.5131	0.5131	-
	8	0.5131	0.5131	0.5131	0.5131	-

Table 53. The initial gas phase nitrogen content in moles.

		Volume				
		1	**2**	**3**	**4**	**5**
Hearth	**1**	962.1046	962.1046	962.1046	962.1046	962.1046
	2	962.1046	962.1046	962.1046	962.1046	962.1046
	3	962.1046	962.1046	962.1046	962.1046	-
	4	962.1046	962.1046	962.1046	962.1046	-
	5	361.4898	361.4898	361.4898	361.4898	-
	6	361.4898	361.4898	361.4898	361.4898	-
	7	2.0525	2.0525	2.0525	2.0525	-
	8	2.0525	2.0525	2.0525	2.0525	-

Table 54. The initial gas phase water content in moles.

		Volume				
		1	**2**	**3**	**4**	**5**
Hearth	**1**	414.0361	414.0361	414.0361	414.0361	414.0361
	2	413.5361	413.5361	413.5361	413.5361	413.5361
	3	412.654	412.654	412.654	412.654	-
	4	392.071	392.071	392.071	392.071	-
	5	123.0816	123.0816	123.0816	123.0816	-
	6	84.1155	84.1155	84.1155	84.1155	-
	7	0	0	0	0	-
	8	0	0	0	0	-

Table 55. The initial gas phase carbon dioxide content in moles.

		Volume				
		1	**2**	**3**	**4**	**5**
Hearth	**1**	113.3613	113.3613	113.3613	113.3613	113.3613
	2	113.3613	113.3613	113.3613	113.3613	113.3613
	3	113.3613	113.3613	113.3613	113.3613	-
	4	113.3613	113.3613	113.3613	113.3613	-
	5	42.7341	42.7341	42.7341	42.7341	-
	6	37.606	37.606	37.606	37.606	-
	7	0	0	0	0	-
	8	0	0	0	0	-

Table 56. Initial gas phase temperatures.

		Volume				
		1	**2**	**3**	**4**	**5**
Hearth	**1**	615	610	600	590	580
	2	620	630	640	650	660
	3	800	750	730	700	-
	4	850	900	950	991	-
	5	990	970	950	928	-
	6	1000	1020	1050	1090	-
	7	770	800	850	930	-
	8	750	700	650	615	-

Table 57. Initial temperatures of the surfaces of the wall layers.

		Volume				
		1	**2**	**3**	**4**	**5**
Hearth	**1**	518.5	487.5	340.9	142.2	142
	2	545.3	512.5	357.6	147.5	147.3
	3	562.5	526.4	360.5	138.6	138.4
	4	797.7	739.2	488.6	165.8	165.4
	5	731.7	678.8	450.7	156.3	156
	6	1093.6	1009	659.2	218.9	218.5
	7	956.9	878.7	574.6	208.2	207.8
	8	621.6	572.3	383.5	157.6	157.4

Table 58. Initial temperatures of the rabble arms, the central shaft and the cooling air.

		Rabble arms	Central shaft	Cooling air
Hearth	**1**	219.9887	359.129	155.8965
	2	220.6755	351.7382	148.2979
	3	264.5972	566.4871	140.0577
	4	338.1638	596.7174	125.3319
	5	285.6519	751.3813	101.6242
	6	429.3633	887.84	77.3869
	7	157.9416	235.3228	37.8246
	8	60.5673	157.65	25.1767

Table 59. Values for the heat exchange areas between the solid bed and the gas phase (m^2).

		Volume				
		1	**2**	**3**	**4**	**5**
Hearth	**1**	0.8043	1.0725	1.3406	1.6087	1.8768
	2	0.8043	1.0725	1.3406	1.6087	1.8768
	3	2.0923	2.9292	3.7661	4.6031	-
	4	2.0923	2.9292	3.7661	4.6031	-
	5	2.0923	2.9292	3.7661	4.6031	-
	6	2.0923	2.9292	3.7661	4.6031	-
	7	2.0923	2.9292	3.7661	4.6031	-
	8	2.0923	2.9292	3.7661	4.6031	-

Table 60. Values for the heat exchange areas between the inner wall and the gas phase (m^2).

		Volume				
		1				
Hearth	**1**	3.0159	4.0212	5.0265	6.0319	18.683
	2	3.0159	4.0212	5.0265	6.0319	18.683
	3	3.927	5.4978	7.0686	25.8217	-
	4	3.927	5.4978	7.0686	25.8217	-
	5	3.927	5.4978	7.0686	25.8217	-
	6	3.927	5.4978	7.0686	25.8217	-
	7	3.927	5.4978	7.0686	25.8217	-
	8	3.927	5.4978	7.0686	25.8217	-

Table 61. Values for the heat exchange coefficients between the solid bed and the gas phase (kJ/K m^2).

		Volume				
		1	**2**	**3**	**4**	**5**
Hearth	**1**	0.0052	0.0039	0.0032	0.0027	0.0024
	2	0.0050	0.0038	0.0031	0.0026	0.0023
	3	0.0043	0.0031	0.0024	0.0020	-
	4	0.0026	0.0019	0.0015	0.0013	-
	5	0.0030	0.0022	0.0017	0.0015	-
	6	0.0011	0.0008	0.0006	0.0005	-
	7	0.0034	0.0034	0.0034	0.0034	-
	8	0.0043	0.0043	0.0043	0.0043	-

Table 62. Values for the heat exchange coefficients between the inner wall and the gas phase, between the central shaft and the gas phase and between the rabble arms and the gas phase (kJ/K m^2). In addition, the values of the heat exchange area between the central shaft and the gas phase (m^2).

		Wall-Gas coefficient	Shaft-Gas Area	Shaft-Gas coefficient	Rabble arms-Gas coefficient
Hearth	**1**	0.0008	0.3354	0.0037	0.0024
	2	0.0008	0.3354	0.0035	0.0023
	3	0.0007	0.3354	0.0031	0.0020
	4	0.0005	0.4437	0.0022	0.0020
	5	0.0002	0.4437	0.0008	0.0007
	6	0.0002	0.4437	0.0008	0.0007
	7	0.0023	0.4437	0.0023	0.0029
	8	0.0029	0.4437	0.0029	0.0038

Step 4. Walls, cooling air, arms and central shaft temperature profiles

The step to calculate the temperature profiles of the walls, the cooling air, the central shaft and the rabble involves Equations 66, 67 and 78-107. The equations presented already in this Appendix are not written here again. The required parameters and their initial values in this step are listed in Table 63.

Walls energy balance equation

$$\frac{\partial Q_w}{\partial t} = Q_{wg} - Q_{ws} - Q_{wa} \quad (66)$$

Central shaft and rabble arms energy balance equation

$$\frac{\partial Q_w}{\partial t} = Q_{gsa} - Q_{sa,cool} \quad (67)$$

Radiative heat flux between the walls and the solid bed

$$Q_{rws} = \sigma A_{sw} \varepsilon_{sw} \left(T_w^4 - T_s^4\right) \quad (78)$$

Emissivity of the wall and solid bed heat exchange

$$\varepsilon_{sw} = \frac{\varepsilon_s \varepsilon_w \left(1 - \varepsilon_g\right)}{1 - U} \quad (79)$$

Variable U in above equation

$$U = (1 - \varepsilon_w)\left(1 - \varepsilon_g\right)[v\left(1 - \varepsilon_g\right)(1 - \varepsilon_s) + (1 - v)] \quad (80)$$

Ratio of the surfaces of the solid bed and the walls

$$v = \frac{A_{sg}}{A_{gw}} \quad (81)$$

Heat flux inside the wall

$$Q_w = \frac{2\pi L(T_{inner\ wall} - T_{outer\ wall})}{\frac{1}{\lambda_1}\ln\left(\frac{r_2}{r_1}\right) + \frac{1}{\lambda_2}\ln\left(\frac{r_3}{r_2}\right) + \frac{1}{\lambda_3}\ln\left(\frac{r_4}{r_3}\right) + \frac{1}{\lambda_4}\ln\left(\frac{r_5}{r_4}\right)} \quad (87)$$

Heat flux between the ambient air and the outer wall

$$\begin{aligned} Q_{wa} &= Q_{cwa} + Q_{rwa} \\ &= h_{cwa}A_{wa}(T_{ambient} - T_{outer\ wall}) \\ &+ \sigma A_{wa}\varepsilon_{outer\ wall}(T_{ambient}^4 \\ &- T_{outer\ wall}^4) \end{aligned} \quad (88)$$

Inner wall layer energy balance equation

$$\frac{\partial Q_{wall\ inner}}{\partial t} = Q_{wg} - Q_{ws} - Q_w \quad (89)$$

Temperature change of a layer of the wall

$$\begin{aligned} \frac{\partial T_{wall\ section}}{\partial t} &= -Q_w \\ &* \ln\left(\frac{r_{i+i}}{r_i}\right)\frac{1}{2\pi\lambda_i h_{wall}} \end{aligned} \quad (90)$$

Rayleigh number for natural convection on a vertical hot plate

$$Ra = \frac{g\beta(T_{wall\ outer} - T_{ambient})L^3}{\nu\alpha} \quad (91$$

Nusselt number if $Ra_{wa} > 10^9$

$$Nu_{wa} = 0.10 * Ra_{wa}^{\frac{1}{3}} \quad (92)$$

Heat transfer coefficient between the ambient air and the outer wall

$$h_{wa} = \frac{Nu_{wa}k_{air}}{L} \quad (93)$$

Heat flux between the cooling air and the central shaft

$$Q_{shaft\_cool} = Q_{rshaft\_cool} + Q_{cshaft\_cool} \quad (101)$$

Radiative heat exchange term between the cooling air and the central shaft

$$Q_{rshaft\_cool} = \sigma A_{shaft\_cool} \varepsilon_{shaft} \quad (T_{shaft}^4 - T_{cool}^4) \quad (102)$$

Convective heat exchange term between the cooling air and the central shaft

$$Q_{cshaft\_cool} = h_{cshaft\_cool} A_{shaft\_cool} (T_{shaft} - T_{cool}) \quad (103)$$

Nusselt number (turbulent flow inside a pipe)

$$Nu = 0.023 * Re^{0.8} * Pr^{\frac{1}{3}} \left(\frac{\bar{\mu}}{\mu_w}\right)^{0.14} \quad (104)$$

Characteristic length

$$D_h = 4 * \frac{Cross\ sectional\ area\ of\ the\ arm}{Perimeter\ of\ the\ arm} \quad (105)$$

Table 63. Parameters and their initial values for the fourth step (1/2).

Parameter	Initial value
The inner radius of the furnace	3.0385 m
The widths of the wall layers	Given in Table 14
Heat conductivities of the wall layers	Given in Table 14
Area of the heat exchange surface between the gas phase and the walls	Given in Table 60
Heat exchange coefficient between the gas phase and the inner wall surface	Given in Table 62
Emissivity of the inner wall surface	0.9
Emissivity of the gas phase	see Appendix 2
Area of the heat exchange surface between the solid bed and the walls	Given in Table 59
Emissivity between the solid bed and the inner walls	Function of temperature
Height of the outer surface of the walls	1.143 m
Conduction constant over the whole wall	0.2879 J/m^2K
Area of the heat exchange surface between the ambient air and the outer wall	Given in Table 64
Heat exchange coefficient between the ambient air and the outer wall surface	Given in Table 64
Combined heat capacity of the inner wall layer and the hearth roofs	14.979 kJ/K
Cooling air inlet temperature	20 °C
Composition of the cooling air	80 % nitrogen, 20 % oxygen
Area of the heat exchange surface between the cooling air and the central shaft	Given in Table 64
Heat exchange coefficient between the cooling air and the central shaft	0.0101 kJ/m^2 K
Area of the heat exchange surface between the cooling air and the arms	3.7699 m^2 per hearth
Heat exchange coefficient between the cooling air and the arms	0.03 kJ/m^2 K
Area of the heat exchange surface between the gas phase and the central shaft	Given in Table62
Heat exchange coefficient between the gas phase and the central shaft	Given in Table 62

Table 64. Parameters and their initial values for the fourth step (2/2).

Parameter	**Initial value**
Emissivity of the central shaft	0.9
Heat capacity of the central shaft	H1-3: 368.96 kJ/K, H4-8: 488.10 kJ/K
Area of the heat exchange surface between the gas phase and the arms	0.7411 m^2
Emissivity of the arms	0.9
Heat capacity of the arms	379.35 kJ/K
Initial values for the solid volume temperatures	Given in Table 34
Initial values for the rabble arms temperatures	Given in Table 58
Initial values for the central shaft temperature	Given in Table 58
Initial values for the walls temperature profile	Given in Table 57
Initial values for the cooling air temperature	Given in Table 58

Table 65. Values for the heat exchange coefficients between the outer wall and the ambient air (kJ/K m^2) and the values of the heat exchange areas between the ambient air and the outer wall and between the central shaft and the cooling air (m^2).

		Ambient-Wall Area	Ambient-Wall coefficient	Cooling air-Shaft Area
Hearth	**1**	18.41	0.0039	1.66
	2	18.41	0.0039	1.66
	3	18.41	0.0045	1.66
	4	24.35	0.0051	2.19
	5	24.35	0.0050	2.19
	6	24.35	0.0048	2.19
	7	24.35	0.0041	2.19
	8	24.35	0.0036	2.19

Step 5. Solid bed energy balance

The final step calculates the solid bed energy balance and it involves Equations 62, 63, 78-81, 106 and 107. The equations presented already in this Appendix are not written here again. The required parameters and their initial values in this step are listed in Table 66.

Solid bed energy continuity equation

$$\frac{\partial Q}{\partial t} = \dot{Q}_{mass,in} - \dot{Q}_{mass,out} - \dot{Q}_{reactions} - \dot{Q}_{evaporation} + Q_{sw} + Q_{sg} \quad (62)$$

Equation for solid enthalpy calculation

$$\dot{Q}_{kaolin} = c_{p,kaolin} m_{kaolin} T_{kaolin} \quad (63)$$

Table 66. The equations and the parameters required to compute the solid bed energy balance.

Parameter	**Initial value**
Feed rate	Given as data series
Feed inflow composition (Kaolin/water)	99.5 % of kaolin, 0.5 % of water
Temperature of the feed	30 °C
D-matrices for each hearth	Given in Tables 36-43
Reaction enthalpies	Given in Table 33
Reaction rates	Computed in Step 1
Loss on Ignition	14 %
Area of the heat exchange surface between the gas phase and the solid bed	Given in Table 59
Heat exchange coefficient between the gas phase and the solid bed surface	Given in Table 60
Emissivity of the solid bed	Function of temperature
Emissivity of the gas phase	see Appendix 2
Area of the heat exchange surface between the solid bed and the walls	Given in Table 59
Emissivity between the solid bed and the inner walls	Function of temperature
Heat capacities of the solid components	Given in Table 13
Initial values for the solid volume temperatures	Given in Table 34